HOKKAIDO UNIVERSITY

Title	Raman Spectroscopy for Spatial Heterogeneity in Membrane-less Organelles
Author(s)	Tian, Ya
Degree Grantor	北海道大学
Degree Name	博士(情報科学)
Dissertation Number	甲第16698号
Issue Date	2025-12-25
DOI	https://doi.org/10.14943/doctoral.k16698
Doc URL	https://hdl.handle.net/2115/98672
Type	doctoral thesis
File Information	Tian_Ya.pdf, 全文

Hokkaido University Collection of Scholarly and Academic Papers : HUSCAP

Raman Spectroscopy for Spatial Heterogeneity in Membrane-less Organelles

ラマン分光法を用いた非膜オルガネラの空間的不均一性解析

Ya Tian

Graduate School of Information Science and Technology,

Hokkaido University

Supervisor: Hiroshi Uji-i

Table of Contents

Acknowledgments ..... *iii*

Abstract *1*

Chapter 1 General Introduction *5*

1.1 Introduction to membrane-less organelles in Eukaryotes **6**

1.1.1 The molecular language of LLPS and MLOs 9

1.1.2 Relationship between membrane-less organelles and amyotrophic lateral sclerosis 18

1.2 Introduction to Raman spectroscopy **32**

1.2.1 Raman scattering 34

1.2.2 Bio-applications of Raman spectroscopy 39

1.3 Problem statement and research objectives **42**

1.3.1 Problem statement 42

1.3.2 Research objectives 45

1.4 References **47**

Chapter 2 Spatially Heterogeneous Dynamics of droplets formed by arginine-rich dipeptides and poly-A RNA during liquid-liquid phase separation ***67***

2.1 Abstract 68

2.2 Introduction 69

2.3 Materials and methods 71

2.4 Results and discussion 73

2.5 Conclusions 78

2.6 Appendix 79

2.7 References 80

Chapter 3 Raman spectroscopy and FRAP analysis on density heterogeneity and diffusion behavior of complex coacervation by arginine-rich dipeptides and poly-A RNA ***83***

3.1 Abstract 84

3.2 Introduction 85

3.3 Experimental Section 88

3.4 Results and discussion 91

3.5 Conclusions 104

3.6 Appendix 106

3.7 Reference 113

Summary and perspective ***119***

Publications ***121***

Conferences ***123***

Acknowledgments

Times fly.

Hokkaido University provided me with the President's Fellowship and gave me a chance to study in Japan.

I would like to express my gratitude to Professor Hiroshi Uji-i who gave me an offer and a chance to continue the doctoral study. It is the first time I start to think about the nature when I face the results I got. Every step is important when dealing with the science. I learned to explain the data, I should be responsible for all the conclusions I get when we do scientific things. When I wrote the scientific articles, Hiroshi gave me a lot of assistance and advice. Without his help, I would not understand what the scientific thing is, and the method to arrange the ideas to tell a good story. Also, I learned about the never-give-up mind from Hiroshi based on his study story from Kyoto to Tohoku, and his research work in Belgium. Many thanks to him for giving me advice and offering financial support during my PhD study in Japan.

I would like to express my gratitude to Associate Professor Kenji Hirai for the help in reminding me of all the deadlines and the necessary progress of my study here. He is always there to ensure that I stay on track with every aspect of my work. His proactive approach in confirming the progress of each task is incredibly helpful. He regularly checks in with me, providing gentle reminders about upcoming deadlines and milestones. With his support, I feel more accountable and motivated to meet my goals. Many thanks to him for reminding me, and supporting me always.

I would like to express my gratitude to Associate Professor Tomoko Inose for the help in teaching me the cell experiments and for giving me advice on the experiments. She has patiently guided me through experimental procedures, offering clear and thorough instructions

at every step. Her expertise in data analysis is remarkable; she not only taught me various analytical techniques but also helped me interpret the results with great insight. Moreover, she goes above and beyond by meticulously reviewing my data. Her attention to detail has helped me catch errors and improve the quality of my work significantly. Many thanks to her for teaching me the experimental methods here.

I would like to express my gratitude to Associate Professor Qiang Zhang for his help. He taught me endoscopy and now I am good at inserting the silver nanowires inside the nucleoli of the cancer cells. Also, when I have problems with the next step of the experiment, Zhang always helps me and gives me advice. Many thanks to him for his kindness and patience.

I would like to express my gratitude to Professor Kohsuke Kanekura for his help. He helped me with the project about membrane-less organelles and gave me a lot of advice about the results. Many thanks to him for his kindness and help.

I would like to express my gratitude to Assistant Professor Farsai Taemaitree, Dr. Motosuke Tsutsumi, Saito-San, and Ishide-san for their help.

I would like to express my gratitude to all of the professors who have taught me during my study in Hokkaido University.

I would like to express my gratitude to all lab mates in nanomaterials and microscopy for the great discussions about science and life.

I would like to express my gratitude to Kitahama-san, Oita-san, Sakamato-san, Kitadate-san, Kanisawa-san, Takekuma-san and all staff in IST office. They always try their best to help me.

I would like to express my gratitude to the Hokkaido University President's Fellowship for the doctoral scholarship.

I would like to express my gratitude to Hokkaido University for letting me study here.

I would like to express my gratitude to all managers at Hokkaido University International House Kita 23 for helping me with my daily life living in Japan.

I would like to thank my father and mother for their support and company. They always stand behind me and encourage me.

I would like to express my gratitude to all of the people who have ever helped me during my study in Hokkaido University.

Thanks to everyone again.

Abstract

Membrane-less organelles (MLOs) are formed via liquid-liquid phase separation (LLPS) within cells. MLOs play a critical role in various cellular processes and exchange molecules quickly with surroundings. Moreover, the formation and dynamic behaviors of MLOs have significant implications for understanding human health. Disruptions in their formation and alteration in their dynamics have been linked to several diseases. Specifically, MLOs exhibit abnormal diffusion dynamics contributing to impaired functions with neurodegenerative diseases. Understanding the underlying molecular mechanisms of the diffusion dynamics and their contributions to disease development could be the key to unlocking novel therapeutic strategies targeting MLOs in neurodegenerative diseases.

Neurodegenerative diseases are characterized by the loss or dysfunction of neurons in the human brain. Two common examples are Amyotrophic Lateral Sclerosis (ALS) and Frontotemporal Dementia (FTD), both of which have been linked to abnormal repeat expansions of *GGGGCC* sequences within the intron of mutant *C9ORF72* gene. These hexanucleotide repeat expansions are translated via a non-ATG mechanism into toxic arginine-rich dipeptides, which could accumulate within various MLOs via LLPS and alter the diffusion behaviors. The diffusion dynamics and spatial heterogeneity within these LLPS-derived MLOs remain poorly understood.

In Chapter 2, we investigated *in vitro* liquid droplets formed by positively charged arginine-rich dipeptides, $(PR)_{20}$ (twenty repeats of proline–arginine) mixed with negatively charged homopolymeric adenine (poly-A RNA), with spatially resolved fluorescence recovery after photobleaching (FRAP) analysis and Raman spectroscopy. The result was compared with an artificially designed dipeptide, $(P_4R_4)_5$, which has the same number of proline and arginine but

with the uneven charge pattern consisting of five repeats of four continuous proline and four continuous arginine. Although $(PR)_{20}$ and $(P_4R_4)_5$ have the same net charge, FRAP analysis revealed the reduced fluidity in $(P_4R_4)_5$ / poly-A RNA compared to $(PR)_{20}$ / poly-A RNA droplets, which is mainly caused by the uneven partition of the positively charged arginine in $(P_4R_4)_5$ dipeptide leads to the higher binding energy compared to repetitive structure of $(PR)_{20}$. Our findings revealed that Raman spectroscopy effectively enables the monitoring of the spatial gradient of RNA concentration inside individual droplets, which can be correlated with FRAP analysis. These positively charged arginine-rich dipeptides concentrate within liquid droplets and play a crucial role in forming a hierarchical structure within liquid droplets. Taken together, Raman spectroscopy provides insights into understanding the diffusion dynamics and a more comprehensive understanding of their spatial distribution and molecular diffusion.

To further understand the mechanism regulating the diffusion behaviors of charged molecules in MLOs, in Chapter 3, we employed Raman spectroscopy and FRAP analysis to elucidate the spatial distribution and molecular diffusion behaviors of the dipeptides with different charge properties and poly-A RNA within LLPS-derived liquid droplets *in vitro*. Although $(PR)_{20}$ and $(GR)_{20}$ have the same partition of the repeat sequence and net charge, their sequence-specific charge distribution would influence the dynamics of LLPS-derived liquid droplets. Raman spectra of individual LLPS liquid droplet revealed that $(GR)_{20}$ / poly-A RNA complexes have a higher density of RNAs than $(PR)_{20}$ / poly-A RNA droplets. Furthermore, we observed a concentration gradient of RNA within individual liquid droplets in Raman spectra maps, while the intensity ratios between dipeptide and RNA remained uniform, suggesting a hierarchical structure and the formation of stable RNA-dipeptide complexes. FRAP analysis of RNA and various small dye molecules with different net charges further indicated heterogeneous diffusion dynamics, with slower diffusion at the droplet center compared to the inner boundary. This trend aligns with the observed concentration gradient of RNA and dipeptides in the Raman spectroscopic measurements. Notably, only the negatively charged fluorescein showed a

significant difference in the ratio of center-to-boundary recovery time between $(PR)_{20}$ and $(GR)_{20}$ droplets, suggesting stronger interaction with $(GR)_{20}$.

Together, these findings reveal spatial heterogeneity and diffusion behaviors within LLPS-derived liquid droplets and highlight charge-dependent interactions in LLPS droplets. These results provide insights into the mechanisms governing molecular diffusion dynamics, contributing to a deeper understanding of protein aggregation in neurodegenerative diseases.

Chapter 1

General Introduction

1.1 Introduction to membrane-less organelles in Eukaryotes

Eukaryotic cells have evolved organelles to organize their components spatially and temporally to carry out functions by two classes of sub-cellular compartments in both nucleus and cytoplasm: membrane-bound organelles that compartmentalize materials within a lipid bilayer membrane and membrane-less organelles (MLOs) formed via liquid-liquid phase separation (LLPS) within cells that lack delimiting membranes and exchange with the subcellular surroundings quickly. There are many MLOs, including nucleoli, Cajal bodies, and promyelocytic leukemia (PML) bodies in the nucleus, and stress granules (SGs) and P bodies in the cytoplasm, as shown in Figure 1.1.[1] In addition, MLOs can form and disassemble repeatedly when needed at different stages of cell cycles. For example, the nucleolus, one of the MLOs, was described as liquid-like in the 1830s under a light microscope,[2, 3] is present at the non-mitotic stage and disassembles at the mitotic stage. The formation of SGs, which are highly dynamic MLOs formed via LLPS, can be induced by stress stimuli, including viral infection, oxidative stress and heat.[4, 5, 6, 7] They disappear quickly when the stress stimulus is removed.[8] Additionally, certain anticancer drugs can be recruited into the MLOs,[9] and some toxic peptides can impede the function of the MLOs.[10] The dynamic behaviors and functions of MLOs are primarily governed by their physical properties. These liquid-like features are key to understanding how MLOs operate within cells.

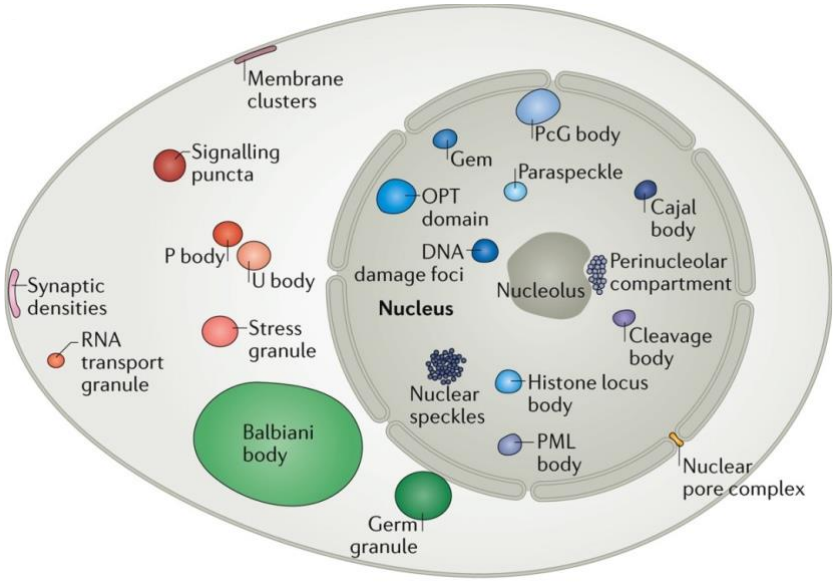

Figure 1.1. MLOs in eukaryotic cells [adapted from[1]]

Recent studies focus on MLOs with a series of emergent physicochemical properties, such as density, surface tension, viscoelasticity, and electrochemical potential.[11] These properties likely influence biochemistry and cellular function.[12] These MLOs play a vital role in tens of thousands of biological reactions in cells due to the dynamic properties, which allow their formation, dissolution and rapid transport of macromolecules with surroundings.[13] Many reactions occur in MLOs within a limited space ranging from Ångstroms (Å) to micrometers (μm), enabling specialized functions, including protein localization, supramolecular assembly, gene expression, gene transcription, RNA metabolism, minimizing cellular noise, genome packaging control and cell-cycle control (Figure 1.2).[14, 15, 16]

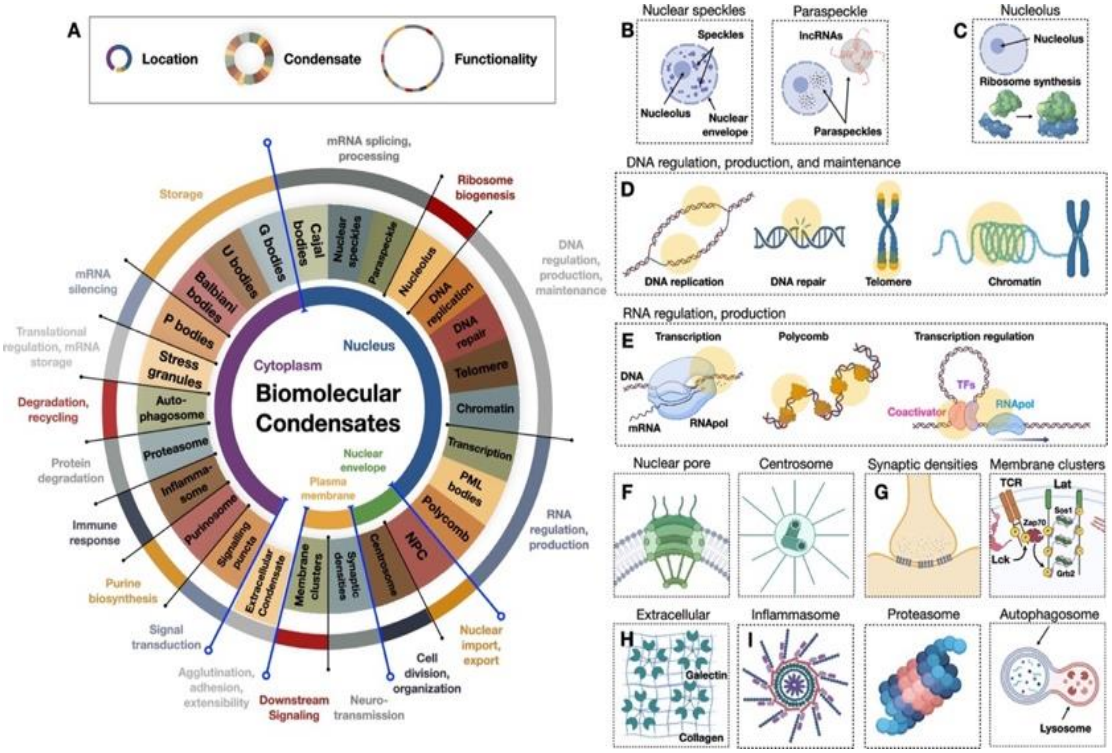

Figure 1.2. Names, locations and the functionality of MLOs in eukaryotic cells. [adapted from[17]]

Due to the diverse physical properties of different MLOs, they are capable of interacting with a wide range of small molecules (Figure 1.3), thereby performing various biological functions. Elucidating the connection between dynamics and their physical properties may enhance our understanding of MLOs' behavior in both physiological and pathological contexts. However, more and more studies have shown that abnormal MLOs are related to various diseases. When such normal functioning MLOs become abnormal, they typically exhibit changes in droplet properties, including fibers with poor dynamics, shape changes, size changes, and the appearance or disappearance of large numbers. Such abnormalities can directly affect cell function.

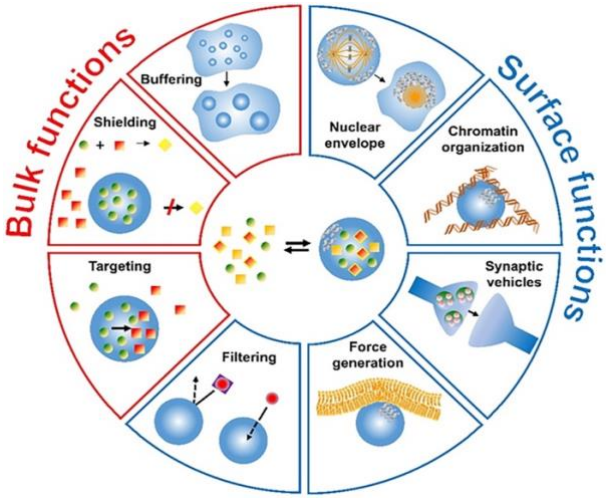

Figure 1.3. Various functions of MLOs with surroundings in eukaryotic cells [adapted from[18]]

1.1.1 The molecular language of LLPS and MLOs

The formation mechanism of MLOs has long been a mystery. Over the past almost 16 years, a new scientific field focused on MLOs has supported a completely new LLPS model, wherein many biomolecular interactions are associated with biomolecular condensates.[19] This discovery not only explains the formation mechanism of MLOs but also provides new methods, such as fluorescence recovery after photobleaching (FRAP) analysis, to explore the diffusion of components within MLOs in cell life activities.[20] Despite the diverse array of MLOs in eukaryotic cells, this common formation mechanism underlies their assembly within the cell.[21] MLOs, also known as biomolecular condensates (BMCs), are formed via LLPS and are highly dynamic.[22, 23, 24] For example, the components inside MLOs, such as P granules, can quickly exchange with those in the cellular environment and display liquid-like properties.[19] This

dynamic property is mainly due to the fact that the molecules therein are only bound by weak multivalent interactions rather than strong chemical bonds, allowing them to flow and disperse freely.[25] For this reason, biomolecules with special properties, especially proteins and negatively charged nucleic acids, are more likely to aggregate with other components in the cell through LLPS to form local high-concentration reaction units. The formation and maintenance of MLOs usually rely on the charge properties of their components. Molecules with positive or negative charges, especially specific positively charged amino acids and negatively charged nucleic acids, often form MLOs through electrostatic interactions.[10] For example, arginine-rich proteins can bind to acidic molecules due to their positive charge, while negatively charged RNA easily binds to positively charged proteins to form droplet-like structures. These charge-driven interactions not only enhance the intermolecular attraction but also promote the occurrence of LLPS. Gaining a better understanding of the normal and pathological functions of MLOs requires a clear understanding of the molecular interactions and how different biomolecules contribute to phase separation.[26]

In general, all MLOs are composed of protein, RNA, and/or DNA and formed via LLPS. Proteins undergoing LLPS contain intrinsically disordered low-complexity domains that can self-assemble into the condensed phase.

Short history of liquid-liquid phase separation

Phase separation is a well-known physical and chemical concept for a long time, especially in the polymer science and process engineering fields.[27] The study of phase separation in the description of biology has a long history of more than 100 years since the 1890s (Figure 1.4). Albert Kossel was the first person who report the phase separation of proteins and nucleic acids.[3, 28] Wilson and other bioscientists observed that cell was crowded with liquid droplets or coacervates.[29, 30]

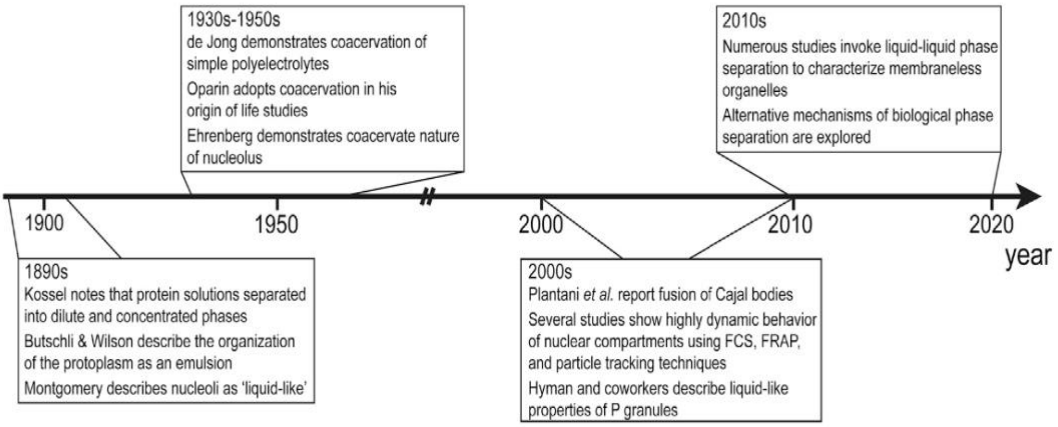

Figure 1.4. History of the development of LLPS. [adapted from[3]]

A resurgence of phase separation research in the field of biology can be traced back to 2009 when Hyman and Brangwynne discovered that P particles formed via phase separation and have liquid-like properties.[19] In 2012, Li et al. discovered that multivalent weak interactions can drive proteins and RNA in test tubes to form small droplets or colloids.[25] The concentration of protein in liquid droplets was approximately one hundred times higher than in the surroundings, and the development of *in vitro* experiments has made the study of phase separation much easier, which has become a breakthrough in the field of phase separation.

Weak Interactions driving LLPS

The LLPS can be divided into three types: segregative LLPS, simple coacervation and associative LLPS (Figure 1.5).

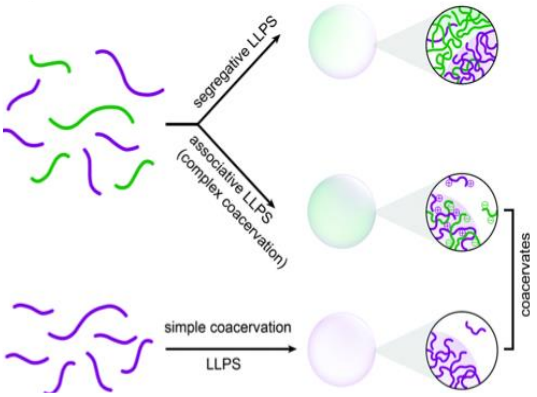

Figure 1.5. Types of liquid-liquid phase separation [adapted from[31]]

In a segregative LLPS, two soluble polymers are separated into two phases due to the repulsive interactions between them.[31,32] For example, when two incompatible polymers, such as Poly(ethylene glycol) (PEG) and dextran, separate into two aqueous phases, one phase rich in dextran and one phase rich in PEG.[33]

The repulsive interactions between polymers in the segregative LLPS can be rationalized by Flory-Huggins (FH) mean-field model between polymers and surrounding media,[34, 35, 36] which uses the χ-parameter (chi) to describe interactions. χ-parameter also called Flory-Huggins interaction parameter, Huggins parameter, Flory-Huggins parameter. The free energy per volume, F_{FH}, in FH model can be written in the following equation,[37]

$$\frac{F_{FH}}{K_B T} = \frac{1}{N}\phi ln(\phi) + (1-\phi)\ln(\phi) + \chi\phi(1-\phi) \qquad (1.1)$$

where the polymer volume fraction ϕ is defined as the ratio of the volume occupied by polymer monomers to the total volume of the solution. K_B is the Boltzmann constant, which is a proportionality constant between the temperature and energy. And the Boltzmann constant

equals to the ratio between Universal gas constant (R) and Avogadro number ($\widetilde{N}$), $K_B = \frac{R}{\widetilde{N}}$. And T is the temperature of the system. The parameter N denotes the degree of polymerization, representing the number of monomers in a single polymer chain, and influences the entropic contribution to the free energy.

In an associative LLPS, or complex coacervation, two or more biopolymers with oppositely charged are condensed into one dense liquid phase due to the attractive interactions between them.[31] For example, when two biopolymers carry the opposite net charge, they would undergo complex coacervation,[38] resulting in phase-separated systems with a dense phase and a dilute phase.[39] Attractive interactions can be driven by a wide range of molecular forces. These include non-specific forces, like electrostatic attractions, hydrogen bonds, hydrophobic effects, and aromatic stacking, as well as specific molecular recognition mechanisms, such as base pairing in nucleic acids and selective binding between multivalent proteins, which are considered heteropolymers with complex structures. Multivalent weak interactions mediated by the associative polymers, which are defined by Rubinstein and Dobrynin[36,40] that the macromolecules with attractive groups, like intrinsically disordered regions (IDRs),[41, 42] low-complexity domains (LCDs)[43] and prion-like domains (PLDs)[44,45] would facilitate LLPS and form dynamic complexes.[46, 47, 48] The framework of Flory-Huggins provides us with a model to describe the homopolymers and the solvent. In modern polymer theories, associative polymers can be described with sticker-and-spacer model (Figure 1.6). Stickers are groups participating in attractive interactions, whereas spacers are parts of the chain that do not significantly drive attractive interactions but modulate chain properties.[49] Concepts of scaffold (host) and clients (guest) concepts are used to describe the LLPS condensates and molecules partitioned within them via weak multivalent interactions.[50, 51] FUS IDR is a known scaffold protein, which is associated with neurodegenerative disease when abnormal phase separation occurrs.[52, 20, 53]

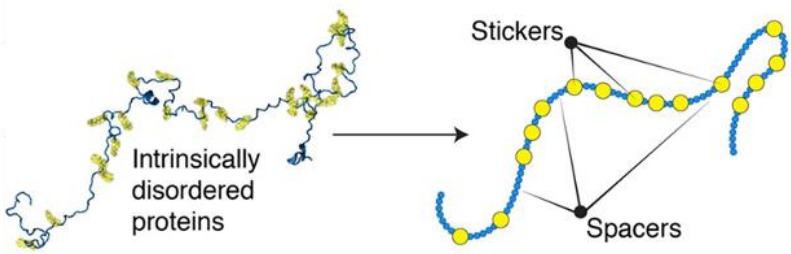

Figure 1.6. Stickers and spacers model of IDR. [adapted from [36]]

In a simple coacervation, or self-coacervation, only one single polymer, like IDRs, is condensed into one phase at a certain temperature, pH and salt concentration.[31, 54, 55] For example, a dense phase enriched in one biomolecule due to homotypic interactions between charged residues inside sequences.[41, 56] Associative polymers and polyampholytes are prone to undergo simple coacervation. Polyampholytes contain both positive and negative charges.

Recently, segregative and associative interactions have been combined to form complex droplets with functions that have not been realized for either aqueous two-phase or coacervation.[57, 58] Macromolecular inert crowding agents, such as PEG, dextran and Ficoll, are widely used in *in vitro* LLPS research.[59] These crowding agents could promote (or in theory also suppress) LLPS.[10, 59, 60, 61] Crowding agents like dextran, PEG, and Ficoll, can be observed in the condensed phase. [62, 63, 64]

Up to now, there are three different theories are proposed to explain LLPS, polymer theory, the multivalency theory and stickers and spacers theory (Figure 1.7).[65] According to the Flory-Huggins mean-field model, LLPS is driven by a competition of energy and entropy. Entropy is used to describe the disorder or randomness in a system. Multivalency theory describes multivalent polymers, such as IDRs and RNA, that mediate the formation of LLPS droplets when interacting with other molecules with more than three valences.[66, 65] Stickers and spacers

theory focus on the interaction part within the biomolecules. Flory-Stockmayer theory considers the valence of stickers and the bond formation probability and ignores the intrinsic connectivity due to spacers.[34, 36, 67]

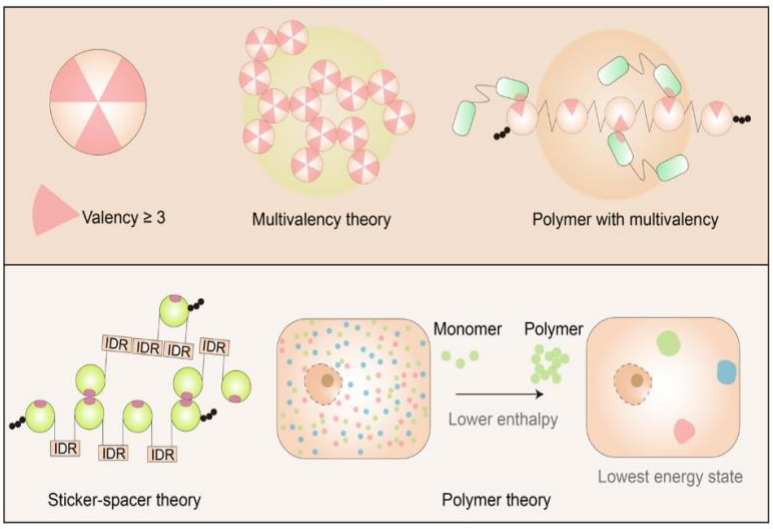

Figure 1.7. Three theories explaining LLPS [adapted from[65]]

The phase-separated molecules form LLPS through interactions including long range interactions (electrostatic interactions) and short range interactions (hydrophobic, cation-pi, and pi-pi) (Figure 1.8). The electrostatic interaction between oppositely charged polyelectrolytes determines the formation of LLPS-derived MLOs. The electrostatic interaction would be shielded by the high concentration of salt, and the liquid droplets would be dissolved.[68, 69] The cation-pi interaction is a weak intermolecular interaction between positively charged molecules and molecules with a pi-electron system, such as a benzene ring of Tyr, Phe, Trp, and His or pi orbitals on the side chain of Arg.[70, 71, 72, 73] The pi-pi interaction

is a weak intermolecular interaction between aromatic rings, such as the aromatic amino acids, and nucleobases like adenine.[74] In addition to the strength of intermolecular bonds, multivalency is also important to induce LLPS.[25,75, 76, 77] Hydrophobic interactions are weak interactions and hydrophobic interactions between molecules would be suppressed by the 1,6-hexanediol (1,6-HD).[78, 79, 80] So, 1,6-HD treatment is widely used for disrupting LLPS droplets both in cells and *in vitro*.[81, 82]

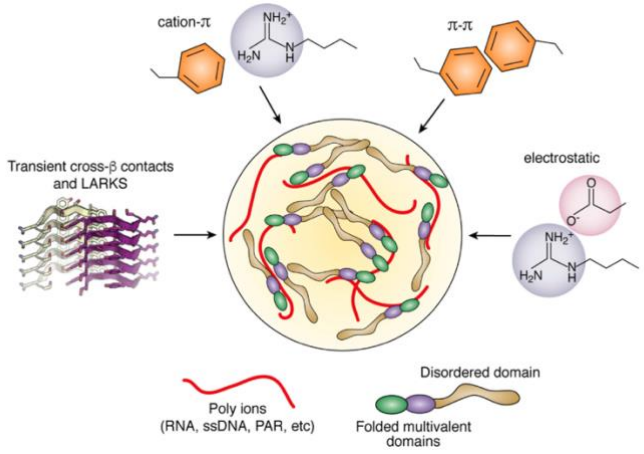

Figure 1.8. Weak interactions related to LLPS [adapted from[83]]

LLPS is a thermodynamic and non-equilibrium process in which a homogeneous solution spontaneously divides into two phases with different concentrations due to its properties. This spontaneous process can be observed easily in a tube with the naked eyes [84, 85] or by optical microscopy because the condensed phase becomes turbid, and the turbidity at 600 nm (optical density at 600 nm, OD_{600}) increases when the concentration of the components within the dense phase increases in LLPS.[86, 87] Many factors affect the initiation of LLPS, such as the concentration of the phase separation molecules, the environment stimulus of the surroundings,

including component concentrations, system temperature, salt, and pH (Figure 1.9). Environmental changes can regulate the morphology and structure of droplets by changing the parameters of liquid-liquid phase separation, which lays the foundation for cells to dynamically regulate the function of MLOs according to their physiological needs.

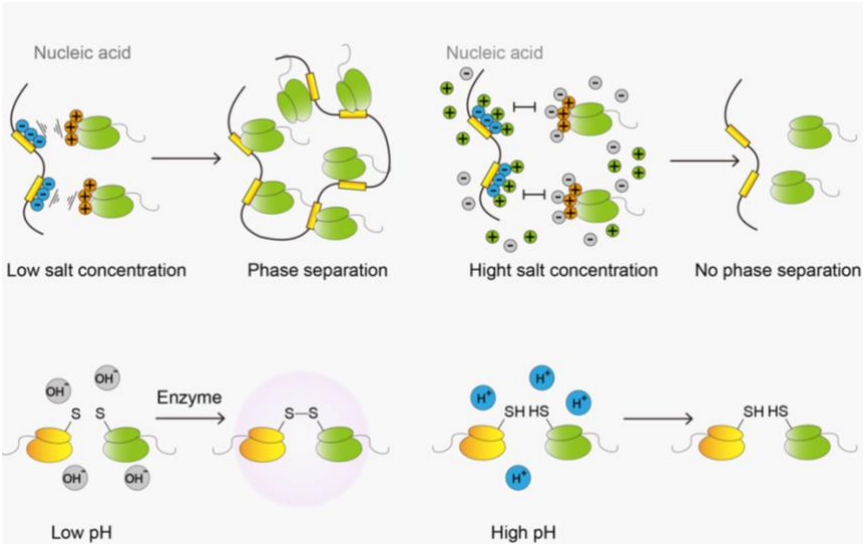

Figure 1.9. LLPS regulated by enviroment stimulus. [adapted from[65]]

These factors contribute to the dynamic nature of LLPS and its role in the formation and regulation of MLOs. The LLPS mechanism explains this important feature, that is, MLOs can rapidly transform between different morphologies in response to physiological signals such as changes in molecular concentration. Unlike the fixed membrane structure, this provides greater flexibility for MLOs to regulate their functional activities. In addition, LLPS also explains an important reason why MLOs are easily regulated by changes in the cellular microenvironment.

The next section will specifically introduce the main characteristics of these MLOs and specifically explain the role of their property changes in diseases.

1.1.2 Relationship between membrane-less organelles and amyotrophic lateral sclerosis

MLOs are small liquid-like droplets condensed by biomolecules (DNA, RNA and protein), lacking physical boundaries, allowing for rapid exchange of biomolecules with the surrounding cellular environment.[88] The dynamics of the liquid-like MLOs play an essential role in the cellular processes. These MLOs can exchange rapidly with surroundings and appear or disappear depending on the different stages of the cell and will also fuse when the cell encounters external stimuli (Figure 1.10). These characteristics all show the liquid-like properties of MLOs. Although the involvement of MLOs in crucial cellular processes is increasingly recognized, their specific functions remain unclear. The various cellular functions of MLOs underscore their significance in maintaining cellular function and homeostasis. Understanding how the biomolecules are organized inside cells helps us unveil the biological functions.[89] In contrast to conventional membrane-bound organelles with distinct roles, MLOs are often engaged in multiple functional pathways within the cell. This intricate involvement poses a challenge in comprehensively understanding their exact contributions, highlighting the need for further investigation into these dynamic cellular structures. However, alterations in the dynamics of MLOs can be linked to various disease-related processes, including cancer, neurodegeneration disease, such as amyotrophic lateral sclerosis (ALS), frontotemporal dementia (FTD), Parkinson's disease (PD), Alzheimer's disease (AD), viral infections, cardiac diseases and so on.[90, 91, 92] These findings emphasize the importance of understanding diffusion behavior of MLOs in both normal and pathological conditions to elucidate their potential roles

in disease development and progression. This section will provide an overview of the physical properties and diffusion dynamics of liquid MLOs formed via LLPS.

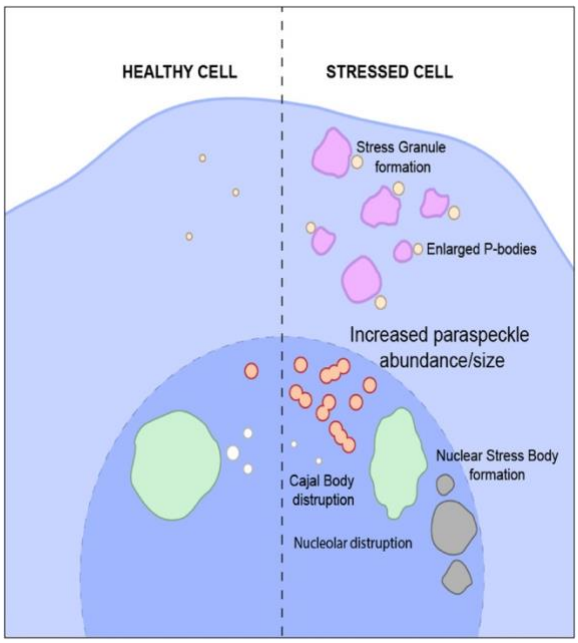

Figure 1.10. Various changes of MLOs in eukaryotic cells facing stress [adapted from[93]]

ALS, also known as Lou Gehrig's disease, is a neurodegenerative disease that causes the death of a large number of normally functioning neurons, leading to damage to upper and lower motor neurons, resulting in muscle atrophy and weakness as well as respiratory failure. ALS is mainly a sporadic case, of which about 5-10% are familial cases. More than 30 genes have been found to be associated with ALS, including the *C9ORF72* mutant gene, *TARDBP* gene, *FUS* gene, and *SOD1* (Figure 1.11). The protein products encoded by these genes, including arginine-rich dipeptides, TAR DNA-binding protein 43kDa (TDP-43) and fused-in-sarcoma (FUS), can form phase-separated droplets through LLPS or directly impair the function of

MLOs, causing the occurrence and development of ALS. For ALS, protein degradation and clearance pathways are disrupted, which are ubiquitin-proteasome system and autophagy.[94, 95, 96] In ALS disease, protein homeostasis or proteostasis is disrupted. Such proteins should have been degraded by the proteasome pathway, but because the function of the MLOs involved in this step is disrupted, the excess proteins cannot be degraded. The MLOs involved in related functions include PML nuclear Bodies, SGs and nucleoli.[97, 98] Therefore, understanding the abnormal droplets caused by such proteins or the abnormal MLOs associated with them is very useful for analyzing the progression of ALS. Most abnormal LLPS manifests as abnormal diffusion dynamics within the droplets, which in turn affects other cell functions and ultimately causes cell death.

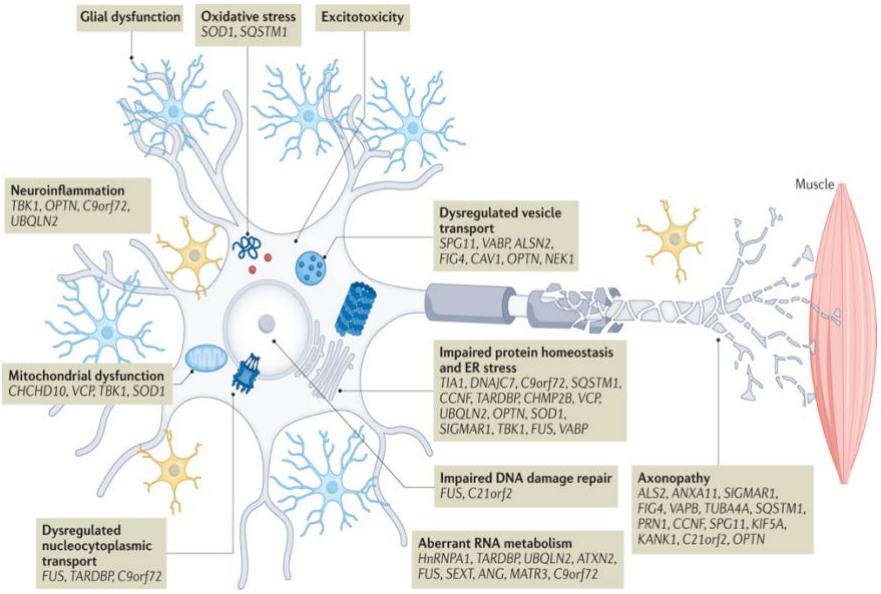

Figure 1.11. Risk factors and genes related to ALS [adapted from[99]]

Inclusion bodies in neurodegenerative disease

ALS is characterized by the presence of insoluble inclusion bodies that cannot be removed by detergents. These inclusion bodies are usually formed by misfolded ubiquitinated proteins. Currently, known misfolded proteins include tau, TDP-43, FUS, and superoxide dismutase-1 (SOD1).[10] There are many well-known inclusion bodies related to ALS disease, such as TDP-43 inclusion bodies. TDP-43 inclusion bodies are the first identified inclusion bodies and observed in ~97% of ALS.[10, 100, 101] In addition to TDP-43, recent studies have found that arginine-rich dipeptides, such as poly-PR and poly-GR can also form p62-inclusion bodies in ALS,[102] and these arginine-rich dipeptide inclusion bodies appeared earlier than TDP-43 inclusion bodies.[103] Moreover, the density of poly-GR inclusion bodies is higher than that in other arginine-rich dipeptide inclusion bodies.[104, 105] In this thesis, we analyze the spatial diffusion dynamics of arginine-rich dipeptide-derived MLOs.

Phase-transition of Membrane-less organelles

Some MLOs undergoing phase transitions would lose dynamics properties due to the pathological phase transition from a liquid-like form to a gel-like or solid phase (Figure 1.12).[92] More and more studies have proved that these MLOs with abnormal dynamics are responsible for cancer and neurodegenerative disease.[47, 106] Modulating the environmental salt concentration and pH can induce a liquid-to-gel transition of the droplets, leading to irreversible gel-like coacervations.[107, 108] However, even at physiological conditions, several key proteins in neurodegenerative diseases are concentrated in MLOs and observed to spontaneously mature into solid aggregates within hours *in vitro* and in living cell experiments.[20, 96] For example, ALS-related IDRs or LCDs, TDP-43 and FUS, undergo LLPS, resulting in their liquid-to-solid phase transition and accumulation into insoluble protein aggregates.[109, 110] Aberrant phase transitions may be at the core of many neurodegenerative

diseases. Similarly, arginine-rich dipeptides translated by *C9ORF72* mutant gene are also found to induce the transition of droplets from a liquid to a gel-like state, thereby disrupting the normal fluidity and molecular exchange of MLOs.[111, 112] C9-related ALS is the most common one found so far, accounting for more than 20% of familial ALS (fALS), and 5%-10% of sporadic ALS (sALS). The arginine-rich dipeptides are translated from the intron of *C9ORF72* mutant gene, which are highly positively charged and impair the MLOs' functions. In the next section, we delve into the crucial role of arginine-rich dipeptides in C9-related ALS, especially the diffusion dynamics of the MLOs related to this disease.

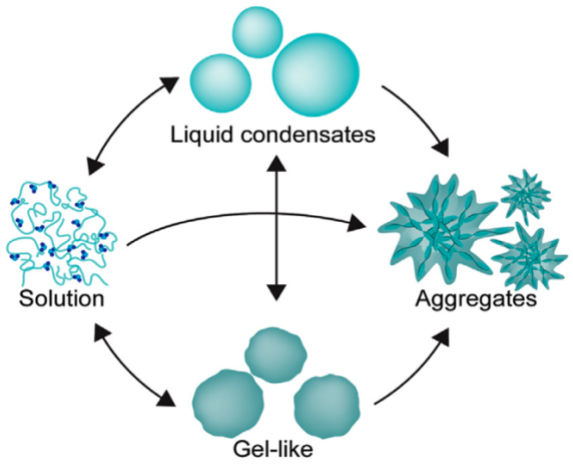

Figure 1.12. Phase transition [adapted from[113]]

Abnormal function of MLOs in C9-neurodegeneration disease

Three competing but non-exclusive mechanisms are currently recognized (Figure 1.13). First, the loss-of-function mechanism might result from the reduction of the normally functional *C9ORF72* gene and its product, namely haploinsufficiency.[114] Secondly, a gain-of-function

mechanism might result from the *C9ORF72* mutant gene producing a large number of hexanucleotide repeat sequences.[115] Third, a gain-of-function mechanism might result from non-coding intron in the *C9ORF72* mutant gene producing a large number of repeated toxic dipeptides, such as poly-PR, poly-GR and poly-GA through non-ATG translation.[116, 117]

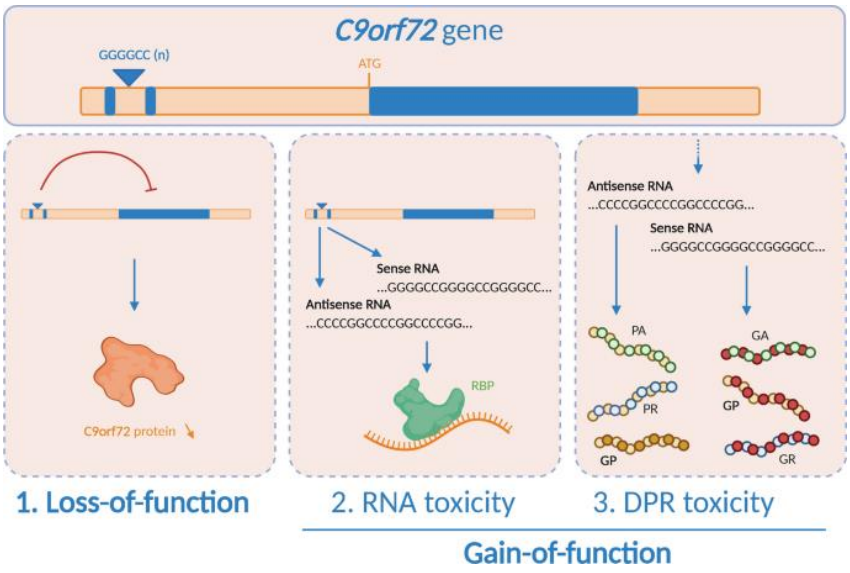

Figure 1.13. Three main mechanisms [adapted from[118]]

Based on the pathogenic mechanisms, several therapeutic strategies are emerging to help patients with C9-ALS disease (Figure 1.14).

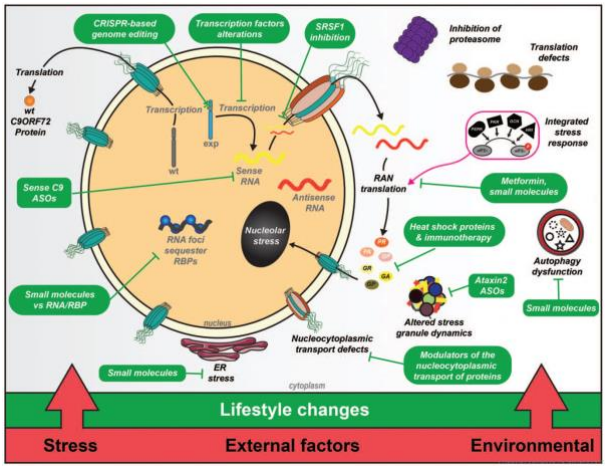

Figure 1.14. Therapeutic approaches for C9-ALS diseases [adapted from[119]]

There are many researches related to the first two explanations.[115, 114, 120] In this thesis, we focused on the third type mechanism related to arginine-rich dipeptides (Figure 1.15). Regarding the third type, arginine-rich dipeptides, poly-PR (repeats of proline and arginine) and poly-GR (repeats of glycine and arginine), have received much attention due to their strong toxicity.[121] In addition to arginine-rich dipeptides, poly-GA (repeats of glycine and alanine) also exhibited moderate toxicity and was able to be transmitted between cells. The toxicity of poly-GA sequences includes the formation of insoluble aggregates[122], inhibiting proteasome[123] and DNA damage by sequestering phosphorylated ATM.[124] The aggregates formed by poly-GA are the most toxic among all dipeptides.[125]

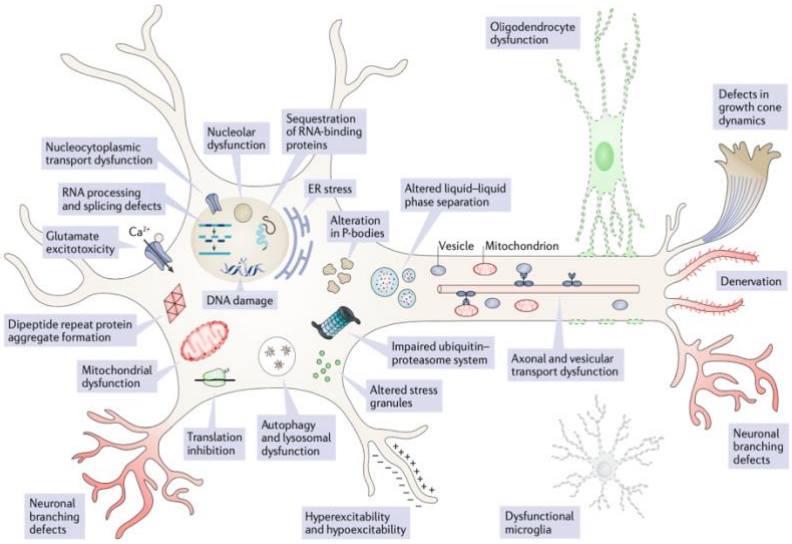

Figure 1.15. Various pathways related to irregular MLOs in neuron cells of C9orf72-mediated ALS/FTD [adapted from[120]]

Toxicity of Arginine-rich dipeptides

Arginine-rich dipeptides carry a large amount of positive charges and penetrate cell membranes effectively and even nuclear membranes.[117 ,126, 127] Poly-GR shows a stronger ability to penetrate membranes than poly-PR.[117, 127] Although the exact transmembrane mechanisms are not yet fully understood, the neurotoxicity of arginine-rich dipeptides has been widely acknowledged. These arginine-rich dipeptides induce translational repression, mitochondrial dysfunction, nucleolar dysfunction, and disruption of nucleocytoplasmic transport, which can ultimately cause neuron death (Figure 1.16).[128 129] In cell viability experiments, arginine-rich dipeptides ($(PR)_{20}$ and $(GR)_{20}$) have been proven to be toxic because they would change the morphology of cells and kill cells.[117] And poly-GR affects mitochondrial function[130, 131], disrupting nucleocytoplasmic transport and causing the aggregation of TDP-43.[132, 133] Some studies have shown that poly-PR is more toxic than poly-GR,[121, 134, 135] while other studies

suggest that poly-GR is more toxic.[104, 136, 137, 138,139] In a cell model of C9-ALS/FTD, poly-PR exhibited more significant toxic effects than poly-GR.[140] In experiment detection, LDH (lactate dehydrogenase) cytotoxicity kits are used to test the cytotoxicity of arginine-rich dipeptides in cells.[126] LDH is an enzyme present in the cytoplasm of cells that can participate in glycolysis. When cells are damaged or die, they will be released into the culture medium. Quantitative detection of the amount of LDH can be used as an indicator for determining the number of dead and damaged cells. The resulting ribotoxic stress response is mediated by ZAKα-induced neuron death.[137]

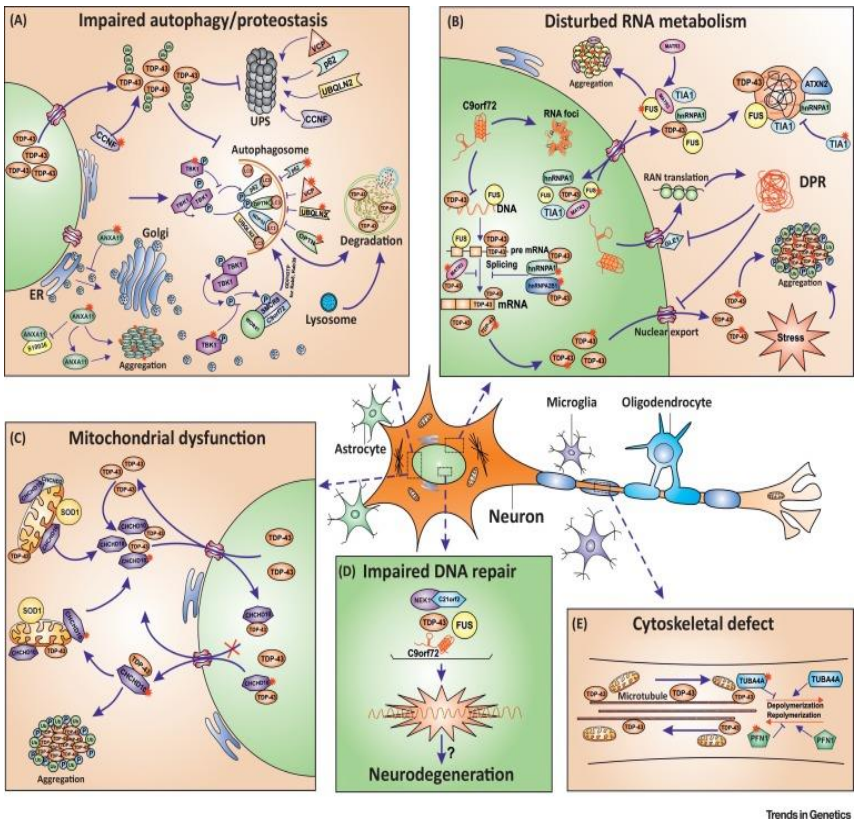

Figure 1.16. Key molecular mechanism of Pathogenesis of C9ALS-FTD disease [adapted from[141]]

Arginine-rich dipeptides are mainly distributed in the nucleolus of cells and also co-localize with stress granules, paraspeckles, and nuclear speckles and alter the diffusion dynamics of MLOs (Figure 1.17).[142] For example, they can alter the diffusion dynamics of nucleoli[142] and stress granules (SGs),[143] inhibit nucleolar stress and activate p53[144, 145], as well as the failure of Cajal bodies.[142] This vast toxic effect on multiple cellular functions revealed that there may be a mechanism that determines the toxicity of these toxic arginine-rich dipeptides. Chen *et al.* found that the repetitive structure of arginine-proline plays a vital role, whereas the proline in the repeat unit weakens the intermolecular interaction but contributes to the sites of multivalent interaction, enhancing the LLPS.[80] The dimension of poly-PR is larger than poly-GR when the chain length is the same.[135] Poly-GR adopts a more compact conformation compared to poly-PR. [135] Poly-PR binds more weakly to acidic molecules and forms fewer contacts with them compared to poly-GR.[135] Proline is more hydrophobic than glycine. Proline is much stiffer than glycine because of the cyclic structure of its side chain. Proline contributes to the rigidity of the protein structure, and glycine contributes to the flexibility of the protein backbone.[135] Stiffness of the components would also affect the molecular dynamics of MLOs.[146, 147] Understanding the physical properties of arginine-rich dipeptides that regulate their molecular dynamics within MLOs in cells is of great significance for revealing their mechanism in the pathological process of ALS.

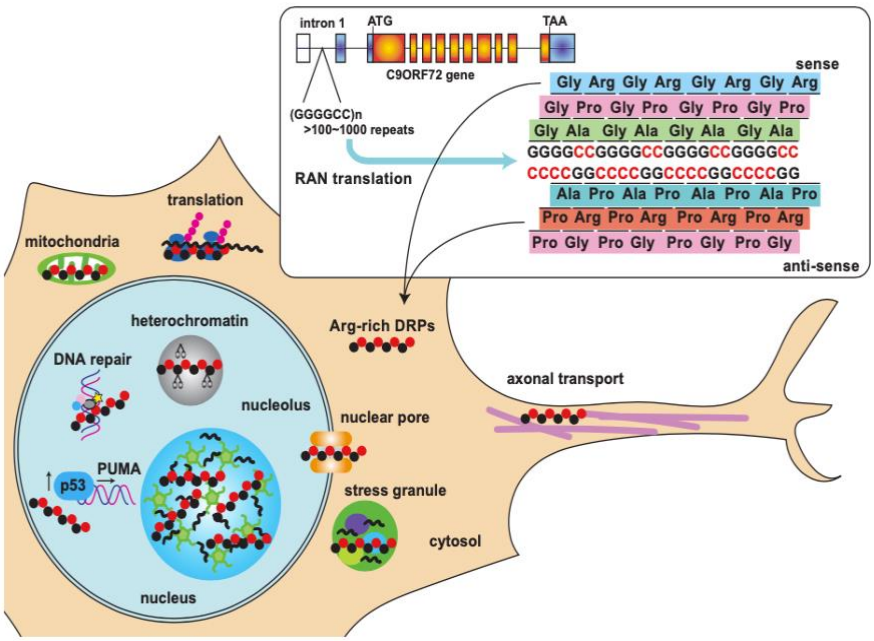

Figure 1.17. Various dysfunctions of MLOs in cells of C9ORF72-mediated disease [adapted from[148]]

Further studies have revealed that arginine-rich dipeptides affect various RNA-related processes (Figure 1.18), including the inhibition of protein translation[126, 142], RNA editing[149] and RNA splicing.[117, 150] These protein translation dysfunctions usually start from the nucleoli within cells. The nucleoli of neurons in ALS patients typically shrink, but in the presence of poly-GR, the nucleoli become relatively larger.[151] However, enlarged nucleoli do not necessarily indicate an active RNA-related process. Notably, despite having the same length of repeat sequences, poly-PR is co-localized with nucleoli, whereas poly-GR is found to be only sporadic around the nucleolus and largely appears in the cytoplasm. This difference in cellular localization is believed to be related to the rigidity of the dipeptide sequence[135] and charge properties.[134] Even when co-localized in the nucleolus, poly-GR exhibits slower diffusion within MLOs than poly-PR.[134] Poly-GR shows stronger interactions with nucleolin (NCL) than

poly-PR.[142] Consistent with this observation, FRAP experiments for GFP labeled NCL single nucleolus have demonstrated that poly-GR repeat polymers exhibit greater efficacy than poly-PR in diminishing the mobile fraction and fluorescence recovery rate of GFP labeled NCL.[142] Understanding these molecular interactions is crucial for deciphering the pathogenic mechanisms of ALS.

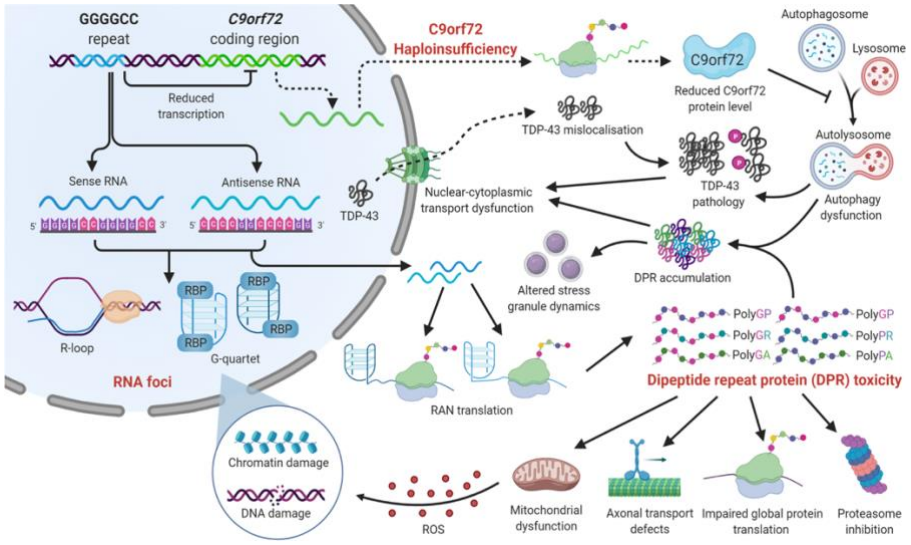

Figure 1.18. Disease mechanism of C9ALS-FTD [adapted from[128]]

Arginine shows a strong preference for stacking with adenine base (Figure 1.19). Cation-π interactions can occur between the cationic side chains of arginine and aromatic side chain of adenine base with a broad electronegative surface,[72] arising as a result of strong attractive forces between positively charged parts and the π-electron cloud of aromatic groups.[152] In addition, arginine can also form a stable hydrogen bond network with the sugar-phosphate backbone of RNA.[153] The delocalized π electrons of the arginine guanidinium group can participate in π–π interactions with RNA bases.[154, 155 156] This multivalency of arginine-rich dipeptides plays a vital role in cytotoxicity. Also, high salt concentrations can induce the reentrant phase behavior of arginine-rich peptides.[157, 158] The hydrophobicity of arginine is the

determining factor giving rise to the reentrant phase behavior and tunable viscoelastic properties of the dense LLPS phase.[159]

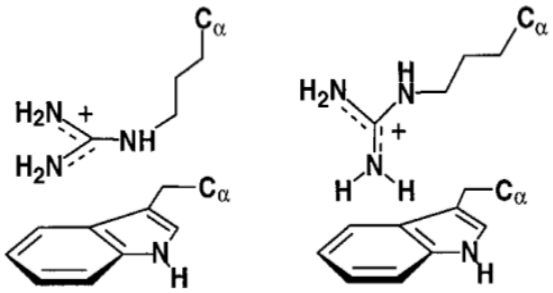

Figure 1.19. Cation-π interactions of the arginine sidechains. [adapted from[71]]

In summary, arginine-rich dipeptides form MLOs via LLPS through electrostatic, hydrophobic, and cation-π interactions, thereby disrupting intracellular RNA metabolism, nucleolar function, and stress response. These findings emphasize the importance of understanding the physical behavior of these arginine-rich dipeptides in cells, which will help reveal their specific roles in the pathogenesis of ALS.

FRAP analysis for diffusion dynamics in coacervations

It remains difficult to determine whether abnormal MLOs contribute to ALS pathogenesis as conventional biochemical tools cannot manipulate the phase separation processes that drive their formation. However, connections between the diffusion dynamics of MLOs and disease have been established.

In the 1970s, Axelrod and collaborators developed the FRAP technique to study the mobility of the protein within cells.[160, 161, 162] FRAP technique was applied to measure the diffusion of

lipid molecules on cellular membranes.[163] Now, it is widely used for studying the dynamics in cell biology, including the dynamics of cytoskeletal, vesicle transport, cell adhesion, mitosis, the structure of chromatin, transcription and protein recycling.[164] FRAP experiments connect the dynamics of molecules to their corresponding significance in cells.[162] In recent years, with the further study of MLOs, FRAP experiments serve as a gold standard for studying the diffusion of components within MLOs, both *in vivo* and *in vitro*.[18, 165]

The FRAP method is often used to assess the molecular diffusion dynamics and spatial heterogeneity within MLOs.[2, 10] Many parameters can affect the recovery rate, such as the size of the liquid droplets and the size of the bleach areas within the droplets.[2] However, FRAP can be affected by the binding strength and the multivalences of components within liquid MLOs, as well as by the fluorescent labeling dyes themselves, which may alter the interactions within liquid droplets.[10]

The photophysical process of fluorescence is depicted by the Jablonski diagram (Figure 1.20). Fluorophore-containing molecules, such as Rhodamine B (RhB), fluorescein and tetramethylrhodamine (TAMRA), emit fluorescence at a larger wavelength compared to excitation light. Fluorescein, Rh B and TAMRA are well-known xanthene dyes that contain a chromophore with a three-ring π-conjugated structure, which serves as the functional unit of fluorescence.

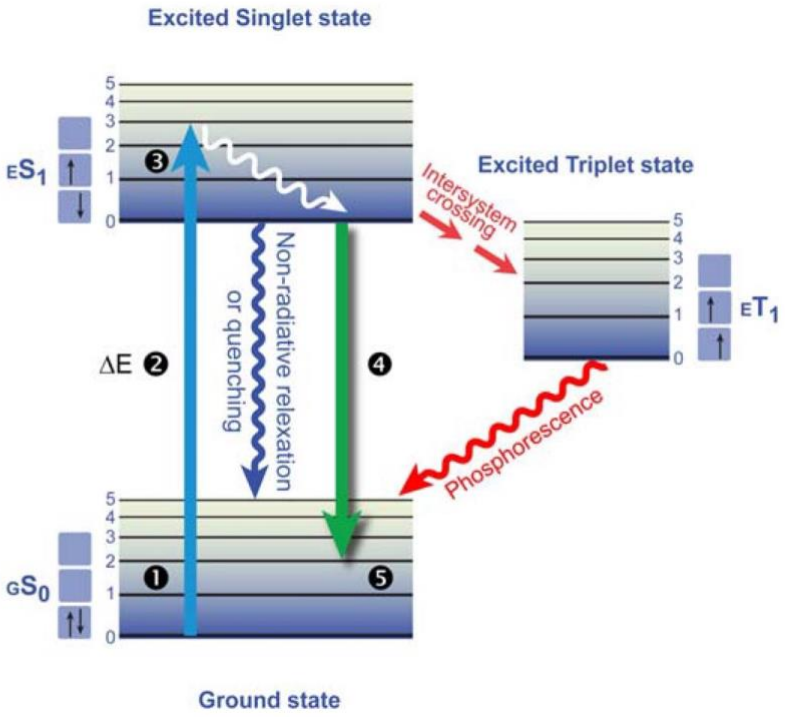

Figure 1.20. Jablonski diagram of fluorescence [adapted from[166]]

The limitation of the fluorescent labeling method has promoted the development of label-free and non-invasive techniques, such as Raman spectroscopy, for MLOs analysis. In this thesis, the liquid droplets formed arginine-rich dipeptides and poly-A RNA via LLPS were subjected to photobleaching. The fluorescence recovery time showed significant differences due to the different charge properties of the arginine-rich dipeptides and the small dye molecules which are used to label the liquid droplets.

1.2 Introduction to Raman spectroscopy

When incident light is irradiated on sample molecules, due to the heterogeneity of the target sample, a small portion of the light (0.1%) deviates from its original propagation direction,

which is called light scattering. In these light scattering processes, two situations occur: elastic scattering and inelastic scattering, depending on whether the wavelength (frequency) of the scattering light changes (Figure 1.21). In the vast majority of cases, elastic scattering (Rayleigh scattering) usually occurs when the wavelength of the light is shorter than the size of the target molecules without changing its wavelength (frequency). The scattering direction is random and evenly distributed in all directions. In the rare case (one in one million), the inelastic scattering (Raman scattering) occurs by changing its wavelength (frequency). When the scattering frequency of the scattering light decreases, the inelastic scattering is called Stokes scattering, which appears at lower wavenumbers. When the scattering frequency of the scattering light increases, the inelastic scattering is called anti-Stokes scattering, which appears at higher wavenumbers. The intensity of the anti-Stokes scattering is three orders of magnitude lower than the intensity of Stokes scattering due to the Boltzmann distribution systems.

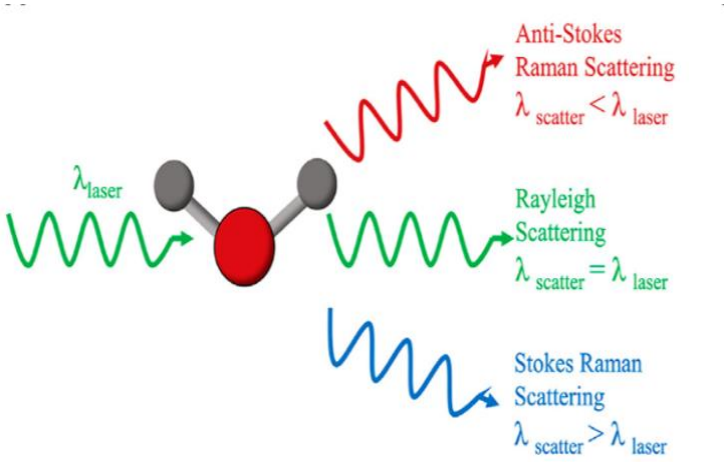

Figure 1.21 Principle of Raman scattering. Molecular mechanism of Raman scattering and Rayleigh scattering. [adapted from[167]]

1.2.1 Raman scattering

In 1923, the Austrian theoretical physicist Adolf Smekal first theoretically predicted the inelastic scattering of photons.[168] In 1928, the Indian physicist C.V. Raman first discovered the existence of inelastic scattering of light and was awarded the 1930 Nobel Prize for this discovery.[169] Frequency changes were discovered in the scattered light of the CCl_4 liquid. Hence, the wavelength (frequency) changes of the scattering light are named Raman scattering (also named combination scattering in Russian literature). In the same year, the Soviet physicists G.S. Landsberg and L.I. Mandelstam also observed frequency changes in scattered light in quartz.[170] Raman scattering can be explained from two perspectives: classical electromagnetic theory and quantum theory.

According to the classical electromagnetic theory, when the incident light (electromagnetic radiation) interacts with the molecules of matter, the external electric field (**E**) of the light will polarize the molecule by shifting the positively charged nuclei and negatively charged electrons in the opposite direction, causing the electron cloud to be periodically disturbed relative to the atomic nuclei. The molecules will produce oscillating induced dipole moments (**μ**). The induced dipole moments **μ** can be written in the following equation,

$$\boldsymbol{\mu}=\alpha\mathbf{E} \qquad (1)$$

where α is the polarizability tensor of the molecules. The oscillating electric dipole is induced by the electric field of incident electromagnetic radiation. If the polarizability of the molecules is not related to the time, the dipole moment **μ** is proportional to the electric dipole rate generated by the circular frequency ω_0 oscillating coil (corresponding to frequency $\omega = 2\pi\nu$, or wavenumber $\tilde{\nu} = \nu/c$, where c is the speed of light), namely Rayleigh scattering. If the

dipole oscillates with the frequency ω_j, and the vibration affects the polarizability of the molecules and makes it periodically change in time, the polarizability of the molecules α can be written in the following formula:

$$\alpha = \alpha_0 + \alpha_j \cos \omega_j t \quad \textbf{(2)}$$

where α_0 is an equilibrium polarizability tensor and α_j is a polarizability tensor associated with ω_j.

Thus, the final equation can be written in the following equation:

$$\mu = \alpha_0 \varepsilon_0 E_0 \cos \omega_0 t + \alpha_j \varepsilon_0 E_0 \cos \omega_0 t \cos \omega_j t \quad \textbf{(3)}$$

$$\mu = \alpha_0 \varepsilon_0 E_0 \cos \omega_0 t + \frac{1}{2} \alpha_j \varepsilon_0 E_0 [\cos(\omega_0 - \omega_j) t + \cos(\omega_0 + \omega_j) t] \quad \textbf{(4)}$$

where the induced dipole moment frequency can be the following three types: ω_0 and $\omega_0 \pm \omega_j$. The frequency less than the frequency ω_0 is Stokes scattering (i.e. $\omega_0 - \omega_j$), while that at a higher frequency (i.e. $\omega_0 + \omega_j$) is anti-Stokes scattering. The Raman scattering is regulated by the frequency of the vibration.

In Raman scattering, the intensity of total Stokes Raman scattering is a very feeble effect and is proportional to the Raman cross-section, the excitation laser intensity and the number of target molecules (Figure 1.22). Because of the extremely small Raman cross sections, typically 10^{-30}-10^{-25} cm^2/molecule, at least $\sim 10^8$ molecules (about 0.1 mM) are necessary to generate a measurable normal Raman scattering signal.[171] Raman scattering is accompanied by Rayleigh scattering. The intensity of Rayleigh scattering is about 3-5 orders of magnitude greater than that of Raman scattering.

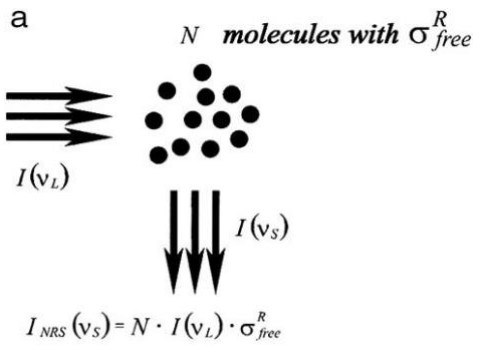

Figure 1.22 Raman scattering. [adapted from[171]]

According to the explanation of quantum theory, the scattering effect of light is expressed by an energy level diagram (Figure 1.23). When an incident photon collides with a molecule elastically, the electrons in the ground state of the molecule are excited by the excitation light and transition to an excited virtual state. The molecule is unstable in the excited virtual state and then transitions back to the ground state from this energy level. In this process, no energy exchange occurs between the photon and the molecule, and the direction of motion of the photon changes, but the frequency of its transition radiation does not change. This is Rayleigh scattering. When a photon collides with a molecule inelastically, the electrons in the ground state of the molecule are excited by the excitation light and may transition to a virtual state and immediately return to the ground state vibration excited state. In this process, the photon transfers energy to the molecule, which is converted into the vibrational energy or rotational energy of the molecule, and the scattering frequency of the photon decreases. This is Stokes scattering. When photons collide inelastically with molecules, the electrons in the ground state vibration excited state in the molecules are excited by the excitation light and may transition to the excited virtual state. This energy level is unstable and quickly returns to the ground state.

In contrast to the Stokes scattering process, in this process, the molecules transfer energy to the photons. Because the photons obtain part of the energy of the molecules, in addition to the change in the direction of movement, their scattering frequency becomes larger than before. This is the anti-Stokes line (anti-Stokes scattering). In quantum theory, Stokes and anti-Stokes Raman scattering are equally likely processes. However, for molecular clusters, they follow the Boltzmann distribution. Since most molecules are in the ground state energy level in the Boltzmann distribution, the number of ground state particles is much larger than the number of vibration excited state particles, and Stokes Raman scattering is more likely to occur. Therefore, Stokes Raman scattering is always stronger than anti-Stokes Raman scattering. Stokes Raman scattering is detected in the Raman spectrum, and the intensity of Stokes lines (Raman scattering) is greater than that of Anti-Stokes lines. These pairs of new lines belong to Raman scattering, and they are symmetrical with respect to the Rayleigh line.

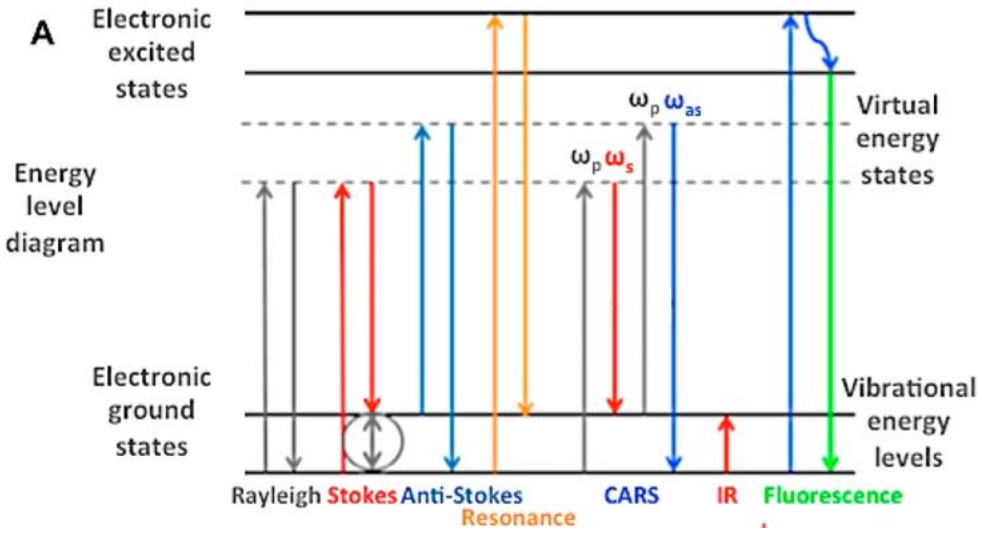

Figure 1.23. Energy level diagram of Raman scattering. [adapted from[172]]

The difference between the frequency of the Stokes line or anti-Stokes line and the frequency of the incident light is the Raman shift. This shift can characteristically represent the molecular vibration mode and can be used to reflect the structural information of the molecule. The frequency shift is the difference between the spectrum line and the original frequency of the incident light. The unit is wavenumber, cm^{-1}. The frequency shift depends on the structure inside the medium and has nothing to do with the type of laser (power, excitation line). For the same substance, the frequency of Raman scattering changes with the change of the frequency of the incident light, but the Raman shift remains unchanged. Therefore, the Raman shift is related to the molecular vibration or rotation energy level and has nothing to do with the frequency of the incident light. Since different molecules have different vibration and rotation energy levels, there are different Raman shifts, so each substance has its own characteristic Raman spectrum. Therefore, Raman spectroscopy is a spectral analysis technology that can fingerprint the structure and composition of a substance. Since the discovery of the inelastic scattering of light, known as Raman scattering effect, Raman spectroscopy has become a valuable technology in various research fields, including biology, chemistry, and medicine. Raman spectroscopy can provide a lot of information about molecules and their structures by detecting the Raman peak frequencies and relative intensities of different vibration modes, characterizing their interactions with the environment, and monitoring their changes during reactions. In addition, since the intensity of the Raman peak is proportional to the number or concentration of molecules, it can also be used for quantitative analysis.

It can provide rich molecular information about the sample in a non-destructive manner. However, early Raman spectroscopy had poor sensitivity and long signal acquisition time due to poor light sources and low spectral intensity, which prevented the widespread application of Raman spectroscopy. In recent years, the progress of laser light sources, new detectors, high-performance computers and microscopic techniques has greatly promoted the extensive application of Raman spectroscopy in some fields.

1.2.2 Bio-applications of Raman spectroscopy

As a non-invasive optical detection technology, Raman spectroscopy has rapidly gained traction in the biomedical field in recent years, with a wide range of application prospects. It reflects the types and internal structures by characterizing the vibration information of sample molecules. This technique is fast, highly specific, and non-invasive. Various proteins, nucleic acids, lipids, and polysaccharide molecules in the human body have specific Raman spectra. Biological molecules exhibit unique Raman spectra.[173, 172, 174, 175] In the late 1960s, R. C. Lords and G. J. Thomas Jr. first recorded the Raman spectra of various nucleic acids and further improved the Raman instrument.[176] For instance, Raman spectrum of nucleic acids contains a large number of characteristic bands from sugars, phosphate backbones and bases, providing useful information for analyzing nucleic acid backbone conformation and base pairing (Figure 1.24).[177]

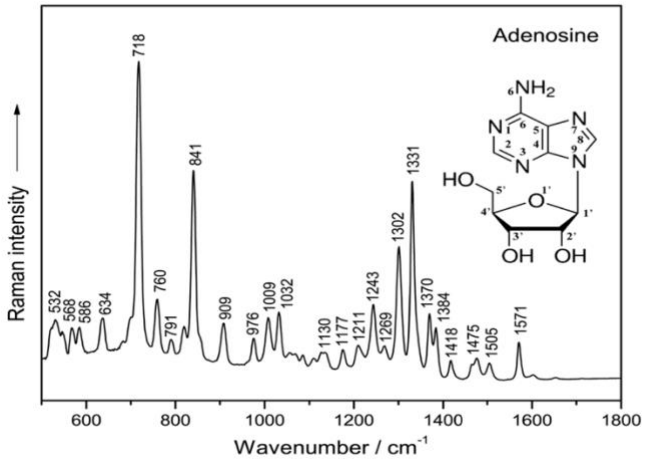

Figure 1.24. Raman spectrum of adenine RNA. [adapted from[177]]

Alterations of the structure and composition of small biomolecules in MLOs can significantly influence their cellular functions and even lead to disease development.[14, 178, 179] The Raman spectra—particularly the relative intensities of molecular peaks—undergo characteristic changes by changes to the protein composition.[180] Figure 1.25 illustrates how Raman spectroscopy can be used to measure the concentration of biomolecules within MLOs.[181] Raman spectra were collected both inside and outside the liquid droplets. The results show that the technique can distinguish characteristic peaks within the droplets compared to the surrounding buffer solution. Thus, further analysis of the Raman spectrum can reveal the structural conformational changes of the proteins during LLPS.[182] In particular, the ratio of the peaks is one of the most important values indicating the interaction of the biomolecules. Monitoring the ratios between characteristic peaks would be essential for the understanding of the potential interactions of many molecular interactions inside MLOs.[180] To this end, many efforts have been made in the development of Raman-based molecular interaction for detecting molecular interactions. The basic principle is to use ratios between characteristic peaks of molecules whose Raman spectra vary in different situations. Therefore, Raman spectroscopy can be used to detect the molecular interactions and dynamics of various components of MLOs.

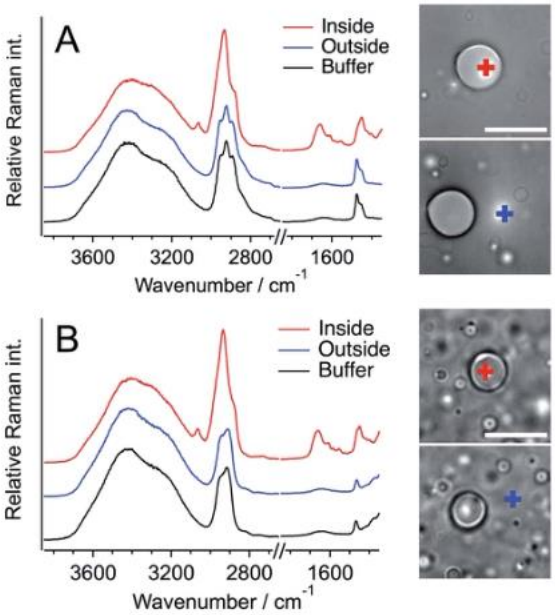

Figure 1.25. Raman spectra of the inside and outside of liquid droplets, respectively. [adapted from[181]]

1.3 Problem statement and research objectives

1.3.1 Problem statement

Membrane-less organelles (MLOs) formed via liquid-liquid phase separation (LLPS) play vital roles in various cellular processes, exhibiting highly dynamic behaviors, with internal components freely exchanging with the surroundings which leads to complex spatiotemporal dynamics of biomolecules in living cells.[183, 184] LLPS homeostasis is highly dependent on the fluidity of the LLPS-derived liquid droplets, and this property is often assessed *in vivo* or *in vitro* using the fluorescence recovery after photobleaching (FRAP) technique.[156, 80] Various weak interactions, including electrostatic interactions, π-π interactions, cation-π interactions, hydrophobic interactions, contribute to the formation of the liquid droplet.[78, 185, 186] These interactions, along with those between droplet components and their surroundings, generate characteristic gradients from the droplet center to its inner boundary and influence their dynamic properties (Figure 1.26). Consequently, diffusion behaviors within droplets are expected to be spatially heterogeneous. However, the normal size of MLOs in living cells ranges from a few hundred nanometers to around two micrometers, which is quite small for optical microscopy. And the contents in MLOs in living cells are quite complex. It is difficult to study the MLOs in living cells as model systems. Although prior fluorescence microscopic studies using fluorescently labeled biomolecules have revealed different droplet dynamics *in vitro,*[156] the underlying causes of these differences remain poorly understood. The diffusion behavior may vary in different liquid droplets caused by charged properties of biomolecules. Understanding how charge properties influence droplet dynamics is key to uncovering these mechanisms. While FRAP has been used to analyse diffusion behaviors, characterizing the spatial heterogeneity of individual droplet behaviors remains challenging. Considering the dysregulation of the molecular diffusion dynamics in LLPS-derived MLOs, understanding the

mechanisms also has medical significance. In particular, in neurodegenerative diseases such as amyotrophic lateral sclerosis (ALS) and frontotemporal dementia (FTD), abnormalities in LLPS show features that are closely related to disease progression.

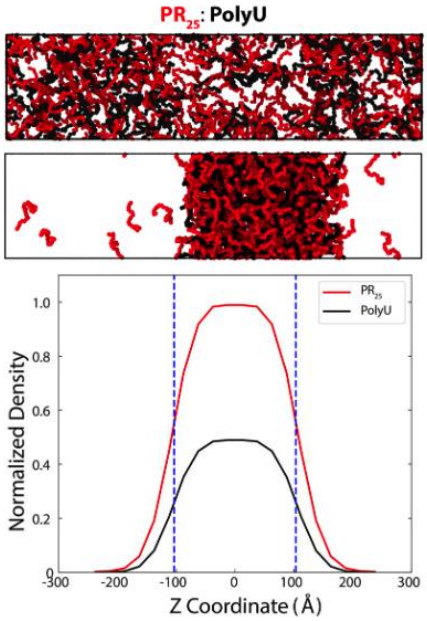

Figure 1.26. Density concentration within LLPS-derived biomolecular condensates. [adapted from[56]]

Specifically, we focus on droplets containing RNA and arginine-rich dipeptides, such as poly(proline-arginine, PR) and poly(glycine-arginine, GR), which are translated via repeat-associated non-ATG (RAN) translation of the intron of mutated *chromosome 9 open reading frame 72* (*C9ORF72*) gene, which are related to familial ALS and FTD. Both poly-PR and poly-GR are positively charged and have the same overall net charge, causing abnormal MLOs' dynamics and inhibiting the processing of ribosomal RNA (rRNA) and translation of protein.[126, 142] Although poly-PR and poly-GR could accumulate in the nucleolar and have similar propensities for LLPS, the diffusion of poly-GR is slower than that of poly-PR both *in cellular*

and *in vitro*.[142, 134] The reason responsible for these diffusion differences remains unclear. Based on the charge properties of arginine-rich dipeptides, different dynamics were observed by FRAP *in vivo* (Figure 1.27). Recent studies suggest that variations in charge distribution along the dipeptide sequence significantly affect binding energies and dynamics of droplets, while the net charge is uniform.[134, 185] It is very important to understand these dynamics for elucidating the underlying mechanism of dipeptide toxicity on MLOs and their contribution to the pathogenesis of neurodegenerative diseases.

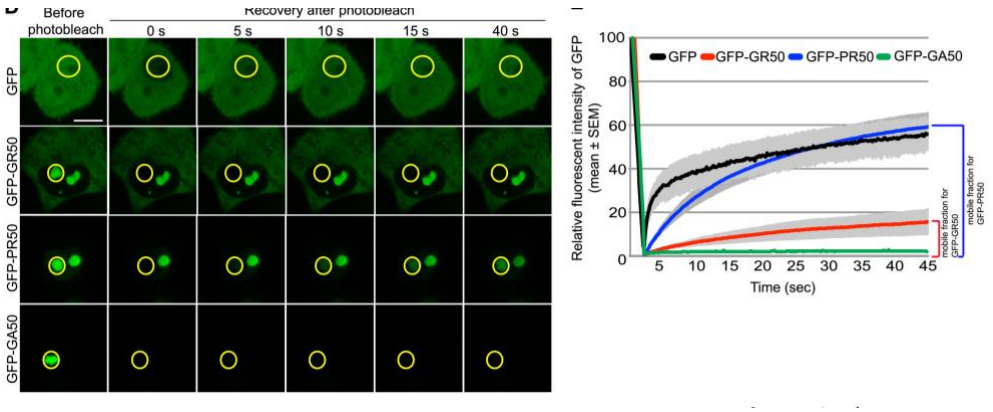

Figure 1.27. Fluorescence recovery and diffusion dynamics of MLOs in cells obtained by FRAP analysis, respectively. [adapted from[142]]

In this work, we employ spatially resolved FRAP analysis and Raman spectroscopy to droplets formed by mixing arginine-rich dipeptide repeats with poly-A RNA via LLPS. Our findings suggest that Raman spectroscopy is a powerful tool to effectively monitor spatial RNA and peptide concentration gradients within individual droplets, which can be correlated with FRAP analysis. Thus, Raman analysis can provide additional insights into the characteristics of these

droplets, contributing to a more comprehensive understanding of their spatial distribution and molecular diffusion in the context of neurodegenerative diseases.

1.3.2 Research objectives

(1) Development of a method to study molecular diffusion behavior and spatial distribution of LLPS-derived liquid droplet *in vitro* model systems with appropriate size

As aforementioned, abnormal diffusion behaviors of LLPS-derived liquid droplets play a vital role in neurodegenerative diseases. The arginine-rich dipeptides have the capability to undergo LLPS with components inside the MLOs that could have a detrimental effect on fundamental cellular processes, potentially leading to injury or death in motor neurons. The liquid droplets exhibit highly dynamic behavior, with internal components freely exchanging with the surrounding media, leading to the complex spatiotemporal dynamics of biomolecules in living cells. The fluidity of these liquid droplets is a critical factor in LLPS homeostasis. However, the size of MLOs is small, ranging from a few hundred nanometers to a few micrometers, which is quite similar to the spatial resolution of optical microscopy. Characterizing the spatial heterogeneity in individual droplets remains a challenging aspect. To overcome this size limitation, in this study, we would like to make a simple *in vitro* model system by forming liquid droplets with proper size with arginine-rich dipeptides and poly-A RNA via LLPS. This *in vitro* model system gives us the chance to connect the diffusion dynamics and molecular distributions of individual LLPS liquid droplets behavior across the liquid droplets. In this study, we would like to figure out spatial heterogeneity with Raman spectroscopy and heterogeneous diffusion dynamics at the center and edge of liquid droplets using FRAP, namely, developing a method to study spatial diffusion behaviors and spatial distribution of the *in vitro* LLPS liquid droplet model system.

(2) Development of a method to examine heterogeneity within individual liquid droplets

After figuring out spatial density gradients and heterogenous diffusion dynamics within LLPS droplets, in this study, we would like to further study density heterogeneity in LLPS-derived droplets formed via poly-A RNA and arginine-rich dipeptides with different charge properties, by analysing spatial Raman intensity ratio and spatially heterogeneous diffusion dynamics of molecules within indivadual droplets. As aforementioned, spatial density gradients and heterogeneous diffusion dynamics within droplets. However, variations in charge distribution along the dipeptide sequence significantly affect binding energies and droplet dynamics, even when the overall net charge is identical, therefore, in this study, we would like to prepare and analyse LLPS droplets consisting of components with different charged properties, formed by arginine-rich dipeptides with distinct charge properties using Raman spectroscopy and FRAP analysis. FRAP analyses of RNA and various small dye molecules with different charges, in combination with Raman spectroscopy, are performed to further investigate the heterogeneity within LLPS-derived droplets.

1.4 References

1 Banani, S. F.; Lee, H. O.; Hyman, A. A.; Rosen, M. K. Biomolecular condensates: organizers of cellular biochemistry. *Nat Rev Mol Cell Biol* **2017,** *18* (5), 285-298.

2 Alberti, S.; Gladfelter, A.; Mittag, T. Considerations and Challenges in Studying Liquid-Liquid Phase Separation and Biomolecular Condensates. *Cell* **2019,** *176* (3), 419-434.

3 King, J. T.; Shakya, A. Phase separation of DNA: From past to present. *Biophys J* **2021,** *120* (7), 1139-1149.

4 White, J. P.; Lloyd, R. E. Regulation of stress granules in virus systems. *Trends Microbiol* **2012,** *20* (4), 175-183.

5 Arimoto-Matsuzaki, K.; Saito, H.; Takekawa, M. TIA1 oxidation inhibits stress granule assembly and sensitizes cells to stress-induced apoptosis. *Nature Communications* **2016,** *7* (1), 10252.

6 Nover, L.; Scharf, K. D.; Neumann, D. Formation of cytoplasmic heat shock granules in tomato cell cultures and leaves. *Mol Cell Biol* **1983,** *3* (9), 1648-1655.

7 Collier, N. C.; Heuser, J.; Levy, M. A.; Schlesinger, M. J. Ultrastructural and biochemical analysis of the stress granule in chicken embryo fibroblasts. *J Cell Biol* **1988,** *106* (4), 1131-1139.

8 Marcelo, A.; Koppenol, R.; de Almeida, L. P.; Matos, C. A.; Nóbrega, C. Stress granules, RNA-binding proteins and polyglutamine diseases: too much aggregation? *Cell Death & Disease* **2021,** *12* (6), 592.

9 Klein, I. A.; Boija, A.; Afeyan, L. K.; Hawken, S. W.; Fan, M.; Dall'Agnese, A.; Oksuz, O.; Henninger, J. E.; Shrinivas, K.; Sabari, B. R.; Sagi, I.; Clark, V. E.; Platt, J. M.; Kar, M.; McCall, P. M.; Zamudio, A. V.; Manteiga, J. C.; Coffey, E. L.; Li, C. H.; Hannett, N. M.; Guo, Y. E.; Decker, T. M.; Lee, T. I.; Zhang, T.; Weng, J. K.; Taatjes, D. J.; Chakraborty, A.; Sharp, P. A.; Chang, Y. T.; Hyman, A. A.; Gray, N. S.; Young, R. A. Partitioning of cancer therapeutics in nuclear condensates. *Science* **2020,** *368* (6497), 1386-1392.

10 Kanekura, K.; Kuroda, M. How can we interpret the relationship between liquid-liquid phase separation and amyotrophic lateral sclerosis? *Lab Invest* **2022,** *102* (9), 912-918.

11 Zhang, M.; Mittag, T.; Case, L. The next phase of biomolecular condensate research. *Cell Rep* **2024,** *43* (12), 115076.

12 Schmit, J. D.; Feric, M.; Dundr, M. How Hierarchical Interactions Make Membraneless Organelles Tick Like Clockwork. *Trends Biochem Sci* **2021,** *46* (7), 525-534.

13 Lyon, A. S.; Peeples, W. B.; Rosen, M. K. A framework for understanding the functions of biomolecular condensates across scales. *Nat Rev Mol Cell Biol* **2021,** *22* (3), 215-235.

14 Mitrea, D. M.; Mittasch, M.; Gomes, B. F.; Klein, I. A.; Murcko, M. A. Modulating biomolecular condensates: a novel approach to drug discovery. *Nat Rev Drug Discov* **2022,** *21* (11), 841-862.

15 Li, W.; Jiang, C.; Zhang, E. Advances in the phase separation-organized membraneless organelles in cells: a narrative review. *Transl Cancer Res* **2021,** *10* (11), 4929-4946.

16 Yang, S.; Shen, W.; Hu, J.; Cai, S.; Zhang, C.; Jin, S.; Guan, X.; Wu, J.; Wu, Y.; Cui, J. Molecular mechanisms and cellular functions of liquid-liquid phase separation during antiviral immune responses. *Front Immunol* **2023,** *14*, 1162211.

17 Silva, J. L.; Foguel, D.; Ferreira, V. F.; Vieira, T.; Marques, M. A.; Ferretti, G. D. S.; Outeiro, T. F.; Cordeiro, Y.; de Oliveira, G. A. P. Targeting Biomolecular Condensation and Protein Aggregation against Cancer. *Chem Rev* **2023,** *123* (14), 9094-9138.

18 Bratek-Skicki, A.; Van Nerom, M.; Maes, D.; Tompa, P. Biological colloids: Unique properties of membraneless organelles in the cell. *Adv Colloid Interface Sci* **2022,** *310*, 102777.

19 Brangwynne, C. P.; Eckmann, C. R.; Courson, D. S.; Rybarska, A.; Hoege, C.; Gharakhani, J.; Julicher, F.; Hyman, A. A. Germline P granules are liquid droplets that localize by controlled dissolution/condensation. *Science* **2009,** *324* (5935), 1729-1732.

20 Patel, A.; Lee, H. O.; Jawerth, L.; Maharana, S.; Jahnel, M.; Hein, M. Y.; Stoynov, S.; Mahamid, J.; Saha, S.; Franzmann, T. M.; Pozniakovski, A.; Poser, I.; Maghelli, N.; Royer, L. A.; Weigert, M.; Myers, E. W.; Grill, S.; Drechsel, D.; Hyman, A. A.; Alberti, S. A Liquid-to-Solid Phase Transition of the ALS Protein FUS Accelerated by Disease Mutation. *Cell* **2015,** *162* (5), 1066-1077.

21 Hyman, A. A.; Weber, C. A.; Julicher, F. Liquid-liquid phase separation in biology. *Annu Rev Cell Dev Biol* **2014,** *30* (1), 39-58.

22 Hyman, A. A.; Simons, K. Cell biology. Beyond oil and water--phase transitions in cells. *Science* **2012,** *337* (6098), 1047-1049.

23 Wei, M. T.; Elbaum-Garfinkle, S.; Holehouse, A. S.; Chen, C. C.; Feric, M.; Arnold, C. B.; Priestley, R. D.; Pappu, R. V.; Brangwynne, C. P. Phase behaviour of disordered proteins underlying low density and high permeability of liquid organelles. *Nat Chem* **2017,** *9* (11), 1118-1125.

24 Ranganathan, S.; Shakhnovich, E. I. Dynamic metastable long-living droplets formed by sticker-spacer proteins. *Elife* **2020,** *9*, e56159.

25 Li, P.; Banjade, S.; Cheng, H. C.; Kim, S.; Chen, B.; Guo, L.; Llaguno, M.; Hollingsworth, J. V.; King, D. S.; Banani, S. F.; Russo, P. S.; Jiang, Q. X.; Nixon, B. T.; Rosen, M. K. Phase transitions in the assembly of multivalent signalling proteins. *Nature* **2012,** *483* (7389), 336-340.

26 Dignon, G. L.; Best, R. B.; Mittal, J. Biomolecular Phase Separation: From Molecular Driving Forces to Macroscopic Properties. *Annu Rev Phys Chem* **2020,** *71* (1), 53-75.

27 Rangachari, V. Biomolecular condensates - extant relics or evolving microcompartments? *Commun Biol* **2023,** *6* (1), 656.

28 Kossel, A. Ueber die basischen Stoffe des Zellkerns. **1897**.

29 Wilson, E. B. The Structure of Protoplasm. *Science* **1899,** *10* (237), 33-45.

30 Hyman, A. A.; Brangwynne, C. P. Beyond stereospecificity: liquids and mesoscale organization of cytoplasm. *Dev Cell* **2011,** *21* (1), 14-16.

31 Abbas, M.; Lipinski, W. P.; Wang, J.; Spruijt, E. Peptide-based coacervates as biomimetic protocells. *Chem Soc Rev* **2021,** *50* (6), 3690-3705.

32 Fang, Y.; Li, L.; Inoue, C.; Lundin, L.; Appelqvist, I. Associative and segregative phase separations of gelatin/kappa-carrageenan aqueous mixtures. *Langmuir* **2006,** *22* (23), 9532-9537.

33 Buzza, D. M.; Fletcher, P. D.; Georgiou, T. K.; Ghasdian, N. Water-in-water emulsions based on incompatible polymers and stabilized by triblock copolymers-templated polymersomes. *Langmuir* **2013,** *29* (48), 14804-14814.

34 Flory, P. J. Molecular size distribution in three dimensional polymers. I. Gelation1. *Journal of the american chemical society* **1941,** *63* (11), 3083-3090.

35 Flory, P. J. Thermodynamics of high polymer solutions. *Journal of Chemical Physics* **1942,** *10* (1), 51-61.

36 Choi, J. M.; Holehouse, A. S.; Pappu, R. V. Physical Principles Underlying the Complex Biology of Intracellular Phase Transitions. *Annu Rev Biophys* **2020,** *49* (Volume 49, 2020), 107-133.

37 Sommer, J. U. Gluonic and Regulatory Solvents: A Paradigm for Tunable Phase Segregation in Polymers. *Macromolecules* **2018,** *51* (8), 3066-3074.

38 Lin, Z.; Beneyton, T.; Baret, J. C.; Martin, N. Coacervate Droplets for Synthetic Cells. *Small Methods* **2023,** *7* (12), e2300496.

39 Naz, M.; Zhang, L.; Chen, C.; Yang, S.; Dou, H.; Mann, S.; Li, J. Self-assembly of stabilized droplets from liquid-liquid phase separation for higher-order structures and functions. *Commun Chem* **2024,** *7* (1), 79.

40 Rubinstein, M.; Dobrynin, A. V. Solutions of associative polymers. *Trends in Polymer Science* **1997,** *5* (6), 181-186.

41 Pak, C. W.; Kosno, M.; Holehouse, A. S.; Padrick, S. B.; Mittal, A.; Ali, R.; Yunus, A. A.; Liu, D. R.; Pappu, R. V.; Rosen, M. K. Sequence Determinants of Intracellular Phase Separation by Complex Coacervation of a Disordered Protein. *Mol Cell* **2016,** *63* (1), 72-85.

42 Borcherds, W.; Bremer, A.; Borgia, M. B.; Mittag, T. How do intrinsically disordered protein regions encode a driving force for liquid-liquid phase separation? *Curr Opin Struct Biol* **2021,** *67*, 41-50.

43 Hughes, M. P.; Sawaya, M. R.; Boyer, D. R.; Goldschmidt, L.; Rodriguez, J. A.; Cascio, D.; Chong, L.; Gonen, T.; Eisenberg, D. S. Atomic structures of low-complexity protein segments reveal kinked beta sheets that assemble networks. *Science* **2018,** *359* (6376), 698-701.

44 Martin, E. W.; Holehouse, A. S.; Peran, I.; Farag, M.; Incicco, J. J.; Bremer, A.; Grace, C. R.; Soranno, A.; Pappu, R. V.; Mittag, T. Valence and patterning of aromatic residues determine the phase behavior of prion-like domains. *Science* **2020,** *367* (6478), 694-699.

45 Bremer, A.; Farag, M.; Borcherds, W. M.; Peran, I.; Martin, E. W.; Pappu, R. V.; Mittag, T. Deciphering how naturally occurring sequence features impact the phase behaviours of disordered prion-like domains. *Nat Chem* **2022,** *14* (2), 196-207.

46 Guseva, S.; Schnapka, V.; Adamski, W.; Maurin, D.; Ruigrok, R. W. H.; Salvi, N.; Blackledge, M. Liquid-Liquid Phase Separation Modifies the Dynamic Properties of Intrinsically Disordered Proteins. *J Am Chem Soc* **2023,** *145* (19), 10548-10563.

47 Kato, M.; Han, T. W.; Xie, S.; Shi, K.; Du, X.; Wu, L. C.; Mirzaei, H.; Goldsmith, E. J.; Longgood, J.; Pei, J.; Grishin, N. V.; Frantz, D. E.; Schneider, J. W.; Chen, S.; Li, L.; Sawaya, M. R.; Eisenberg, D.; Tycko, R.; McKnight, S. L. Cell-free formation of RNA granules: low complexity sequence domains form dynamic fibers within hydrogels. *Cell* **2012,** *149* (4), 753-767.

48 Davis, R. B.; Supakar, A.; Ranganath, A. K.; Moosa, M. M.; Banerjee, P. R. Heterotypic interactions can drive selective co-condensation of prion-like low-complexity domains of FET proteins and mammalian SWI/SNF complex. *Nat Commun* **2024,** *15* (1), 1168.

49 Choi, J. M.; Pappu, R. V. The Stickers and Spacers Framework for Describing Phase Behavior of Multivalent Intrinsically Disordered Proteins. *Biophysical Journal* **2020,** *118* (3), 492a-492a.

50 Banani, S. F.; Rice, A. M.; Peeples, W. B.; Lin, Y.; Jain, S.; Parker, R.; Rosen, M. K. Compositional Control of Phase-Separated Cellular Bodies. *Cell* **2016,** *166* (3), 651-663.

51 Kamagata, K.; Iwaki, N.; Kanbayashi, S.; Banerjee, T.; Chiba, R.; Gaudon, V.; Castaing, B.; Sakomoto, S. Structure-dependent recruitment and diffusion of guest proteins in liquid droplets of FUS. *Sci Rep* **2022,** *12* (1), 7101.

52 Lin, Y.; Protter, D. S.; Rosen, M. K.; Parker, R. Formation and Maturation of Phase-Separated Liquid Droplets by RNA-Binding Proteins. *Mol Cell* **2015,** *60* (2), 208-219.

53 Molliex, A.; Temirov, J.; Lee, J.; Coughlin, M.; Kanagaraj, A. P.; Kim, H. J.; Mittag, T.; Taylor, J. P. Phase separation by low complexity domains promotes stress granule assembly and drives pathological fibrillization. *Cell* **2015,** *163* (1), 123-133.

54 Gabryelczyk, B.; Cai, H.; Shi, X.; Sun, Y.; Swinkels, P. J. M.; Salentinig, S.; Pervushin, K.; Miserez, A. Hydrogen bond guidance and aromatic stacking drive liquid-liquid phase separation of intrinsically disordered histidine-rich peptides. *Nat Commun* **2019,** *10* (1), 5465.

55 Kim, S.; Yoo, H. Y.; Huang, J.; Lee, Y.; Park, S.; Park, Y.; Jin, S.; Jung, Y. M.; Zeng, H.; Hwang, D. S.; Jho, Y. Salt Triggers the Simple Coacervation of an Underwater Adhesive When Cations Meet Aromatic pi Electrons in Seawater. *ACS Nano* **2017,** *11* (7), 6764-6772.

56 Welsh, T. J.; Krainer, G.; Espinosa, J. R.; Joseph, J. A.; Sridhar, A.; Jahnel, M.; Arter, W. E.; Saar, K. L.; Alberti, S.; Collepardo-Guevara, R.; Knowles, T. P. J. Surface Electrostatics Govern the Emulsion Stability of Biomolecular Condensates. *Nano Lett* **2022,** *22* (2), 612-621.

57 Li, Q.; Song, Q.; Guo, W.; Cao, Y.; Cui, X.; Chen, D.; Shum, H. C. Synthetic Membraneless Droplets for Synaptic-Like Clustering of Lipid Vesicles. *Angew Chem Int Ed Engl* **2023,** *62* (45), e202313096.

58 Li, J. B.; Xu, Z. J.; Zhu, M.; Zhao, C. Y.; Wang, X. L.; Chen, H. X.; Liu, X. M.; Wang, L.; Huang, X. Programmable spatial organization of liquid-phase condensations. *Chem* **2022,** *8* (3), 784-800.

59 Andre, A. A. M.; Spruijt, E. Liquid-Liquid Phase Separation in Crowded Environments. *Int J Mol Sci* **2020,** *21* (16).

60 Minton, A. P. Excluded volume as a determinant of macromolecular structure and reactivity. *Biopolymers* **2004,** *20* (10), 2093-2120.

61 Ghosh, A.; Mazarakos, K.; Zhou, H. X. Three archetypical classes of macromolecular regulators of protein liquid-liquid phase separation. *Proc Natl Acad Sci U S A* **2019,** *116* (39), 19474-19483.

62 Schuster, B. S.; Reed, E. H.; Parthasarathy, R.; Jahnke, C. N.; Caldwell, R. M.; Bermudez, J. G.; Ramage, H.; Good, M. C.; Hammer, D. A. Controllable protein phase separation and modular recruitment to form responsive membraneless organelles. *Nat Commun* **2018,** *9* (1), 2985.

63 Qian, D. Y.; Welsh, T. J.; Erkamp, N. A.; Qamar, S.; Nixon-Abell, J.; Krainer, G.; St George-Hyslop, P.; Michaels, T. C. T.; Knowles, T. P. J. Tie-Line Analysis Reveals Interactions Driving Heteromolecular Condensate Formation. *Physical Review X* **2022,** *12* (4), 041038.

64 Marianelli, A. M.; Miller, B. M.; Keating, C. D. Impact of macromolecular crowding on RNA/spermine complex coacervation and oligonucleotide compartmentalization. *Soft Matter* **2018,** *14* (3), 368-378.

65 Li, J.; Zhang, M.; Ma, W.; Yang, B.; Lu, H.; Zhou, F.; Zhang, L. Post-translational modifications in liquid-liquid phase separation: a comprehensive review. *Mol Biomed* **2022,** *3* (1), 13.

66 Sipko, E. L.; Chappell, G. F.; Berlow, R. B. Multivalency emerges as a common feature of intrinsically disordered protein interactions. *Curr Opin Struct Biol* **2024,** *84*, 102742.

67 Stockmayer, W. H. Theory of Molecular Size Distribution and Gel Formation in Branched-Chain Polymers. *The Journal of Chemical Physics* **1943,** *11* (2), 45-55.

68 Lin, Y.; Fichou, Y.; Longhini, A. P.; Llanes, L. C.; Yin, P.; Bazan, G. C.; Kosik, K. S.; Han, S. Liquid-Liquid Phase Separation of Tau Driven by Hydrophobic Interaction Facilitates Fibrillization of Tau. *J Mol Biol* **2021,** *433* (2), 166731.

69 Pei, X.; Chen, Y.; Liu, L.; Meng, L.; Zhang, J.; Liu, Y.; Chen, L. E242-E261 region of MYC regulates liquid-liquid phase separation and tumor growth by providing negative charges. *J Biol Chem* **2024,** *300* (11), 107836.

70 Astoricchio, E.; Alfano, C.; Rajendran, L.; Temussi, P. A.; Pastore, A. The Wide World of Coacervates: From the Sea to Neurodegeneration. *Trends Biochem Sci* **2020,** *45* (8), 706-717.

71 Gallivan, J. P.; Dougherty, D. A. Cation-pi interactions in structural biology. *Proc Natl Acad Sci U S A* **1999,** *96* (17), 9459-9464.

72 Morozova, N.; Allers, J.; Myers, J.; Shamoo, Y. Protein-RNA interactions: exploring binding patterns with a three-dimensional superposition analysis of high resolution structures. *Bioinformatics* **2006,** *22* (22), 2746-2752.

73 Cubero, E.; Luque, F. J.; Orozco, M. Is polarization important in cation-π interactions? *Proceedings of the National Academy of Sciences* **1998,** *95* (11), 5976-5980.

74 Vernon, R. M.; Chong, P. A.; Tsang, B.; Kim, T. H.; Bah, A.; Farber, P.; Lin, H.; Forman-Kay, J. D. Pi-Pi contacts are an overlooked protein feature relevant to phase separation. *Elife* **2018,** *7*, e31486.

75 Song, S.; Ivanov, T.; Yuan, D.; Wang, J.; da Silva, L. C.; Xie, J.; Cao, S. Peptide-Based Biomimetic Condensates via Liquid-Liquid Phase Separation as Biomedical Delivery Vehicles. *Biomacromolecules* **2024,** *25* (9), 5468-5488.

76 Chew, P. Y.; Joseph, J. A.; Collepardo-Guevara, R.; Reinhardt, A. Aromatic and arginine content drives multiphasic condensation of protein-RNA mixtures. *Biophys J* **2024,** *123* (11), 1342-1355.

77 Kim, G.; Lee, S. E.; Jeong, S.; Lee, J.; Park, D.; Chang, S. Multivalent electrostatic pi-cation interaction between synaptophysin and synapsin is responsible for the coacervation. *Mol Brain* **2021,** *14* (1), 137.

78 Das, S.; Lin, Y. H.; Vernon, R. M.; Forman-Kay, J. D.; Chan, H. S. Comparative roles of charge, pi, and hydrophobic interactions in sequence-dependent phase separation of intrinsically disordered proteins. *Proc Natl Acad Sci U S A* **2020,** *117* (46), 28795-28805.

79 Das, S.; Amin, A. N.; Lin, Y.-H.; Chan, H. S. Coarse-grained residue-based models of disordered protein condensates: utility and limitations of simple charge pattern parameters. *Physical Chemistry Chemical Physics* **2018,** *20* (45), 28558-28574.

80 Chen, C.; Yamanaka, Y.; Ueda, K.; Li, P.; Miyagi, T.; Harada, Y.; Tezuka, S.; Narumi, S.; Sugimoto, M.; Kuroda, M.; Hayamizu, Y.; Kanekura, K. Phase separation and toxicity of C9orf72 poly(PR) depends on alternate distribution of arginine. *J Cell Biol* **2021,** *220* (11).

81 Duster, R.; Kaltheuner, I. H.; Schmitz, M.; Geyer, M. 1,6-Hexanediol, commonly used to dissolve liquid-liquid phase separated condensates, directly impairs kinase and phosphatase activities. *J Biol Chem* **2021,** *296*, 100260.

82 Muzzopappa, F.; Hummert, J.; Anfossi, M.; Tashev, S. A.; Herten, D. P.; Erdel, F. Detecting and quantifying liquid-liquid phase separation in living cells by model-free calibrated half-bleaching. *Nat Commun* **2022,** *13* (1), 7787.

83 Gomes, E.; Shorter, J. The molecular language of membraneless organelles. *J Biol Chem* **2019,** *294* (18), 7115-7127.

84 Spoelstra, W. K.; Jacques, J. M.; Gonzalez-Linares, R.; Nobrega, F. L.; Haagsma, A. C.; Dogterom, M.; Meijer, D. H.; Idema, T.; Brouns, S. J. J.; Reese, L. CRISPR-based DNA and RNA detection with liquid-liquid phase separation. *Biophys J* **2021,** *120* (7), 1198-1209.

85 Aumiller Jr, W. M.; Pir Cakmak, F.; Davis, B. W.; Keating, C. D. RNA-based coacervates as a model for membraneless organelles: formation, properties, and interfacial liposome assembly. *Langmuir* **2016,** *32* (39), 10042-10053.

86 Xue, S.; Gong, R.; He, F.; Li, Y.; Wang, Y.; Tan, T.; Luo, S. Z. Low-complexity domain of U1-70K modulates phase separation and aggregation through distinctive basic-acidic motifs. *Sci Adv* **2019,** *5* (11), eaax5349.

87 Babinchak, W. M.; Haider, R.; Dumm, B. K.; Sarkar, P.; Surewicz, K.; Choi, J. K.; Surewicz, W. K. The role of liquid-liquid phase separation in aggregation of the TDP-43 low-complexity domain. *J Biol Chem* **2019,** *294* (16), 6306-6317.

88 Alberti, S.; Saha, S.; Woodruff, J. B.; Franzmann, T. M.; Wang, J.; Hyman, A. A. A User's Guide for Phase Separation Assays with Purified Proteins. *J Mol Biol* **2018,** *430* (23), 4806-4820.

89 Boeynaems, S.; Chong, S.; Gsponer, J.; Holt, L.; Milovanovic, D.; Mitrea, D. M.; Mueller-Cajar, O.; Portz, B.; Reilly, J. F.; Reinkemeier, C. D.; Sabari, B. R.; Sanulli, S.; Shorter, J.; Sontag, E.; Strader, L.; Stachowiak, J.; Weber, S. C.; White, M.; Zhang, H.; Zweckstetter, M.; Elbaum-Garfinkle, S.; Kriwacki, R. Phase Separation in Biology and Disease; Current Perspectives and Open Questions. *J Mol Biol* **2023,** *435* (5), 167971.

90 Ramaswami, M.; Taylor, J. P.; Parker, R. Altered ribostasis: RNA-protein granules in degenerative disorders. *Cell* **2013,** *154* (4), 727-736.

91 Wang, B.; Zhang, L.; Dai, T.; Qin, Z.; Lu, H.; Zhang, L.; Zhou, F. Liquid-liquid phase separation in human health and diseases. *Signal Transduct Target Ther* **2021,** *6* (1), 290.

92 Babinchak, W. M.; Surewicz, W. K. Liquid-Liquid Phase Separation and Its Mechanistic Role in Pathological Protein Aggregation. *J Mol Biol* **2020,** *432* (7), 1910-1925.

93 McCluggage, F.; Fox, A. H. Paraspeckle nuclear condensates: Global sensors of cell stress? *Bioessays* **2021,** *43* (5), e2000245.

94 Scotter, E. L.; Vance, C.; Nishimura, A. L.; Lee, Y. B.; Chen, H. J.; Urwin, H.; Sardone, V.; Mitchell, J. C.; Rogelj, B.; Rubinsztein, D. C.; Shaw, C. E. Differential roles of the ubiquitin proteasome system and autophagy in the clearance of soluble and aggregated TDP-43 species. *J Cell Sci* **2014,** *127* (Pt 6), 1263-1278.

95 Ding, W. X.; Yin, X. M. Sorting, recognition and activation of the misfolded protein degradation pathways through macroautophagy and the proteasome. *Autophagy* **2008,** *4* (2), 141-150.

96 Wang, Z.; Zhang, H. Phase Separation, Transition, and Autophagic Degradation of Proteins in Development and Pathogenesis. *Trends in Cell Biology* **2019,** *29* (5), 417-427.

97 Lallemand-Breitenbach, V.; de Thé, H. PML nuclear bodies. *Cold Spring Harb Perspect Biol* **2010,** *2* (5), a000661.

98 Orti, F.; Navarro, A. M.; Rabinovich, A.; Wodak, S. J.; Marino-Buslje, C. Insight into membraneless organelles and their associated proteins: Drivers, Clients and Regulators. *Comput Struct Biotechnol J* **2021,** *19*, 3964-3977.

99 Mead, R. J.; Shan, N.; Reiser, H. J.; Marshall, F.; Shaw, P. J. Amyotrophic lateral sclerosis: a neurodegenerative disorder poised for successful therapeutic translation. *Nat Rev Drug Discov* **2023,** *22* (3), 185-212.

100 Carey, J. L.; Guo, L. Liquid-Liquid Phase Separation of TDP-43 and FUS in Physiology and Pathology of Neurodegenerative Diseases. *Front Mol Biosci* **2022,** *9*, 826719.

101 Neumann, M.; Sampathu, D. M.; Kwong, L. K.; Truax, A. C.; Micsenyi, M. C.; Chou, T. T.; Bruce, J.; Schuck, T.; Grossman, M.; Clark, C. M.; McCluskey, L. F.; Miller, B. L.; Masliah, E.; Mackenzie, I. R.; Feldman, H.; Feiden, W.; Kretzschmar, H. A.; Trojanowski, J. Q.; Lee, V. M. Ubiquitinated TDP-43 in frontotemporal lobar degeneration and amyotrophic lateral sclerosis. *Science* **2006,** *314* (5796), 130-133.

102 Mann, D. M.; Rollinson, S.; Robinson, A.; Bennion Callister, J.; Thompson, J. C.; Snowden, J. S.; Gendron, T.; Petrucelli, L.; Masuda-Suzukake, M.; Hasegawa, M.; Davidson, Y.; Pickering-Brown, S. Dipeptide repeat proteins are present in the p62 positive inclusions in patients with frontotemporal lobar degeneration and motor neurone disease associated with expansions in C9ORF72. *Acta Neuropathol Commun* **2013,** *1*, 68.

103 Baborie, A.; Griffiths, T. D.; Jaros, E.; Perry, R.; McKeith, I. G.; Burn, D. J.; Masuda-Suzukake, M.; Hasegawa, M.; Rollinson, S.; Pickering-Brown, S.; Robinson, A. C.; Davidson, Y. S.; Mann, D. M. Accumulation of dipeptide repeat proteins predates that of TDP-43 in frontotemporal lobar degeneration associated with hexanucleotide repeat expansions in C9ORF72 gene. *Neuropathol Appl Neurobiol* **2015,** *41* (5), 601-612.

104 Sakae, N.; Bieniek, K. F.; Zhang, Y. J.; Ross, K.; Gendron, T. F.; Murray, M. E.; Rademakers, R.; Petrucelli, L.; Dickson, D. W. Poly-GR dipeptide repeat polymers correlate with neurodegeneration and Clinicopathological subtypes in C9ORF72-related brain disease. *Acta Neuropathol Commun* **2018,** *6* (1), 63.

105 Schludi, M. H.; May, S.; Grasser, F. A.; Rentzsch, K.; Kremmer, E.; Kupper, C.; Klopstock, T.; German Consortium for Frontotemporal Lobar, D.; Bavarian Brain Banking, A.; Arzberger, T.; Edbauer, D. Distribution of dipeptide repeat proteins in cellular models and C9orf72 mutation cases suggests link to transcriptional silencing. *Acta Neuropathol* **2015,** *130* (4), 537-555.

106Alberti, S.; Dormann, D. Liquid-Liquid Phase Separation in Disease. *Annu Rev Genet* **2019,** *53* (1), 171-194.

107 Liu, Y.; Momani, B.; Winter, H. H.; Perry, S. L. Rheological characterization of liquid-to-solid transitions in bulk polyelectrolyte complexes. *Soft Matter* **2017,** *13* (40), 7332-7340.

108 Dogra, P.; Joshi, A.; Majumdar, A.; Mukhopadhyay, S. Intermolecular Charge-Transfer Modulates Liquid–Liquid Phase Separation and Liquid-to-Solid Maturation of an Intrinsically Disordered pH-Responsive Domain. *Journal of the American Chemical Society* **2019,** *141* (51), 20380-20389.

109 Conicella, A. E.; Zerze, G. H.; Mittal, J.; Fawzi, N. L. ALS Mutations Disrupt Phase Separation Mediated by alpha-Helical Structure in the TDP-43 Low-Complexity C-Terminal Domain. *Structure* **2016,** *24* (9), 1537-1549.

110 Kanekura, K.; Miyagi, T. Intricate roles of spacers and stickers of Arg-rich C9ORF72 dipeptide repeat proteins; from toxicity to targeting to membraneless organelles. *Organelle* **2023,** *1* (1).

111 Nanaura, H.; Kawamukai, H.; Fujiwara, A.; Uehara, T.; Aiba, Y.; Nakanishi, M.; Shiota, T.; Hibino, M.; Wiriyasermkul, P.; Kikuchi, S.; Nagata, R.; Matsubayashi, M.; Shinkai, Y.; Niwa, T.; Mannen, T.; Morikawa, N.; Iguchi, N.; Kiriyama, T.; Morishima, K.; Inoue, R.; Sugiyama, M.; Oda, T.; Kodera, N.; Toma-Fukai, S.; Sato, M.; Taguchi, H.; Nagamori, S.; Shoji, O.; Ishimori, K.; Matsumura, H.; Sugie, K.; Saio, T.; Yoshizawa, T.; Mori, E. C9orf72-derived arginine-rich poly-dipeptides impede phase modifiers. *Nat Commun* **2021,** *12* (1), 5301.

112 Solomon, D. A.; Smikle, R.; Reid, M. J.; Mizielinska, S. Altered Phase Separation and Cellular Impact in C9orf72-Linked ALS/FTD. *Front Cell Neurosci* **2021,** *15*, 664151.

113 Yewdall, N. A.; André, A. A. M.; Lu, T. M.; Spruijt, E. Coacervates as models of membraneless organelles. *Current Opinion in Colloid & Interface Science* **2021,** *52*, 101416.

114 Shi, Y.; Lin, S.; Staats, K. A.; Li, Y.; Chang, W. H.; Hung, S. T.; Hendricks, E.; Linares, G.

R.; Wang, Y.; Son, E. Y.; Wen, X.; Kisler, K.; Wilkinson, B.; Menendez, L.; Sugawara, T.; Woolwine, P.; Huang, M.; Cowan, M. J.; Ge, B.; Koutsodendris, N.; Sandor, K. P.; Komberg, J.; Vangoor, V. R.; Senthilkumar, K.; Hennes, V.; Seah, C.; Nelson, A. R.; Cheng, T. Y.; Lee, S. J.; August, P. R.; Chen, J. A.; Wisniewski, N.; Hanson-Smith, V.; Belgard, T. G.; Zhang, A.; Coba, M.; Grunseich, C.; Ward, M. E.; van den Berg, L. H.; Pasterkamp, R. J.; Trotti, D.; Zlokovic, B. V.; Ichida, J. K. Haploinsufficiency leads to neurodegeneration in C9ORF72 ALS/FTD human induced motor neurons. *Nat Med* **2018,** *24* (3), 313-325.

115 Donnelly, C. J.; Zhang, P. W.; Pham, J. T.; Haeusler, A. R.; Mistry, N. A.; Vidensky, S.; Daley, E. L.; Poth, E. M.; Hoover, B.; Fines, D. M.; Maragakis, N.; Tienari, P. J.; Petrucelli, L.; Traynor, B. J.; Wang, J.; Rigo, F.; Bennett, C. F.; Blackshaw, S.; Sattler, R.; Rothstein, J. D. RNA toxicity from the ALS/FTD C9ORF72 expansion is mitigated by antisense intervention. *Neuron* **2013,** *80* (2), 415-428.

116 Mizielinska, S.; Gronke, S.; Niccoli, T.; Ridler, C. E.; Clayton, E. L.; Devoy, A.; Moens, T.; Norona, F. E.; Woollacott, I. O. C.; Pietrzyk, J.; Cleverley, K.; Nicoll, A. J.; Pickering-Brown, S.; Dols, J.; Cabecinha, M.; Hendrich, O.; Fratta, P.; Fisher, E. M. C.; Partridge, L.; Isaacs, A. M. C9orf72 repeat expansions cause neurodegeneration in Drosophila through arginine-rich proteins. *Science* **2014,** *345* (6201), 1192-1194.

117 Kwon, I.; Xiang, S.; Kato, M.; Wu, L.; Theodoropoulos, P.; Wang, T.; Kim, J.; Yun, J.; Xie, Y.; McKnight, S. L. Poly-dipeptides encoded by the C9orf72 repeats bind nucleoli, impede RNA biogenesis, and kill cells. *Science* **2014,** *345* (6201), 1139-1145.

118 Braems, E.; Swinnen, B.; Van Den Bosch, L. C9orf72 loss-of-function: a trivial, stand-alone or additive mechanism in C9 ALS/FTD? *Acta Neuropathologica* **2020,** *140* (5), 625-643.

119 Hautbergue, G. M.; Cleary, J. D.; Guo, S.; Ranum, L. P. W. Therapeutic strategies for C9orf72 amyotrophic lateral sclerosis and frontotemporal dementia. *Curr Opin Neurol* **2021,** *34* (5), 748-755.

120Balendra, R.; Isaacs, A. M. C9orf72-mediated ALS and FTD: multiple pathways to disease. *Nat Rev Neurol* **2018,** *14* (9), 544-558.

121 Wen, X.; Tan, W.; Westergard, T.; Krishnamurthy, K.; Markandaiah, S. S.; Shi, Y.; Lin, S.; Shneider, N. A.; Monaghan, J.; Pandey, U. B.; Pasinelli, P.; Ichida, J. K.; Trotti, D. Antisense proline-arginine RAN dipeptides linked to C9ORF72-ALS/FTD form toxic nuclear aggregates that initiate in vitro and in vivo neuronal death. *Neuron* **2014,** *84* (6), 1213-1225.

122 Zhang, Y. J.; Gendron, T. F.; Grima, J. C.; Sasaguri, H.; Jansen-West, K.; Xu, Y. F.; Katzman, R. B.; Gass, J.; Murray, M. E.; Shinohara, M.; Lin, W. L.; Garrett, A.; Stankowski, J. N.; Daughrity, L.; Tong, J.; Perkerson, E. A.; Yue, M.; Chew, J.; Castanedes-Casey, M.; Kurti, A.; Wang, Z. S.; Liesinger, A. M.; Baker, J. D.; Jiang, J.; Lagier-Tourenne, C.; Edbauer, D.; Cleveland, D. W.; Rademakers, R.; Boylan, K. B.; Bu, G.; Link, C. D.; Dickey, C. A.; Rothstein, J. D.; Dickson, D. W.; Fryer, J. D.; Petrucelli, L. C9ORF72 poly(GA) aggregates sequester and impair HR23 and nucleocytoplasmic transport proteins. *Nat Neurosci* **2016,** *19* (5), 668-677.

123 Guo, Q.; Lehmer, C.; Martinez-Sanchez, A.; Rudack, T.; Beck, F.; Hartmann, H.; Perez-Berlanga, M.; Frottin, F.; Hipp, M. S.; Hartl, F. U.; Edbauer, D.; Baumeister, W.; Fernandez-Busnadiego, R. In Situ Structure of Neuronal C9orf72 Poly-GA Aggregates Reveals Proteasome Recruitment. *Cell* **2018,** *172* (4), 696-705 e612.

124 Nihei, Y.; Mori, K.; Werner, G.; Arzberger, T.; Zhou, Q.; Khosravi, B.; Japtok, J.; Hermann, A.; Sommacal, A.; Weber, M.; German Consortium for Frontotemporal Lobar, D.; Bavarian Brain Banking, A.; Kamp, F.; Nuscher, B.; Edbauer, D.; Haass, C. Poly-glycine-alanine exacerbates C9orf72 repeat expansion-mediated DNA damage via sequestration of phosphorylated ATM and loss of nuclear hnRNPA3. *Acta Neuropathol* **2020,** *139* (1), 99-118.

125 Jain, S.; Das, D.; Mukherjee, A.; Roy, I. Inhibition of PolyGA Dipeptide Repeat Protein Aggregation by Nucleic Acid Aptamers in C9 Amyotrophic Lateral Sclerosis-Frontotemporal Dementia Models. *Molecular Neurobiology* **2025**, DOI:10.1007/s12035-025-05075-1 10.1007/s12035-025-05075-1.

126 Kanekura, K.; Yagi, T.; Cammack, A. J.; Mahadevan, J.; Kuroda, M.; Harms, M. B.; Miller, T. M.; Urano, F. Poly-dipeptides encoded by the C9ORF72 repeats block global protein translation. *Hum Mol Genet* **2016,** *25* (9), 1803-1813.

127 Kanekura, K.; Harada, Y.; Fujimoto, M.; Yagi, T.; Hayamizu, Y.; Nagaoka, K.; Kuroda, M. Characterization of membrane penetration and cytotoxicity of C9orf72-encoding arginine-rich dipeptides. *Sci Rep* **2018,** *8* (1), 12740.

128 Masrori, P.; Beckers, J.; Gossye, H.; Van Damme, P. The role of inflammation in neurodegeneration: novel insights into the role of the immune system in C9orf72 HRE-mediated ALS/FTD. *Mol Neurodegener* **2022,** *17* (1), 22.

129 Moens, T. G.; Partridge, L.; Isaacs, A. M. Genetic models of C9orf72: what is toxic? *Curr Opin Genet Dev* **2017,** *44*, 92-101.

130 Lopez-Gonzalez, R.; Lu, Y.; Gendron, T. F.; Karydas, A.; Tran, H.; Yang, D.; Petrucelli, L.; Miller, B. L.; Almeida, S.; Gao, F. B. Poly(GR) in C9ORF72-Related ALS/FTD Compromises Mitochondrial Function and Increases Oxidative Stress and DNA Damage in iPSC-Derived Motor Neurons. *Neuron* **2016,** *92* (2), 383-391.

131 Li, S.; Wu, Z.; Li, Y.; Tantray, I.; De Stefani, D.; Mattarei, A.; Krishnan, G.; Gao, F. B.; Vogel, H.; Lu, B. Altered MICOS Morphology and Mitochondrial Ion Homeostasis Contribute to Poly(GR) Toxicity Associated with C9-ALS/FTD. *Cell Rep* **2020,** *32* (5), 107989.

132 Hutten, S.; Usluer, S.; Bourgeois, B.; Simonetti, F.; Odeh, H. M.; Fare, C. M.; Czuppa, M.; Hruska-Plochan, M.; Hofweber, M.; Polymenidou, M.; Shorter, J.; Edbauer, D.; Madl, T.; Dormann, D. Nuclear Import Receptors Directly Bind to Arginine-Rich Dipeptide Repeat Proteins and Suppress Their Pathological Interactions. *Cell Rep* **2020,** *33* (12), 108538.

133 Cook, C. N.; Wu, Y.; Odeh, H. M.; Gendron, T. F.; Jansen-West, K.; Del Rosso, G.; Yue, M.; Jiang, P.; Gomes, E.; Tong, J.; Daughrity, L. M.; Avendano, N. M.; Castanedes-Casey, M.; Shao, W.; Oskarsson, B.; Tomassy, G. S.; McCampbell, A.; Rigo, F.; Dickson, D. W.; Shorter, J.; Zhang, Y. J.; Petrucelli, L. C9orf72 poly(GR) aggregation induces TDP-43 proteinopathy. *Sci Transl Med* **2020,** *12* (559), eabb3774.

134 Miyagi, T.; Ueda, K.; Sugimoto, M.; Yagi, T.; Ito, D.; Yamazaki, R.; Narumi, S.; Hayamizu, Y.; Uji, I. H.; Kuroda, M.; Kanekura, K. Differential toxicity and localization of arginine-rich C9ORF72 dipeptide repeat proteins depend on de-clustering of positive charges. *iScience* **2023,** *26* (6), 106957.

135 Jafarinia, H.; van der Giessen, E.; Onck, P. R. Phase Separation of Toxic Dipeptide Repeat Proteins Related to C9orf72 ALS/FTD. *Biophys J* **2020,** *119* (4), 843-851.

136 Bratek-Skicki, A.; Ahmed, J.; Jonckheere, K.; Peeters, E.; Heeren, K.; Volkov, A.; Hendrix, J.; Batys, P.; Bosch, L. V. D.; Tompa, P. Application of polystyrene sulfonate (PSS) for inhibiting toxicity of ALS/FTD-linked dipeptide repeats. *bioRxiv* **2023**, DOI:10.1101/2023.05.19.541518 10.1101/2023.05.19.541518, 2023.2005.2019.541518.

137 Dong, D.; Zhang, Z.; Li, Y.; Latallo, M. J.; Wang, S.; Nelson, B.; Wu, R.; Krishnan, G.; Gao, F. B.; Wu, B.; Sun, S. Poly-GR repeats associated with ALS/FTD gene C9ORF72 impair translation elongation and induce a ribotoxic stress response in neurons. *Sci Signal* **2024,** *17* (848), eadl1030.

138 Choi, S. Y.; Lopez-Gonzalez, R.; Krishnan, G.; Phillips, H. L.; Li, A. N.; Seeley, W. W.;

Yao, W. D.; Almeida, S.; Gao, F. B. C9ORF72-ALS/FTD-associated poly(GR) binds Atp5a1 and compromises mitochondrial function in vivo. *Nat Neurosci* **2019,** *22* (6), 851-862.

139 Gittings, L. M.; Boeynaems, S.; Lightwood, D.; Clargo, A.; Topia, S.; Nakayama, L.; Troakes, C.; Mann, D. M. A.; Gitler, A. D.; Lashley, T.; Isaacs, A. M. Symmetric dimethylation of poly-GR correlates with disease duration in C9orf72 FTLD and ALS and reduces poly-GR phase separation and toxicity. *Acta Neuropathol* **2020,** *139* (2), 407-410.

140 Babu, M.; Favretto, F.; de Opakua, A. I.; Rankovic, M.; Becker, S.; Zweckstetter, M. Proline/arginine dipeptide repeat polymers derail protein folding in amyotrophic lateral sclerosis. *Nat Commun* **2021,** *12* (1), 3396.

141 Nguyen, H. P.; Van Broeckhoven, C.; van der Zee, J. ALS Genes in the Genomic Era and their Implications for FTD. *Trends Genet* **2018,** *34* (6), 404-423.

142 Lee, K. H.; Zhang, P.; Kim, H. J.; Mitrea, D. M.; Sarkar, M.; Freibaum, B. D.; Cika, J.; Coughlin, M.; Messing, J.; Molliex, A.; Maxwell, B. A.; Kim, N. C.; Temirov, J.; Moore, J.; Kolaitis, R. M.; Shaw, T. I.; Bai, B.; Peng, J.; Kriwacki, R. W.; Taylor, J. P. C9orf72 Dipeptide Repeats Impair the Assembly, Dynamics, and Function of Membrane-Less Organelles. *Cell* **2016,** *167* (3), 774-788 e717.

143 Boeynaems, S.; Bogaert, E.; Kovacs, D.; Konijnenberg, A.; Timmerman, E.; Volkov, A.; Guharoy, M.; De Decker, M.; Jaspers, T.; Ryan, V. H.; Janke, A. M.; Baatsen, P.; Vercruysse, T.; Kolaitis, R. M.; Daelemans, D.; Taylor, J. P.; Kedersha, N.; Anderson, P.; Impens, F.; Sobott, F.; Schymkowitz, J.; Rousseau, F.; Fawzi, N. L.; Robberecht, W.; Van Damme, P.; Tompa, P.; Van Den Bosch, L. Phase Separation of C9orf72 Dipeptide Repeats Perturbs Stress Granule Dynamics. *Mol Cell* **2017,** *65* (6), 1044-1055 e1045.

144 Maor-Nof, M.; Shipony, Z.; Lopez-Gonzalez, R.; Nakayama, L.; Zhang, Y. J.; Couthouis, J.; Blum, J. A.; Castruita, P. A.; Linares, G. R.; Ruan, K.; Ramaswami, G.; Simon, D. J.; Nof, A.; Santana, M.; Han, K.; Sinnott-Armstrong, N.; Bassik, M. C.; Geschwind, D. H.; Tessier-Lavigne, M.; Attardi, L. D.; Lloyd, T. E.; Ichida, J. K.; Gao, F. B.; Greenleaf, W. J.; Yokoyama, J. S.; Petrucelli, L.; Gitler, A. D. p53 is a central regulator driving neurodegeneration caused by C9orf72 poly(PR). *Cell* **2021,** *184* (3), 689-708 e620.

145 Cicardi, M. E.; Hallgren, J. H.; Mawrie, D.; Krishnamurthy, K.; Markandaiah, S. S.; Nelson, A. T.; Kankate, V.; Anderson, E. N.; Pasinelli, P.; Pandey, U. B.; Eischen, C. M.; Trotti, D. C9orf72 poly(PR) mediated neurodegeneration is associated with nucleolar stress. *iScience* **2023,** *26* (9), 107505.

146 Zumbro, E.; Alexander-Katz, A. Polymer Stiffness Regulates Multivalent Binding and Liquid-Liquid Phase Separation. *Biophys J* **2020,** *119* (9), 1849-1864.

147 Lytle, T. K.; Sing, C. E. Tuning chain interaction entropy in complex coacervation using polymer stiffness, architecture, and salt valency. *Molecular Systems Design & Engineering* **2018,** *3* (1), 183-196.

148 Kanekura, K.; Hayamizu, Y.; Kuroda, M. Order controls disordered droplets: structure-function relationships in C9ORF72-derived poly(PR). *Am J Physiol Cell Physiol* **2022,** *322* (2), C197-C204.

149 Suzuki, H.; Matsuoka, M. Proline-arginine poly-dipeptide encoded by the C9orf72 repeat expansion inhibits adenosine deaminase acting on RNA. *J Neurochem* **2021,** *158* (3), 753-765.

150 Wu, R.; Ye, Y.; Dong, D.; Zhang, Z.; Wang, S.; Li, Y.; Wright, N.; Redding-Ochoa, J.; Chang, K.; Xu, S.; Tu, X.; Zhu, C.; Ostrow, L. W.; Roca, X.; Troncoso, J. C.; Wu, B.; Sun, S. Disruption of nuclear speckle integrity dysregulates RNA splicing in C9ORF72-FTD/ALS. *Neuron* **2024,** *112* (20), 3434-3451 e3411.

151 Aladesuyi Arogundade, O.; Nguyen, S.; Leung, R.; Wainio, D.; Rodriguez, M.; Ravits, J. Nucleolar stress in C9orf72 and sporadic ALS spinal motor neurons precedes TDP-43 mislocalization. *Acta Neuropathologica Communications* **2021,** *9* (1), 26.

152 Infield, D. T.; Rasouli, A.; Galles, G. D.; Chipot, C.; Tajkhorshid, E.; Ahern, C. A. Cation-pi Interactions and their Functional Roles in Membrane Proteins. *J Mol Biol* **2021,** *433* (17), 167035.

153 Tao, J.; Frankel, A. D. Specific binding of arginine to TAR RNA. *Proc Natl Acad Sci U S A* **1992,** *89* (7), 2723-2726.

154 Moreno-Villoslada, I.; Jofre, M.; Miranda, V.; Gonzalez, R.; Sotelo, T.; Hess, S.; Rivas, B. L. pH dependence of the interaction between rhodamine B and the water-soluble poly(sodium 4-styrenesulfonate). *J Phys Chem B* **2006,** *110* (24), 11809-11812.

155 Alshareedah, I.; Kaur, T.; Ngo, J.; Seppala, H.; Kounatse, L. D.; Wang, W.; Moosa, M. M.; Banerjee, P. R. Interplay between Short-Range Attraction and Long-Range Repulsion Controls Reentrant Liquid Condensation of Ribonucleoprotein-RNA Complexes. *J Am Chem Soc* **2019,** *141* (37), 14593-14602.

156 Boeynaems, S.; Holehouse, A. S.; Weinhardt, V.; Kovacs, D.; Van Lindt, J.; Larabell, C.; Van Den Bosch, L.; Das, R.; Tompa, P. S.; Pappu, R. V.; Gitler, A. D. Spontaneous driving forces give rise to protein-RNA condensates with coexisting phases and complex material properties. *Proc Natl Acad Sci U S A* **2019,** *116* (16), 7889-7898.

157 Krainer, G.; Welsh, T. J.; Joseph, J. A.; Espinosa, J. R.; Wittmann, S.; de Csillery, E.; Sridhar, A.; Toprakcioglu, Z.; Gudiskyte, G.; Czekalska, M. A.; Arter, W. E.; Guillen-Boixet, J.; Franzmann, T. M.; Qamar, S.; George-Hyslop, P. S.; Hyman, A. A.; Collepardo-Guevara, R.; Alberti, S.; Knowles, T. P. J. Reentrant liquid condensate phase of proteins is stabilized by hydrophobic and non-ionic interactions. *Nat Commun* **2021,** *12* (1), 1085.

158 Boija, A.; Klein, I. A.; Young, R. A. Biomolecular Condensates and Cancer. *Cancer Cell* **2021,** *39* (2), 174-192.

159 Hong, Y.; Najafi, S.; Casey, T.; Shea, J. E.; Han, S. I.; Hwang, D. S. Hydrophobicity of arginine leads to reentrant liquid-liquid phase separation behaviors of arginine-rich proteins. *Nat Commun* **2022,** *13* (1), 7326.

160 Axelrod, D.; Koppel, D. E.; Schlessinger, J.; Elson, E.; Webb, W. W. Mobility measurement by analysis of fluorescence photobleaching recovery kinetics. *Biophys J* **1976,** *16* (9), 1055-1069.

161 Koppel, D. E.; Axelrod, D.; Schlessinger, J.; Elson, E. L.; Webb, W. W. Dynamics of fluorescence marker concentration as a probe of mobility. *Biophysical Journal* **1976,** *16* (11), 1315-1329.

162 Elzie, C. A.; Janetopoulos, C. FRAP analysis of chemosensory components of Dictyostelium. *Methods Mol Biol* **2009,** *571*, 349-369.

163 Poo, M.; Cone, R. A. Lateral diffusion of rhodopsin in the photoreceptor membrane. *Nature* **1974,** *247* (5441), 438-441.

164 Ishikawa-Ankerhold, H. C.; Ankerhold, R.; Drummen, G. P. Advanced fluorescence microscopy techniques--FRAP, FLIP, FLAP, FRET and FLIM. *Molecules* **2012,** *17* (4), 4047-4132.

165 Taylor, N. O.; Wei, M. T.; Stone, H. A.; Brangwynne, C. P. Quantifying Dynamics in Phase-Separated Condensates Using Fluorescence Recovery after Photobleaching. *Biophys J* **2019,** *117* (7), 1285-1300.

166 Drummen, G. P. Fluorescent probes and fluorescence (microscopy) techniques--illuminating biological and biomedical research. *Molecules* **2012,** *17* (12), 14067-14090.

167 Liu, K.; Zhao, Q.; Li, B.; Zhao, X. Raman Spectroscopy: A Novel Technology for Gastric Cancer Diagnosis. *Front Bioeng Biotechnol* **2022,** *10*, 856591.

168 Smekal, A. Zur Quantentheorie der Dispersion. *Die Naturwissenschaften* **1923,** *11* (43), 873-875.

169 Raman, C. V.; Krishnan, K. S. A new type of secondary radiation. *Nature* **1928,** *121* (3048), 501-502.

170 Landsberg, G. S.; Mandelstam, L. I. Eine neue Erscheinung bei der Lichtzerstreuung in Krystallen. *Die Naturwissenschaften* **1928,** *16* (28), 557-558.

171 Kneipp, K.; Kneipp, H.; Itzkan, I.; Dasari, R. R.; Feld, M. S. Ultrasensitive chemical analysis by Raman spectroscopy. *Chem Rev* **1999,** *99* (10), 2957-2976.

172 Devitt, G.; Howard, K.; Mudher, A.; Mahajan, S. Raman Spectroscopy: An Emerging Tool in Neurodegenerative Disease Research and Diagnosis. *ACS Chem Neurosci* **2018,** *9* (3), 404-420.

173 Cutshaw, G.; Uthaman, S.; Hassan, N.; Kothadiya, S.; Wen, X.; Bardhan, R. The Emerging Role of Raman Spectroscopy as an Omics Approach for Metabolic Profiling and Biomarker Detection toward Precision Medicine. *Chemical Reviews* **2023,** *123* (13), 8297-8346.

174 Dodo, K.; Fujita, K.; Sodeoka, M. Raman Spectroscopy for Chemical Biology Research. *J Am Chem Soc* **2022,** *144* (43), 19651-19667.

175 Kuhar, N.; Sil, S.; Verma, T.; Umapathy, S. Challenges in application of Raman spectroscopy to biology and materials. *RSC Adv* **2018,** *8* (46), 25888-25908.

176 Lord, R. C.; Thomas, G. J. Raman Spectral Studies of Nucleic Acids and Related Molecules .I. Ribonucleic Acid Derivatives. *Spectrochimica Acta Part a-Molecular Spectroscopy* **1967,** *A 23* (9), 2551-&.

177 Tripon, C.; Muntean, C. M.; Bratu, I.; Nalpantidis, K.; Deckert, V. (Sub)picosecond processes in DNA and RNA constituents: a Raman spectroscopic assessment. *Polymer Bulletin* **2017,** *74* (10), 4087-4100.

178 Visser, B. S.; Lipinski, W. P.; Spruijt, E. The role of biomolecular condensates in protein aggregation. *Nat Rev Chem* **2024,** *8* (9), 686-700.

179 Riggs, C. L.; Kedersha, N.; Amarsanaa, M.; Zubair, S. N.; Ivanov, P.; Anderson, P. UBAP2L contributes to formation of P-bodies and modulates their association with stress granules. *J Cell Biol* **2024,** *223* (10).

180 Baruch Leshem, A.; Sloan-Dennison, S.; Massarano, T.; Ben-David, S.; Graham, D.; Faulds, K.; Gottlieb, H. E.; Chill, J. H.; Lampel, A. Biomolecular condensates formed by designer minimalistic peptides. *Nat Commun* **2023,** *14* (1), 421.

181 Murakami, K.; Kajimoto, S.; Shibata, D.; Kuroi, K.; Fujii, F.; Nakabayashi, T. Observation of liquid-liquid phase separation of ataxin-3 and quantitative evaluation of its concentration in a single droplet using Raman microscopy. *Chem Sci* **2021,** *12* (21), 7411-7418.

182 Shuster, S. O.; Lee, J. C. Watching liquid droplets of TDP-43(CTD) age by Raman spectroscopy. *J Biol Chem* **2022,** *298* (2), 101528.

183 Li, Y.; Liu, Y.; Yu, X.-Y.; Xu, Y.; Pan, X.; Sun, Y.; Wang, Y.; Song, Y.-H.; Shen, Z. Membraneless organelles in health and disease: exploring the molecular basis, physiological roles and pathological implications. *Signal Transduction and Targeted Therapy* **2024,** *9* (1), 305.

184 Nedelsky, N. B.; Taylor, J. P. Bridging biophysics and neurology: aberrant phase transitions in neurodegenerative disease. *Nat Rev Neurol* **2019,** *15* (5), 272-286.

185 Chen, C.; Jia, H.; Nakamura, Y.; Kanekura, K.; Hayamizu, Y. Effect of Multivalency on Phase-Separated Droplets Consisting of Poly(PR) Dipeptide Repeats and RNA at the Solid/Liquid Interface. *ACS Omega* **2022,** *7* (23), 19280-19287.

186 Rai, S.; Pramanik, S.; Mukherjee, S. Deciphering the liquid-liquid phase separation induced modulation in the structure, dynamics, and enzymatic activity of an ordered protein beta-lactoglobulin. *Chem Sci* **2024,** *15* (11), 3936-3948.

Chapter 2

Spatially Heterogeneous Dynamics of droplets formed by arginine-rich dipeptides and poly-A RNA during liquid-liquid phase separation

The results reported in this chapter are based on the following publication:

Tian, Y; Zhang, Q; Hirai, K; Wen, H; Feng, G; Li, J; Taemaitree, T; Inose, T; Kanekura, K; Uji-I, H. Spatially Heterogeneous Dynamics of droplets formed by arginine-rich dipeptides and poly-A RNA during liquid-liquid phase separation. Molecular Crystals and Liquid Crystals.2024. (DOI: 10.1080/15421406.2024.2353937)

I conducted all the experiments, including the sample preparation and the optical measurements, and analysis of the obtained data. I wrote and revised the manuscript.

2.1 Abstract

Arginine-rich dipeptides (proline-arginine (PR)) are highly toxic products encoded by aberrant repeat expansion in the *C9ORF72* gene, which is the most common cause of familial amyotrophic lateral sclerosis (ALS) and frontotemporal dementia (FTD). These dipeptides have the capability to undergo liquid-liquid phase separation (LLPS) with components inside the membrane-less organelles (MLO) that could have a detrimental effect on fundamental cellular processes, potentially leading to injury or death in motor neurons. In this study, Raman spectroscopy was used to investigate the spatial variation within these liquid droplets *in vitro*, revealing concentration gradients of RNA in droplets. The findings were compared with fluorescence recovery after photobleaching (FRAP), offering insights into the spatially heterogeneous dynamics within the droplets. Understanding the mechanism is essential for unravelling the pathogenesis of neuronal diseases and may provide future therapeutic strategies.

2.2 Introduction

Biological macromolecules, such as proteins and nucleic acids, could undergo local concentration through liquid-liquid phase separation (LLPS), which results in the formation of condensed liquid droplets inside cells[1]. LLPS plays a crucial role in the creation of membrane-less organelles, where various essential vital processes are facilitated, such as ribosomal RNA processing in the nucleolus and the rapid stress response through stress granules. Abnormal LLPS is known to have significant implications in the pathogenesis of neurodegenerative disease, such as amyotrophic lateral sclerosis (ALS)[2] and, even in cancers[3]. The liquid droplets exhibit highly dynamic behaviour, with internal components freely exchanging with the surrounding media, leading to the complex spatiotemporal dynamics of biomolecules in living cells. Consequently, the fluidity of these liquid droplets is a critical factor in LLPS homeostasis, and it is often assessed with fluorescence recovery after photo-bleaching (FRAP) analysis both *in cellulo* and *in vitro*.

Components inside liquid droplets experience various chemical interactions, including charge interactions, π- π interactions, cation- π interactions, hydrophobic interactions, or their combinations. These interactions and the interaction of droplet compenents with the sounding media could induce a gradient in properties from the center region of the droplets to their inner boundary. This gradient leads to the existence of the electric potential in the interface of droplets that extend into the surrounding medium, which has been proven by means of the zeta potential analysis[4]. Consequently, the diffusion behaviour within liquid droplets is anticipated to be spatially heterogeneous. To address the complexity of liquid droplets, FRAP has been applied to analyse the diffusion behaviour[5, 6, 7]. Nevertheless, characterizing the spatial heterogeneity in the behaviour of individual droplets behaviour remains a challenging aspect.

In this study, we employed a combination of Raman spectroscopy and FRAP measurement to examine liquid droplets. Specifically, our focus was on investigating droplets containing Arginine-rich dipeptides [proline-arginine (PR)], which is the most common cause of familial amyotrophic lateral sclerosis (ALS) and frontotemporal dementia (FTD) [8]. PR dipeptides are highly toxic as they disrupt the dynamics of membrane-less organelles (MLO) within cells, including stress granules (SGs) and nucleoli[9, 10, 11, 12, 13]. These poly-PR dipeptides have the ability to sequester the essential proteins within MLO, leading to DNA damage[14] and disruption in the nucleocytoplasmic transport[15]. Additionally, they can interact with RNA-binding proteins inside SGs, further contributing to the pathogenesis of ALS/FTD[9]. However, the molecular dynamics of poly-PR in MLO, including their spatial distribution and molecular diffusion, have remained unclear. Understanding these dynamics is critical for unveiling the toxicity mechanism of polyPR on MLO and its contribution to the pathogenesis of neurodegenerative diseases.

Here, we applied spatially resolved FRAP analysis and Raman spectroscopy to liquid droplets formed by an arginine-rich dipeptide repeat, $(PR)_{20}$ (twenty repeats of proline–arginine) mixed with homopolymeric adenine (poly-A RNA). The result was compared with an artificially designed dipeptide $[(P_4R_4)_5]$ which has the same number of proline and arginine residues but with uneven positioning, resulting in higher binding energy[2]. Our finding revealed that Raman spectroscopy effectively enables the monitoring of the spatial gradient of RNA concentration inside individual droplets, which can be correlated with FRAP analysis. Raman analysis, therefore, offers additional insights into the characteristics of these liquid droplets, aiding in a more comprehensive understanding of their spatial distribution and molecular diffusion.

2.3 Materials and methods

Chemicals Poly-A RNA was purchased from Sigma-Aldrich (#10108626001, 700 – 3,500 kDa) and used without further purifications. $(PR)_{20}$ and $(P_4R_4)_5$ dipeptides were chemically synthesized and purified by Genscript (Piscataway, NJ) with a purity higher than 85%. For fluorescence measurements, poly-A_{15} (15 repeats of adenine) with 5-carboxy-tetramethyl-rhodamine (TAMRA) (TAMRA-rA15) were chemically synthesized and purified by Fasmac (Kanagawa, Japan), respectively.

Droplet preparation 1 mM solution of the arginine-rich dipeptide [$(PR)_{20}$ or $(P_4R_4)_5$] solution and 0.55 mg/mL poly-A were prepared in phosphate-buffered saline (PBS; 049-29793, Wako, pH 7.3, $[Na^+]$ = 152 mM) as stock solutions. Droplets were prepared by vortexing 18 μL of the dipeptide and 45.5 μL of the RNA stock solution in 136.5 μL of PBS buffer filled in 8 well non-coated coverslip (Matsunami) and incubated at room temperature for 3 hours. The final concentrations of the dipeptide and poly-A are 0.09 mM and 0.125 mg/mL, respectively.

For fluorescence microscopy, 1 μL of TAMRA-rA15 solution (0.55 mg/mL) and 44.5 μL of the poly-A stock solution (0.55 mg/mL) were mixed in the 136.5 μL of PBS buffer, followed by vertexing with 18 μL of the peptide stock solution (1 mM) to form fluorescently labelled droplets.

Measurement of fluorescence recovery after photobleaching (FRAP) Fluorescence recovery after photobleaching (FRAP) measurements were conducted using a confocal microscope (A1Rsi, Nikon) equipped with a water-immersion 60× objective (PlanApo, N.A. 1.2, Nikon). After fluorescent dyes were bleached at the central region or inner boundary of a droplet, recovery of fluorescence was followed as a function of time. The half time of fluorescence recovery ($t_{1/2}$) was estimated by following the method described in the previous

reports[16, 17, 18]. All the statistical analyses were performed by running a t-test. *, $p < 0.05$; **, $p < 0.01$; ***, p value<0.001.

Raman microscopy Raman spectroscopy measurement was conducted on a home-built Raman microscopy equipped with an inverted microscope (TiU, Nikon) with 60× air objective (PlanApo, NA 0.95, Nikon), a spectrograph (iHR330, HORIBA) with a CCD camera (Newton BR-DD, Andor Technology), and 638 nm laser (638-06-MILD-180, Cobolt). Raman spectrum was obtained at each point with 50 accumulations of 1 s integration time. The measurement setup of Raman spectroscopy is shown in Figure S2.A1.

2.4 Results and discussion

A mixture of $(PR)_{20}$ or $(P_4R_4)_5$ dipeptides and poly-A RNA in the PBS buffer underwent LLPS *in vitro* at room temperature. We first assessed the morphology of the droplets formed on an uncoated glass coverslip (Figure 2.1). Both the $(PR)_{20}$ and $(P_4R_4)_5$ dipeptides combined with poly-A formed distinct rounded droplets on the glass surface. These droplets, typically ranging in size from a few μm to 10 μm, were observed to form within 2~3 hours of incubation at room temperature. The droplets generally remained stable for a few hours, making them suitable for optical microscopic measurements. However, after more than 6 hours of incubation, many of the droplets lost their round shapes due to the interaction with the glass surface. In this study, only well-defined rounded droplets were subjected to FRAP and Raman spectroscopy.

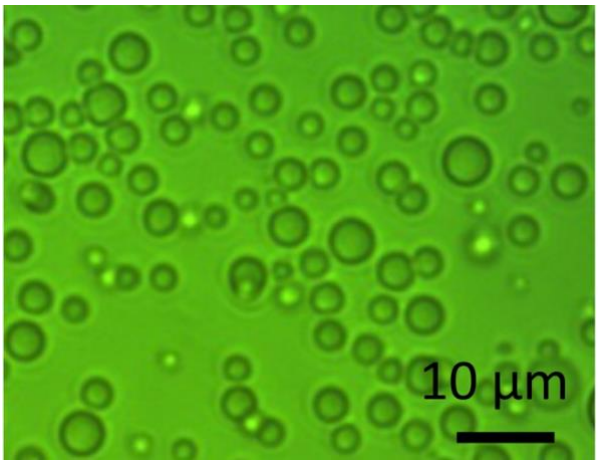

Figure 2.1. Optical transmission images of droplets formed by poly-A and $(PR)_{20}$ peptide in PBS buffer solution after 3 hours incubation at the room temperature.

In order to assess the spatial distribution of fluidity within droplets, the droplets labelled with fluorescent TAMRA-rA15 were subjected to fluorescence measurement. Prior to FRAP measurement, the positions of top and bottom of each droplet were confirmed using the laser focus position of the fluorescence microscope. The laser light was then carefully focused on the middle of each droplet to ensure that the dynamics inside the droplets are monitored by the FRAP measurement. It is worth noting that the half time of fluorescence recovery cannot be properly estimated near the glass surface as the FRAP curves near the surface often show a sigmoidal shape, making precise estimation difficult.

Figure 2.2a and 2.2b present fluorescence snapshots of typical droplets including $(PR)_{20}$ or $(P_4R_4)_5$ during the FRAP measurements, respectively. The corresponding fluorescence recovery curves are displayed in Figure 2.2c and 2.2d, respectively. Each curve exhibits evident photobleaching at the central region or the inner boundary of individual droplets, followed by fluorescence recovery. Analyzing the FRAP curves, we estimated the averaged half recovery time ($\tau_{1/2}$) to be 32.7 ± 8.1 s and 28.1 ± 9.2 s at the central region and the inner boundary of $(PR)_{20}$ / poly-A droplet. For $(P_4R_4)_5$ / poly-A droplet, the estimated $\tau_{1/2}$ values were 39.9 ± 8.6 s and 29.2 ± 5.2 s, respectively. As anticipated, $(P_4R_4)_5$ / poly-A droplets exhibited slower recovery, although the significance was not clearly established, probably due to the limited data points in this in this study (n ~ 10). Given the higher binding energy of $(P_4R_4)_5$ dipeptide resulting from contiguous arginine, it is likely that the droplet has reduced fluidity compared to $(PR)_{20}$ dipeptide[2].

Within each individual droplet, we found a trend of faster fluorescence recovery at the inner boundary, although the significance, as determined by t-tests, was often not conclusively established. Notably, in the case of $(P_4R_4)_5$ / poly-A droplet, a significant difference in recovery time between the center and the inner boundary was observed (Fig. 2.2e). Interestingly, this behavior contradicts the expectation that the bleached area near the boundary of the droplet

should display slower recovery because of the limited diffusions of dye molecule from one side, particularly the side of the droplet interface. The observed rapid fluorescence recovery at the inner boundary is in line with the fact of continuous exchange of components between the inside and outside of the droplets and the surrounding media. However, it is important to note that, given the presence of experimental error in the FRAP measurement, deducing definitive conclusions may be challenging.

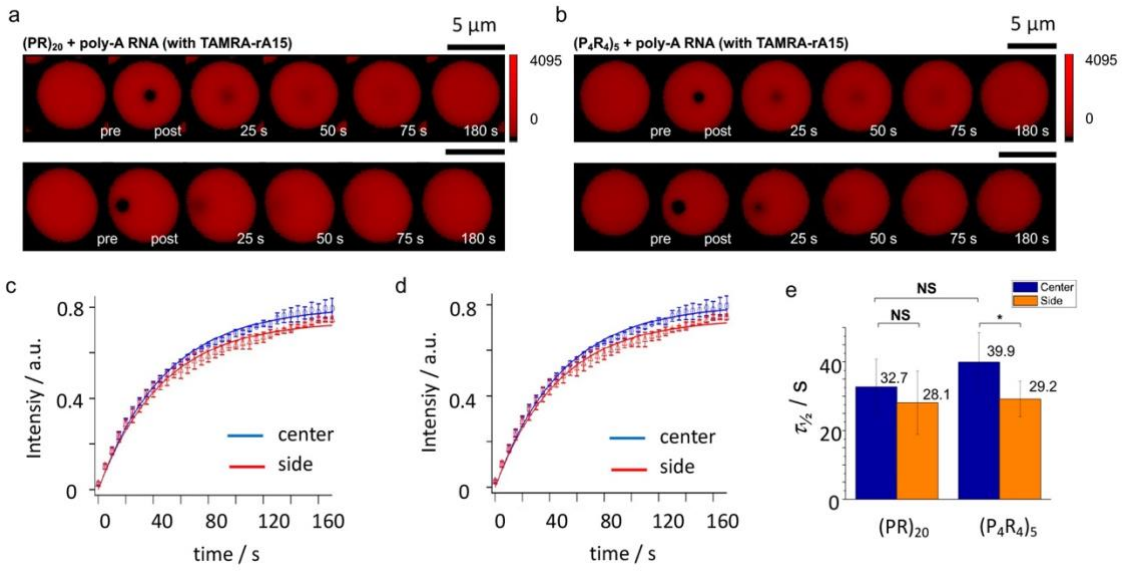

Figure 2.2. FRAP measurements on the droplets. Snapshot of fluorescence images after photobleaching in the droplet of $(PR)_{20}$ / poly-A (a) and that of $(P_4R_4)_5$ / poly-A (b). Averaged FRAP curves at the center (blue line) and the inner boundary (red line) in the droplet of $(PR)_{20}$ / poly-A (c) and that of $(P_4R_4)_5$ / poly-A (d). (e) Averaged half recovery time at the center and inner boundary of $(PR)_{20}$ / poly-A and $(P_4R_4)_5$ / poly-A droplets, respectively. The asterisks indicate the significance in t-test: *, $0.01 < p < 0.05$.

To further explore the spatial heterogeneity of the droplet, Raman spectroscopy was conducted on droplets of ~6 μm in diameter (Figure 2.3). Characteristic peaks of poly-A around ~795 and ~1580 cm^{-1} [19, 20]were identified with minimal interference from the dipeptide. These peaks clearly were evident in both (PR)20 / poly-A and (P4R4)5 / poly-A droplets, as shown in Figure 2.3b and 2.3c, respectively. Figure 2.3c specifically presents the peak intensity at 795 cm^{-1} as a function of the distance from the interface between the droplets and the surrounding media. The Raman signal intensity at the center was obviously higher than that at the inner boundary of the droplet, indicating a higher concentration of poly-A at the center region of the droplet. This observation aligns with the trend identified in the FRAP measurements, where faster diffusion was found near the droplet surface compared to the center of the droplet.

When comparing the relative intensity between the center and the inner boundary, it becomes apparent that concentration gradient of RNA in $(PR)_{20}$ / poly-A droplet is more pronounced than in $(P_4R_4)_5$ / poly-A droplets (Fig. 2.3d). This observation suggests that the difference in the half recovery time between in $(PR)_{20}$ and $(P_4R_4)_5$ droplet cannot be directly attributed to the concentration gradience of RNA inside the droplet. It is likely that RNA strands are interacting with the dipeptides inside droplets, leading to complex diffusion behavior.

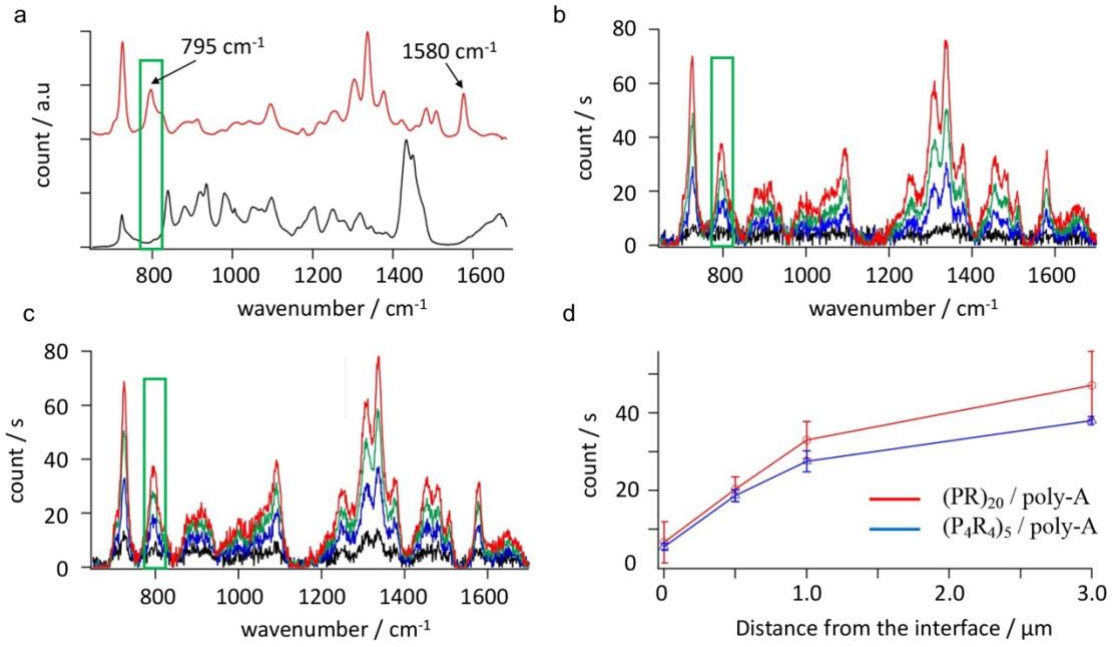

Figure 2.3. Point Raman spectroscopy on the droplets. (a) Reference Raman spectra of poly-A (red line) and $(PR)_{20}$ (black line). (b – c) $(PR)_{20}$ / poly-A (b) and $(P_4R_4)_5$ / poly-A droplets (c), respectively. Spectra were taken at 0 µm (black), 0.5 µm (blue), 1.0 µm (green), and 3.0 µm (red) from the interface, respectively. The green boxes indicate υ(C=C) peak of poly-A RNA. (d) Peak intensity at 795 cm^{-1} as function of the distance from the interface of the droplets of $(PR)_{20}$ / poly-A (red line) and $(P_4R_4)_5$ / poly-A droplets (blue line), respectively.

2.5 Conclusions

The study delved into the spatial dynamics within liquid droplets composed of arginine-rich dipeptides and poly-A RNA, employing a combination of FRAP measurements and Raman microscopy. The FRAP analysis unveiled that poly-A RNA molecules diffuse more rapidly at the inner boundary of droplets compared to their central region. Raman microscopy, on the other hand, indicated a concentration gradient of RNA inside liquid droplet, with lower concentration at the inner boundary and higher concentration to the central region of the droplet. Notably, this concentration gradient aligns with the observed diffusion behaviour. However, the complex interaction between dipeptides and RNA may have additional effects on the diffusion. Although further investigation is warranted, the study demonstrates that Raman microscopy has the potential to contribute to the understanding of the complex dynamics of liquid droplets.

2.6 Appendix

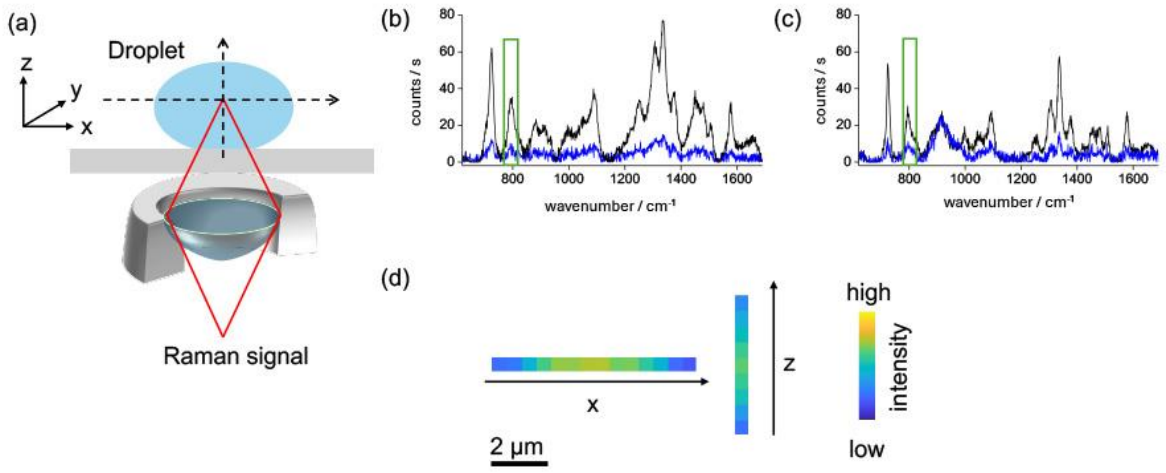

Figure 2.A1. (a) Schematic illustration of a home-built Raman spectroscopy system equipped with an inverted microscope. A 638 nm laser was used for Raman spectroscopy. (b) Raman scattering spectra collected at the center (black line) and edge (blue line) of the droplets. The Raman scattering signal in the green box was used to generate the intensity map along the x-scan direction in (d). (c) Raman scattering spectra collected at the center (black line) and bottom near the glass surface (blue line) of the droplets. The Raman scattering signal in the green box was used to generate the intensity map for the z-scan in (d). (d) Raman scattering intensity maps of the liquid droplets sweeping in the x and z directions.

2.7 References

1 Brangwynne, C. P.; Mitchison, T. J.; Hyman, A. A. Active liquid-like behavior of nucleoli determines their size and shape in Xenopus laevis oocytes. *Proc Natl Acad Sci U S A* **2011,** *108* (11), 4334-4339.

2 Chen, C.; Yamanaka, Y.; Ueda, K.; Li, P.; Miyagi, T.; Harada, Y.; Tezuka, S.; Narumi, S.; Sugimoto, M.; Kuroda, M.; Hayamizu, Y.; Kanekura, K. Phase separation and toxicity of C9orf72 poly(PR) depends on alternate distribution of arginine. *J Cell Biol* **2021,** *220* (11).

3 Klein, I. A.; Boija, A.; Afeyan, L. K.; Hawken, S. W.; Fan, M.; Dall'Agnese, A.; Oksuz, O.; Henninger, J. E.; Shrinivas, K.; Sabari, B. R.; Sagi, I.; Clark, V. E.; Platt, J. M.; Kar, M.; McCall, P. M.; Zamudio, A. V.; Manteiga, J. C.; Coffey, E. L.; Li, C. H.; Hannett, N. M.; Guo, Y. E.; Decker, T. M.; Lee, T. I.; Zhang, T.; Weng, J. K.; Taatjes, D. J.; Chakraborty, A.; Sharp, P. A.; Chang, Y. T.; Hyman, A. A.; Gray, N. S.; Young, R. A. Partitioning of cancer therapeutics in nuclear condensates. *Science* **2020,** *368* (6497), 1386-1392.

4 Welsh, T. J.; Krainer, G.; Espinosa, J. R.; Joseph, J. A.; Sridhar, A.; Jahnel, M.; Arter, W. E.; Saar, K. L.; Alberti, S.; Collepardo-Guevara, R.; Knowles, T. P. J. Surface Electrostatics Govern the Emulsion Stability of Biomolecular Condensates. *Nano Lett* **2022,** *22* (2), 612-621.

5 Phair, R. D.; Misteli, T. High mobility of proteins in the mammalian cell nucleus. *Nature* **2000,** *404* (6778), 604-609.

6 Stixova, L.; Bartova, E.; Matula, P.; Danek, O.; Legartova, S.; Kozubek, S. Heterogeneity in the kinetics of nuclear proteins and trajectories of substructures associated with heterochromatin. *Epigenetics Chromatin* **2011,** *4* (1), 5.

7 Taylor, N. O.; Wei, M. T.; Stone, H. A.; Brangwynne, C. P. Quantifying Dynamics in Phase-Separated Condensates Using Fluorescence Recovery after Photobleaching. *Biophys J* **2019,** *117* (7), 1285-1300.

8 Mitrea, D. M.; Mittasch, M.; Gomes, B. F.; Klein, I. A.; Murcko, M. A. Modulating biomolecular condensates: a novel approach to drug discovery. *Nat Rev Drug Discov* **2022,** *21* (11), 841-862.

9 Boeynaems, S.; Bogaert, E.; Kovacs, D.; Konijnenberg, A.; Timmerman, E.; Volkov, A.; Guharoy, M.; De Decker, M.; Jaspers, T.; Ryan, V. H.; Janke, A. M.; Baatsen, P.; Vercruysse,

T.; Kolaitis, R. M.; Daelemans, D.; Taylor, J. P.; Kedersha, N.; Anderson, P.; Impens, F.; Sobott, F.; Schymkowitz, J.; Rousseau, F.; Fawzi, N. L.; Robberecht, W.; Van Damme, P.; Tompa, P.; Van Den Bosch, L. Phase Separation of C9orf72 Dipeptide Repeats Perturbs Stress Granule Dynamics. *Mol Cell* **2017,** *65* (6), 1044-1055 e1045.

10 Kwon, I.; Xiang, S.; Kato, M.; Wu, L.; Theodoropoulos, P.; Wang, T.; Kim, J.; Yun, J.; Xie, Y.; McKnight, S. L. Poly-dipeptides encoded by the C9orf72 repeats bind nucleoli, impede RNA biogenesis, and kill cells. *Science* **2014,** *345* (6201), 1139-1145.

11 Wen, X.; Tan, W.; Westergard, T.; Krishnamurthy, K.; Markandaiah, S. S.; Shi, Y.; Lin, S.; Shneider, N. A.; Monaghan, J.; Pandey, U. B.; Pasinelli, P.; Ichida, J. K.; Trotti, D. Antisense proline-arginine RAN dipeptides linked to C9ORF72-ALS/FTD form toxic nuclear aggregates that initiate in vitro and in vivo neuronal death. *Neuron* **2014,** *84* (6), 1213-1225.

12 White, M. R.; Mitrea, D. M.; Zhang, P.; Stanley, C. B.; Cassidy, D. E.; Nourse, A.; Phillips, A. H.; Tolbert, M.; Taylor, J. P.; Kriwacki, R. W. C9orf72 Poly(PR) Dipeptide Repeats Disturb Biomolecular Phase Separation and Disrupt Nucleolar Function. *Mol Cell* **2019,** *74* (4), 713-728 e716.

13 Lee, K. H.; Zhang, P.; Kim, H. J.; Mitrea, D. M.; Sarkar, M.; Freibaum, B. D.; Cika, J.; Coughlin, M.; Messing, J.; Molliex, A.; Maxwell, B. A.; Kim, N. C.; Temirov, J.; Moore, J.; Kolaitis, R. M.; Shaw, T. I.; Bai, B.; Peng, J.; Kriwacki, R. W.; Taylor, J. P. C9orf72 Dipeptide Repeats Impair the Assembly, Dynamics, and Function of Membrane-Less Organelles. *Cell* **2016,** *167* (3), 774-788 e717.

14 Farg, M. A.; Konopka, A.; Soo, K. Y.; Ito, D.; Atkin, J. D. The DNA damage response (DDR) is induced by the C9orf72 repeat expansion in amyotrophic lateral sclerosis. *Hum Mol Genet* **2017,** *26* (15), 2882-2896.

15 Tang, X.; Toro, A.; T, G. S.; Gao, J.; Chalk, J.; Oskarsson, B.; Zhang, K. Divergence, Convergence, and Therapeutic Implications: A Cell Biology Perspective of C9ORF72-ALS/FTD. *Mol Neurodegener* **2020,** *15* (1), 34.

16 Kimura, H.; Cook, P. R. Kinetics of core histones in living human cells: little exchange of H3 and H4 and some rapid exchange of H2B. *J Cell Biol* **2001,** *153* (7), 1341-1353.

17 Kitamura, A.; Kubota, H.; Pack, C. G.; Matsumoto, G.; Hirayama, S.; Takahashi, Y.; Kimura, H.; Kinjo, M.; Morimoto, R. I.; Nagata, K. Cytosolic chaperonin prevents polyglutamine toxicity with altering the aggregation state. *Nat Cell Biol* **2006,** *8* (10), 1163-

1170.

18 Tsutsumi, M.; Muto, H.; Myoba, S.; Kimoto, M.; Kitamura, A.; Kamiya, M.; Kikukawa, T.; Takiya, S.; Demura, M.; Kawano, K.; Kinjo, M.; Aizawa, T. In vivo fluorescence correlation spectroscopy analyses of FMBP-1, a silkworm transcription factor. *FEBS Open Bio* **2016,** *6* (2), 106-125.

19 Hirakawa, A. Y.; Okada, H.; Sasagawa, S.; Tsuboi, M. Infrared and Raman spectra of adenine and its 15N and 13C substitution products. *Spectrochimica Acta Part A: Molecular Spectroscopy* **1985,** *41* (1-2), 209-216.

20 Wilson, A. L.; Outeiral, C.; Dowd, S. E.; Doig, A. J.; Popelier, P. L. A.; Waltho, J. P.; Almond, A. Deconvolution of conformational exchange from Raman spectra of aqueous RNA nucleosides. *Commun Chem* **2020,** *3* (1), 56.

Chapter 3

Raman spectroscopy and FRAP analysis on density heterogeneity and diffusion behavior of complex coacervation by arginine-rich dipeptides and poly-A RNA

The results reported in this chapter are based on the following publication:

Tian Y.，Zhang Q.，Li J.T.，Tsutsumi M.，Inose T.，Taemaitree F.，Hirai K.，Kanekura K.，Uji-i H, Raman spectroscopy and FRAP analysis on density heterogeneity and diffusion behavior of complex coacervation by arginine-rich dipeptides and poly-A RNA, ACS Omega. 2025．(DOI: 10.1021/acsomega.5c04844)

I contributed to the experimental design of the combination of FRAP and Raman spectroscopy and conducted all the experiments. I wrote and revised the manuscript.

3.1 Abstract

Membrane-less organelles (MLOs), formed through liquid-liquid phase separation (LLPS), are vital for various cellular functions, including gene expression and RNA metabolism. Destructions in LLPS dynamics, often due to aberrant condensate formation, are implicated in neurodegenerative diseases. Polypeptides composed of repeated dipeptides, namely arginine-rich dipeptide repeat proteins, poly(proline-arginine) (poly-PR) and poly(glycine-arginine) (poly-GR), translated from mutated *C9ORF72* repeats, undergo LLPS and disrupt RNA and protein homeostasis. Although these peptides have similar net charges, they exhibit different diffusion behaviors in liquid droplet, indicating that sequence-specific charge distribution may influence LLPS dynamics. In this study, we combined fluorescence recovery after photobleaching (FRAP) and Raman spectroscopy to examine the density heterogeneity and diffusion behavior of LLPS droplets formed by arginine-rich dipeptides and homo-polymeric adenine RNA (poly-A RNA). We analyzed $(PR)_{20}$, $(P_4R_4)_5$, (same components but different charge pattern), and $(GR)_{20}$ (same net charge as $(PR)_{20}$, but different sequence). Our results showed that droplets formed with different dipeptides displayed heterogeneous diffusion behaviors, which strongly correlated with internal density gradients within individual droplets detected by Raman spectroscopy. This suggests that charge patterning, not just net charge, critically influences LLPS dynamics. FRAP results of small dye molecules with different net-charges aligns with the concentration gradient of RNA and dipeptides obtained by Raman spectroscopy. Raman spectroscopy combined with FRAP provides a powerful approach for revealing the biophysical properties of biomolecular condensates.

3.2 Introduction

Membrane-less organelles (MLOs), or biomolecular condensates formed through liquid-liquid phase separation (LLPS) have attracted significant attention over the past 15 years.[1] These highly dynamic liquid droplets, composed of various charged biological macromolecules, such as proteins and nucleic acids, are involved in numerous essential biological processes,[2] including protein localization, supramolecular assembly, gene expression, gene transcription, RNA metabolism, minimizing cellular noise, genome packaging control, cell-cycle control.[3, 4, 5] In contrast, LLPS-driving condensation can also result in the formation of undesirable protein aggregates, disturbing dynamics and functions of MLOs.[6, 7, 8] Such dysfunctions are linked to insoluble protein aggregate observed in the neurons of patients with neurodegenerative diseases[9] and abnormal MLOs dynamics caused by toxic dipeptides in amyotrophic lateral sclerosis (ALS).[10] Thus, understanding the fluidity differences of liquid droplets is crucial for elucidating the role of LLPS homeostasis in disease progression. Currently, fluorescence recovery after photobleaching (FRAP) is a widely used method to address LLPS dynamics both *in vivo* and *in vitro*.

LLPS is driven by multiple weak interactions, including electrostatic, cation-π, π-π, hydrophobic interactions, and hydrogen bonding.[11, 12] These interactions determine droplet formation and stability and influence their dynamic properties. The combination of oppositely charged polymers can create an electrostatic (Galvani) potential between the droplets and its surrounding media, a phenomenon supported by liquid-state theory[13] and confirmed via zeta potential measurements.[14] Recently, many studies have focused on liquid–liquid phase separation achieved by mixing RNA with positively charged polypeptides. These electrostatic gradients may significantly influence behavior and physical properties of phase-separated droplets.

Polypeptides composed of repeated dipeptides, namely arginine-rich dipeptide repeat proteins, such as poly(proline-arginine, PR) and poly(glycine-arginine, GR), produced via repeat-associated non-ATG (RAN) translation of the mutated *chromosome 9 open reading frame 72* (*C9ORF72*) gene, are highly toxic *in vitro* and *in vivo* and contribute to ALS and frontotemporal dementia (FTD).[15, 16, 17] These dipeptides interact with RNA and proteins through abnormal LLPS, disturbing the homeostasis of RNA[6,18] and protein metabolism.[19, 20] Both poly(PR) and poly(GR) are positively charged and accumulate in nucleolus, impairing nucleolar dynamics and inhibiting ribosomal RNA (rRNA) processing and protein translation.[6, 19] Despite similar propensities for LLPS, poly(GR) exhibits slower diffusion than poly(PR) both *in cellular* and *in vitro*,[19, 21] though the reason for these differences remains unclear. *In vitro*, arginine-rich dipeptides undergo complex coacervation with RNA via electrostatic and π-system interactions.[22] Recent studies suggest that variations in charge distribution along the dipeptide sequence significantly affect binding energies and droplet dynamics, even when the net charge is identical.[12, 21]

Although prior fluorescence microscopic studies using fluorescently labeled biomolecules have revealed different droplet dynamics *in vitro*,[22] the underlying causes of these differences remain poorly understood. Given the charged nature of biopolymers within droplets, their diffusion behavior may vary. Understanding how charge properties influence droplet dynamics is key to uncovering these mechanisms.

To address these questions, we prepared and analysed LLPS droplets formed by arginine-rich dipeptides with distinct charge properties using Raman spectroscopy and FRAP analysis. Raman spectroscopy, a molecular vibrational technique capable of providing the internal composition of droplets, has proven powerful in elucidating molecular interaction in LLPS system.[23, 24, 25, 26, 27, 28] In this study, we investigated droplets formed by mixing homopolymeric adenine (poly-A RNA) with three arginine-rich dipeptides: $(PR)_{20}$ (20 repeats of proline and

arginine), $(P_4R_4)_5$ (five repeats of four proline and four arginine, with the same net charge and component but different charge patterning), and $(GR)_{20}$ (20 repeats of glycine and arginine, with the same net charge and charge patterning but different components and weaker charge separation).[21] Using FRAP and Raman spectroscopy, we observed spatial density gradients and heterogenous diffusion dynamics within droplets, consistent with our previous results.[29] We observed higher density of both fluorescently-labeled RNA and positively charged polypeptides at the center region compared to that at the near boundary within individual liquid droplet by analyzing the Raman intensity maps. Spatially homogeneous Raman intensity ratio between dipeptide and RNA within individual liquid droplets indicated the formation of stable RNA-dipeptide complexes. FRAP analysis of fluorescently-labeled RNA and various small dye molecules with different net-charges further indicated slower diffusion at the center region compared to that at the near boundary within individual liquid droplets. Further analysis in the ratio of center-to-boundary recovery time between $(GR)_{20}$ and $(PR)_{20}$ droplets suggest that only negatively charged fluorescein could form stronger interaction with $(GR)_{20}$ compared to $(PR)_{20}$ and $(P_4R_4)_5$. Spatially heterogeneous diffusion dynamics of molecules within droplets observed with FRAP analysis strongly correlate with droplet density measured by Raman spectroscopy. These findings demonstrate that the combination of FRAP and Raman spectroscopy offers complementary insights into how the charge properties of droplet components influence the complex dynamic behaviors of LLPS-based biomolecular condensates.

3.3 Experimental Section

Chemicals. The peptides $(PR)_{20}$, $(GR)_{20}$, and $(P_4R_4)_5$ were chemically synthesized by Genscript (Piscataway, NJ) with a purity greater than 85%. Poly-A RNA (700 – 3,500 kDa) was purchased from Sigma-Aldrich and used without further purification. TAMRA-rA_{15} (5-carboxy-tetramethyl-rhodamine (TAMRA) labeled poly-A15 (15 repeats of adenine) was synthesized and purified by Fasmac (Kanagawa, Japan).

Phase separation assay. Stock solution of arginine-rich dipeptide [$(PR)_{20}$, $(GR)_{20}$ or $(P_4R_4)_5$] were prepared at ~ 1 mM in phosphate-buffered saline (PBS; 049-29793, Wako, pH 7.3, [Na^+] = 152 mM). A poly-A RNA stock solution was prepared at 0.55 mg/mL in the same PBS. To estimate dipeptide concentration of each solution, the absorbance at 205 nm (A_{205}) of 12-fold diluted stock solution was measured using a UV-Vis spectrophotometer (VL0000D0, Thermo Scientific), based on the absorbance contribution of peptide bonds and side chains.[30, 31] Stock solution of small dye molecules, TAMRA, Rhodamine B, and fluorescein, were also prepared at 1 mM in PBS.

For Raman spectroscopy, fluorescently non-labelled droplets were prepared. Shortly, 45.5 μL of the poly-A RNA stock solution was diluted with 136.5 μL of PBS buffer. Then, 18 μL of the peptide stock solution was added and vortexed. The mixture was transferred to an 8 well non-coated coverslip (Matsunami) and incubated for 3 hours at room temperature.

For FRAP measurement of fluorescently labeled RNA, 1 μL of TAMRA-rA_{15} (0.55 mg/mL) was mixed with 44.5 μL of the poly-A stock solution in 136.5 μL of PBS, followed by vortexing with 18 μL of the peptide stock solution. The mixture was incubated in an 8 well non-coated coverslip for 3 hours at room temperature to form fluorescently labeled droplets. For FRAP analysis of small dyes, 1 μL of the stock solution of TAMRA, Rhodamine B or

fluorescein was mixed with 45.5 μL of the poly-A stock solution in 135.5 μL of PBS, then vortexed with 18 μL of the $(PR)_{20}$ or $(GR)_{20}$ stock solution and incubated at room temperature for 3 hours to form droplets labeled with free dye molecules. The final concentrations of poly-A RNA were approximately 0.125 mg/mL in all solutions.

FRAP analysis. FRAP experiments were conducted using a confocal microscope (A1Rsi, Nikon) equipped with a 60x water-immersion objective (PlanApo, NA 1.2, Nikon), following the protocols described previously.[29, 34] Fluorescein was excited by a 488 nm laser, and the emission signal was detected through a 525/50 bandpass filter. TAMRA, RhB and TAMRA-rA_{15} were excited by a 561 nm laser, and the emission signal was detected through a 593/46 bandpass filter. A small area (approximately 1.0 μm diameter circle) was selected within a liquid droplet. The central or inner boundary region of individual droplets was bleached with 8 scans using 10% (approximately 2 μW, 488 nm) laser power for fluorescein fluorescently labeled droplets, or 19% (approximately 2 μW, 561 nm) laser power for TAMRA, RhB and TAMRA-rA_{15} fluorescently labeled droplets, and the fluorescence recovery was recorded over time. Snapshots were then collected using as low laser power as 0.1% (at 10 nW range) every 1 s for 34 sec (for the small dye molecules fluorescently labeled droplets showing fast fluorescence recovery) or every 5.0 s for 2.5 min (for TAMRA-rA_{15} fluorescently labeled droplets showing slow fluorescence recovery). The relative fluorescence intensities in the bleached area were normalized using the average intensity of three images measured before photobleaching. The normalized intensities were analyzed using a fitting equation for a single exponential association model and the fluorescent half-recovery time ($\tau_{1/2}$) was calculated following previously reported methods.[32, 33, 34] Statistical analyses were performed by a Student's t-test: *, p <0.05; **, p <0.01; ***, p value<0.001.

Raman spectroscopy. Raman measurements were performed using a home-built Raman microscope based on an inverted microscope (TiU, Nikon) with 60x air objective (PlanApo,

NA 0.95, Nikon), a spectrograph (iHR330, HORIBA) and a CCD camera (Newton DU920P–BEX2–DD, Andor Technology). A 638 nm laser (638-06-MILD-180, Cobolt) was used as the excitation source. Raman scattering was collected through a confocal pinhole and a long pass filter (BLP01-647R, Semrock). Single-point Raman spectra were recorded at the center region of individual droplets with 1 s exposure time and 300 accumulations. Raman intensity mapping of individual droplets was performed using Omega software (AIST-NT) with 1 s exposure time and 50 accumulations per pixel. Reference Raman spectra of dipeptides and poly-A RNA in Milli-Q water (18 MΩ cm, Milli-Q System, Millipore) were acquired under the same conditions with 1 s exposure and 1000 accumulations. Raman spectra in each mapping were normalized using spectra obtained from the PBS surrounding droplets. A wavelet transform is applied to each spectrum to optimize denoising and background removal (see Figure 3.A1).

3.4 Results and discussion

Raman Spectroscopic Analysis of Liquid Droplets: Mixture of dipeptides and poly-A formed spherical droplets ranging from a few to ten μm in diameter after 3 hours of incubation. Although some non-spherical droplets were present, the spherical droplets maintained their shape for several hours on the glass surface at room temperature and were used for Raman spectroscopy in this study. To elucidate the vibrational modes and potential interactions between the dipeptides and poly-A within droplets, Raman spectroscopy was performed on droplets approximately 6 μm in diameter. Figure 3.1a and 3.1b show representative Raman spectra of droplets composed of $(PR)_{20}$ / poly-A and $(GR)_{20}$ / poly-A, respectively. For comparison, the reference Raman spectra of $(PR)_{20}$, $(GR)_{20}$ and poly-A are also presented in Figure 3.1. The Raman spectra of the liquid droplets display Raman peaks associated with both arginine-rich dipeptides and poly-A RNA (peak assignments are summarized in Table 3.1).[35, 36, 37] A prominent feature of the spectra is a peak around ~1580 cm^{-1}, which is attributed to the υ(C=C) stretching mode of adenine of poly-A.[35] Additionally, a peak at 1450 cm^{-1} was observed in $(PR)_{20}$-containing droplets and a similar peak around 1445 cm^{-1} appeared in droplets with $(GR)_{20}$. These peaks likely correspond to CH_2 /CH_3 deformation modes from the side chain of the arginine-rich dipeptides.[26, 38, 39] Notably, the peak at 1437 cm^{-1}, associated with N-H deformation of the guanidinium moiety in arginine, was suppressed upon droplet formation. This suppression suggests hydrogen bonding between arginine residues and the adenine bases of RNA.[40]

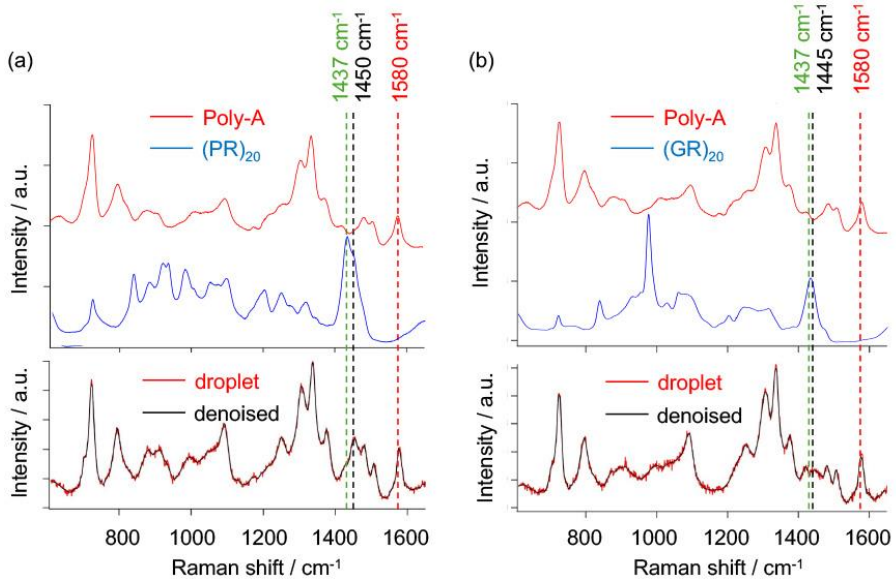

Figure 3.1. Single-point Raman spectroscopy of liquid droplets. Comparison of typical Raman peaks observed in liquid droplets with reference Raman spectra of dipeptides and poly-A RNA. (a) Reference Raman spectra of poly-A RNA (red line) and $(PR)_{20}$ (blue line) (top), and the Raman spectrum measured at the center of a $(PR)_{20}$ / poly-A droplet (bottom). (b) Reference Raman spectra of poly-A RNA (red line) and $(GR)_{20}$ (blue line) (top), and the Raman spectrum measured at the center of a $(GR)_{20}$ / poly-A droplet (bottom). Dashed lines indicate characteristic peaks corresponding to dipeptide (green and black dashed lines) and poly-A RNA (red dashed lines), respectively. The peak at 1437 cm^{-1}, attributed to N-H deformation of the guanidinium moiety of arginine, is observed in both $(PR)_{20}$ and $(GR)_{20}$.

Table 3.1. Assignment of characteristic experimental vibrations of each $(PR)_{20}$ / poly-A RNA droplet to specific vibrational modes.

Peak (cm^{-1})	Assignment
1580	Adenine, C=C (V base), in plane
1510	Adenine, vibrations of benzene, skeletal stretching
1452	Arginine, CH_2/CH_3 deformation modes
1437	Arginine, N–H deformations of the guanidinium moiety of arginine
937	Arginine, C-C; N-C-N; C-N
843	Proline, skeletal vibrations
795	Adenine, C=C
726	Adenine, ring-breathing mode vibration
597	Bending of COO^-

Since the spontaneous Raman scattering intensity is proportional to the molecular concentration, the density of the liquid droplet can be analysed by Raman spectroscopy. In this experiment, the concentration of $(PR)_{20}$ and $(GR)_{20}$ are estimated to be 1.20 mM and 1.06 mM, respectively (Figure 3.A4). Comparing Raman spectra of liquid droplet with these dipeptides and the same amount of poly-A RNA, we found that higher Raman scattering from the droplets consisting of $(GR)_{20}$ / poly-A RNA is 1.1 to 1.2 times higher than that of $(PR)_{20}$ / poly-A RNA droplet (Figure 3.A5), indicating a higher density of $(GR)_{20}$ / poly-A RNA complexes in the corresponding droplets. Since spontaneous Raman scattering intensity is proportional to the

molecular concentration, the density of the liquid droplet can be analysed using Raman spectroscopy. From the UV-Vis spectroscopy, the concentration of $(PR)_{20}$ and $(GR)_{20}$ in the stock solutions were estimated to be 1.20 mM and 1.06 mM, respectively (Figure 3.A4). By comparing Raman spectra of droplet formed from these dipeptides with an equal amount of poly-A, we found that the Raman scattering intensity from $(GR)_{20}$ / poly-A droplets was 1.1 to 1.2 times higher than that from $(PR)_{20}$ / poly-A droplet (Figure 3.A5), indicating a higher density of $(GR)_{20}$ / poly-A complexes within the droplets.

To further gain insights into the spatial information of liquid droplets (Figure 3.2a), Raman mapping was performed across the droplets (Figure 3.2b). Figure 3.2c and 3.2d show Raman intensity map along the x- and z-direction, respectively, where the peak intensity at 1580 cm^{-1} [corresponding to υ(C=C) of poly-A RNA] was used to visualize RNA distribution within a droplet. No Raman peaks were observed outside the droplet, while the characteristic peaks of $(PR)_{20}$ and poly-A RNA are clearly detected inside. The Raman maps reveal a slightly compressed spherical shape of the droplet in z-direction, measuring approximately 5 μm of diameter in the xy-plane and ~3.5 μm in the z-direction for the droplet shown in Figure 3.2c and 3.2d. Note that, in Figure 3.2c, the spectrum at position #1 displays Raman scattering at the edge of the droplet, where a part of the laser excitation light is focused inside and the other part outside. In contrast, at the position #3, the laser focus is entirely inside the droplet. The Raman scattering intensity of υ(C=C) peak at the center of the droplet (position #7) is significantly higher than that near the inner boundary (position #3 - 4), indicating a higher density of poly-A RNA at the center of the droplet. The intensity maps at 1450 or 1445 cm^{-1}, corresponding to CH_2/CH_3 deformation modes of the dipeptides, show similar trends (Figure 3.A2).

Despite the presence of concentration gradients for RNA and dipeptides, the intensity ratio map between the peaks at 1450 (dipeptide-related) and 1580 cm^{-1} (poly-A-related), I_{1450}/I_{1580},

remained relatively homogeneous across the $(PR)_{20}$ droplets (Figure 3.2e, top). (See the Figure 3.2f and 3.2g top for the corresponding intensity ratio maps across the $(P_4R_4)_5$ and $(GR)_{20}$ droplets, respectively.) This uniform ratio suggests the formation of stable RNA-dipeptide complexes, likely driven by strong interaction between them, electrostatic, cation- π, π - π, and/or hydrophobic interactions.[41, 42, 43]

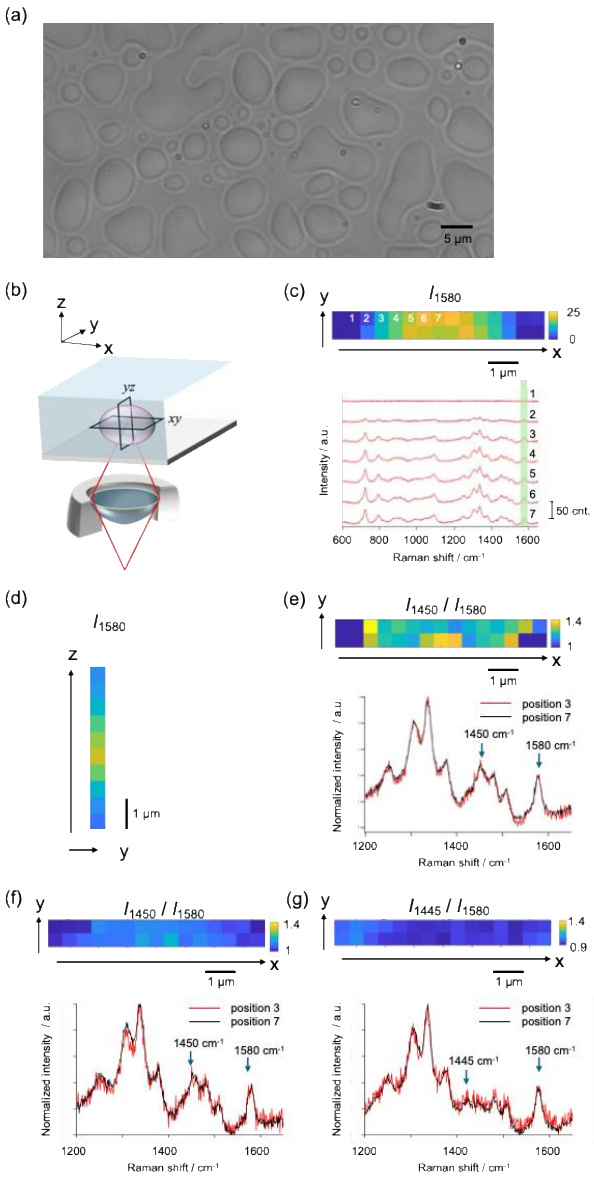

Figure 3.2. Raman mapping of liquid droplets composed of $(PR)_{20}$ and poly-A RNA. (a) A typical optical transmission image of $(PR)_{20}$ / poly-A RNA droplets. Only spherical droplets were analysed in this study. (b) Schematic illustration defining the axis used for Raman microscopy measurements. (c) Raman intensity map of a liquid droplet by scanning along the x-axis (top). Raman scattering spectra collected at various positions: one spectrum from outside of the droplet (position #1) and a series of spectra from the edge to the center of the droplet (position #2 to #7) (bottom). The light green background at 1580 cm^{-1}, which is attributed to υ(C=C), indicates the presence of RNA. (d) Raman intensity map of the droplet obtained by scanning along the z-axis. (e-g) Intensity ratio of the Raman peaks at 1450 cm^{-1} or 1445 cm^{-1} (dipeptide related) and 1580 cm^{-1} (RNA related), I_{1450}/I_{1580}, or I_{1445}/I_{1580} acquired along the x-axis (top) within droplets composed of $(PR)_{20}$ / poly-A RNA (e), $(P_4R_4)_5$ / poly-A RNA (f) and $(GR)_{20}$ / poly-A RNA droplets (g), respectively. Normalized Raman spectra at positions #3 and #7 are shown for comparison (bottom).

We examined the density heterogeneity of $(P_4R_4)_5$, which has the same net charge as $(PR)_{20}$ but different charge patterning, and in $(GR)_{20}$ which shares both the same net charge and charge patterning as $(PR)_{20}$ but insufficient charge separation and different amino acid components.[21] Raman intensity maps at 1580 cm^{-1} (RNA related) and 1450 cm^{-1} (dipeptide related) for $(PR)_{20}$ / poly-A (Figure 3.A2a), $(P_4R_4)_5$ / poly-A (Figure 3.A2b), and 1580 cm^{-1} and 1445 cm^{-1} for $(GR)_{20}$ / poly-A droplets (Figure 3.A2c) reveal clear concentration gradients of poly-A RNA and dipeptides from the center to the inner boundary of the droplets. These suggest that arginine-rich dipeptides play a crucial role in forming hierarchical structure within liquid droplets. Interestingly, although $(GR)_{20}$, $(PR)_{20}$, and $(P_4R_4)_5$ share the same isoelectric point (e.g., pI=12.37),[44] the peak intensity at 1580 cm^{-1} is significantly higher in $(GR)_{20}$ droplet compared to $(PR)_{20}$ and $(P_4R_4)_5$ droplet (Figure 3.A3), indicating a greater accumulation of

RNA in $(GR)_{20}$ droplet. This is particularly notable given that the stock concentration of $(GR)_{20}$ (1.06 mM) is lower than that of $(PR)_{20}$ (1.20 mM) (Figure 3.A4).

Despite both peptides containing arginine residues and having the same pI, the difference in charge distribution and structural flexibility likely influences their binding behavior to RNA. In $(PR)_{20}$, the cyclic structure of proline spatially separates arginine residues, weakening electrostatic interactions with the negatively charged RNA backbone and resulting in partial binding with RNA.[45] In contrast, $(GR)_{20}$ contains glycine, of which a minimal side chain (a single hydrogen atom) does not disrupt arginine clustering. This results in a block-like positive charge pattern that strengthens electrostatic attraction to poly-A RNA.[21, 45, 46] Furthermore, the guanidinium groups of arginine in $(GR)_{20}$ can participate in a variety of interactions, including electrostatic interactions to phosphate backbone and cation–π and π–π stacking interactions with adenine bases.[47] These diverse interaction modes allow individual arginine residues to engage with multiple RNA sites, supporting cooperative rather than competitive binding.[47, 48] Additionally, the structural flexibility of $(GR)_{20}$ due to glycine spacers, enhances its ability to conform to RNA and form π–π interactions more than the rigid proline-containing $(PR)_{20}$.[47, 49, 50] This structural flexibility likely contributes to the higher RNA recruitment in $(GR)_{20}$-containing droplets, as reflected by the increased Raman scattering intensity associated with RNA (Figure 3.A5a). Therefore, despite its lower initial concentration, $(GR)_{20}$ exhibits a stronger capability to accumulate RNA within droplets. This is likely driven by its clustered positive charges, conformational flexibility, and ability to form multivalent interactions.

Diffusion Behavior of poly-A RNA in Liquid Droplets: To elucidate the molecular diffusion dynamics within liquid droplets, we performed FRAP measurements. In the initial set of experiments, FRAP was conducted using fluorescently labeled poly-A RNA (TAMRA-rA_{15}) to monitor the diffusion behavior of arginine-rich dipeptide/RNA complexes (Figuer 3.3). For this purpose, TAMRA-rA_{15} was mixed with unlabeled poly-A at a concentration of 2.25 wt%

and incubated with the dipeptides. Figure 3.3a presents representative fluorescence snapshots of $(PR)_{20}$ / poly-A droplets during FRAP measurements, showing fluorescence recovery after photobleaching at the central region (Figure 3.3a top) and near the inner boundary (Figure 3.3a bottom) of the droplet. The corresponding fluorescence recovery curves as a function of time are shown in Figure 3.3b. The averaged half-recovery time ($\tau_{1/2}$) was estimated to be 37.6 ± 4.4 s at the center and 32.1 ± 3.3 s near the inner boundary (Figure 3.3b and 3.3e, respectively). Similar measurements were conducted for $(P_4R_4)_5$ / poly-A (Figure 3.3c) and $(GR)_{20}$ / poly-A droplets (Figure 3.3d), where comparable spatial trends were observed (Figure 3.3e). In all cases, fluorescence recovery was consistently slower at the central region than at the inner boundary, indicating spatially heterogeneous diffusion dynamics of the dipeptide/RNA complexes. This slower recovery correlates with the higher concentration of the complexes at the droplet center, as also revealed by Raman spectroscopy (Figure 3.2 and Figure 3.A2). In all liquid droplets labeled with TAMRA-rA_{15}, the fluorescent recovery of TAMRA-rA_{15} molecules was found not to fully recover, as shown by the recovery curves for all droplet types (Figure 3.3b-d). This partial recovery suggests that a fraction of dipeptide/RNA complexes diffuse slowly within the liquid droplets during the limited observation time and/or the intensity did not recover due to the photo-bleaching effect of the low amount of TAMRA-rA_{15}. Furthermore, the intermediate fluorescence recovery of TAMRA-rA_{15} at the center region is slightly higher than that at the near boundary within liquid droplets (Figure 3.3b-d). These results correspond with the local density gradients across the droplet regions.

The $\tau_{1/2}$ values for TAMRA-rA_{15} in $(P_4R_4)_5$ / poly-A droplets were estimated to be 42.9 ± 9.5 s at the center and 36.1 ± 5.6 s at the boundary (Figure 3.3c and 3.3e), similar to the values observed with the $(PR)_{20}$ dipeptide. This suggests that the diffusion behavior of the dipeptide/RNA complexes is not strongly affected by the charge distribution pattern of the dipeptide repeat proteins. In contrast, $\tau_{1/2}$ values in $(GR)_{20}$ / poly-A droplets were significantly longer; 56.9 ± 19.8 s at the center and 47.4 ± 11.6 s at the boundary (Figure 3.3d and 3.3e).

This increase is likely due to the higher density of $(GR)_{20}$ / poly-A droplets, as confirmed by Raman spectroscopy (Figure 3.A5a). Furthermore, the ratios of average recovery half-times between the center and boundary remained consistent across all droplet types (Figure 3.3f). These results indicate that the diffusion behavior of poly-A RNA in arginine-rich dipeptide / poly-A RNA droplets is primarily governed by the droplet density rather than the charge pattern of the dipeptides.

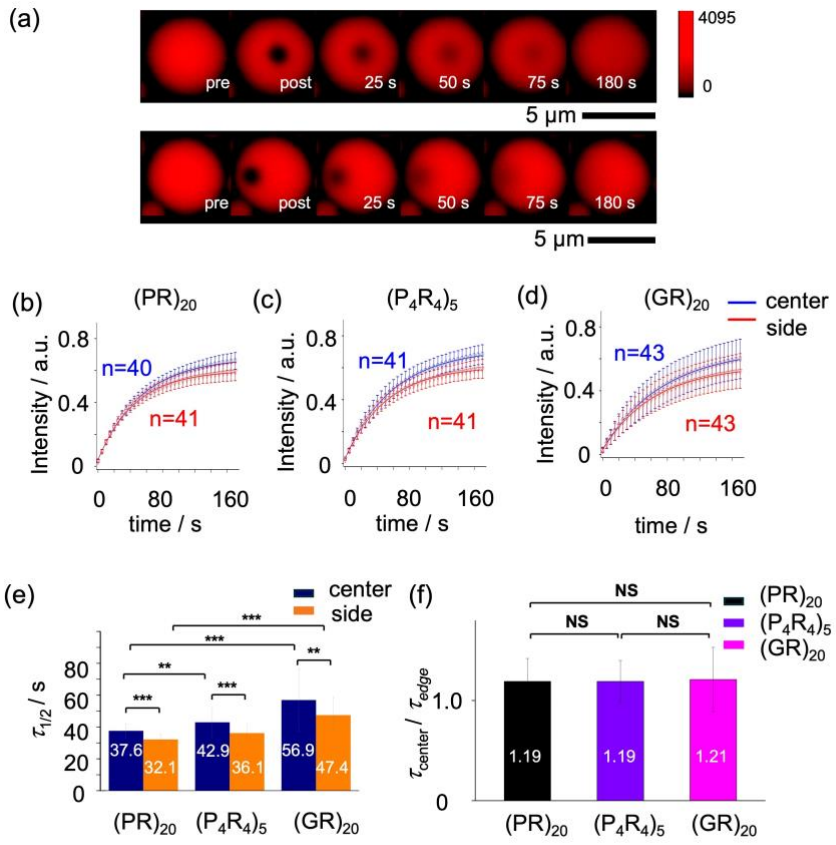

Figure 3.3. Diffusion of poly-A RNA in liquid droplets. (a) Fluorescence snapshots of $(PR)_{20}$ / poly-A RNA droplets before and after photobleaching. (b-d) Averaged FRAP curves at the center (blue line) and the inner boundary (red line) of droplets composed of $(PR)_{20}$ / poly-A RNA (b), $(P_4R_4)_5$ / poly-A RNA (c) and $(GR)_{20}$ / poly-A RNA droplets (d),

respectively. (e) Averaged half recovery time ($\tau_{1/2}$) at the center (blue bars) and inner boundary (orange bars) of each dipeptide. (f) Ratio of the recovery time at the center to that at the boundary for TAMRA-rA_{15} in $(PR)_{20}$ / poly-A RNA (black), $(P_4R_4)_5$ / poly-A RNA (purple) and $(GR)_{20}$ / poly-A RNA (pink) droplets. Asterisks indicate statistical significance based on t-test: *, $p < 0.05$, **, $p < 0.01$, ***, $p < 0.001$, NS: not significant ($p > 0.05$).

Diffusion Behavior of small molecules in Liquid Droplets: In the second set of FRAP measurements, we investigated the diffusion behavior of small molecules within droplets using three types of fluorescence dyes: TAMRA (Figure 3.4a), Rhodamine B (RhB) (Figure 3.4b), and fluorescein (Figure. 3.4c). These dyes were selected to mimic diffusion behavior of small biomolecules or drug-like compounds. In PBS (pH 7.4), TAMRA has a neutral net charge, RhB carries a positive charge, and fluorescein is negatively charged.[51, 52] Prior to droplet formation, the dyes were dissolved in PBS and mixed with a precursor solution containing non-labeled poly-A and the dipeptides, yielding a final dye concentration of 5 μM. Figure 3.4d-f show representative FRAP snapshots of the dyes at the center and boundary of a $(PR)_{20}$ / poly-A droplet. Notably, the fluorescence intensity of the negatively charged dye (fluorescein) recovered almost completely within 11 s after photobleaching (Figure 3.4f), whereas the bleached regions for TAMRA and RhB remained visible (Figure 3.4d and 3.4e). This observation indicates that the negatively charged dyes diffuse more rapidly than neutral or positively charged ones. In all cases, all small dye molecules showed almost fully fluorescent recovery (Figure 3.4g-i, Figure 3.A6d-f and Figure 3.A7d-f). This suggests that small dye molecules diffuse quickly within the liquid droplets in very short observation time. When comparing the recovery curves of the dipeptide/RNA complexes and small dye molecules in $(PR)_{20}$ droplets (Figure 3.3b and Figure 3.4g-i), the large molecular size of dipeptide/RNA complexes showed slow recovery while the small dye molecules did quick recovery in liquid phase. This suggests that the large molecular size of dipeptide/RNA complexes lead to molecular crowding due to the volume exclusion effect.

The corresponding fluorescence recovery curves for the three dyes are shown in Figure 3.4g-i, respectively. Blue lines represent the FRAP curves at the droplet center, and red lines correspond to the inner boundary of $(PR)_{20}$ / poly-A droplet. (See the Figure 3.A6 and A7 for the corresponding snapshots and recovery curves in $(GR)_{20}$ and $(P_4R_4)_5$ droplets, respectively.) The averaged $\tau_{1/2}$ values for each dye in droplets containing $(PR)_{20}$, $(P_4R_4)_5$ or $(GR)_{20}$ are summarized in Figure 3.5a-c. Consistent with the results obtained using fluorescently labeled poly-A RNA (Figure 3.3), fluorescence recovery was generally faster at the droplet boundary than at the center, regardless of charges of dye or dipeptide sequence. This suggests that diffusion of small molecules is generally enhanced near the droplet boundary. For $(PR)_{20}$-containing droplets, the averaged $\tau_{1/2}$ of TAMRA at the center was estimated to be 2.5 s. For fluorescein, $\tau_{1/2}$ was slightly shorter at 1.5 s, while RhB exhibited a significantly longer $\tau_{1/2}$ of 5.6 s (Figure 3.5a). This charge-dependent trend in recovery time was consistent across both droplet regions and different dipeptide sequences. Notably, the recovery times in $(GR)_{20}$ droplets were approximately twice as long as those in $(PR)_{20}$-containing droplets (Figure 3.5a and 3.5c), likely due to the higher density of $(GR)_{20}$-containing droplets, as discussed in Figure 3.3.

Finally, the ratio of recovery time between the droplet center and boundary for TAMRA and RhB showed no significant difference across between $(PR)_{20}$, $(P_4R_4)_5$ and $(GR)_{20}$-containing droplets. However, for fluorescein, this ratio varies significantly between the different dipeptide droplets (Figure 3.5d), suggesting a stronger binding between negatively charged molecules and $(GR)_{20}$ compared to $(PR)_{20}$. Previous studies using zeta potential measurements and simulations have shown that such droplets are generally negatively charged.[12, 14, 53] This could explain the observed charge-dependent diffusion behavior of the fluorescence dyes. These differences in diffusion behavior are likely due to electrostatic interactions within the droplets, where negatively charged fluorescein is repelled and thus diffuses more rapidly, while positively charged RhB experiences attractive interactions and therefore diffuses more slowly.

Thus, by tuning the charge of drug molecules to align with the electrostatic environment of the droplets during drug design, it may be possible to retain their enrichment within the droplets while reducing diffusion hinderance. In combination with droplet-disrupting argents, such as 1,6-hexanediol (1,6-HD), this strategy could enhance drug bioavailability and open up novel therapeutic avenues.

Collectively, our Raman and FRAP measurements reveal heterogenetic dynamics and hierarchical structure within liquid droplets, consistent with an internal concentration gradient of RNA. The complex diffusion behavior observed is primarily driven by the formation of stable RNA-dipeptide complexes. Importantly, both the overall charge and density variations within droplets, arising from interactions with arginine-rich dipeptides, should be taken into account when analyzing diffusion processes in these systems.

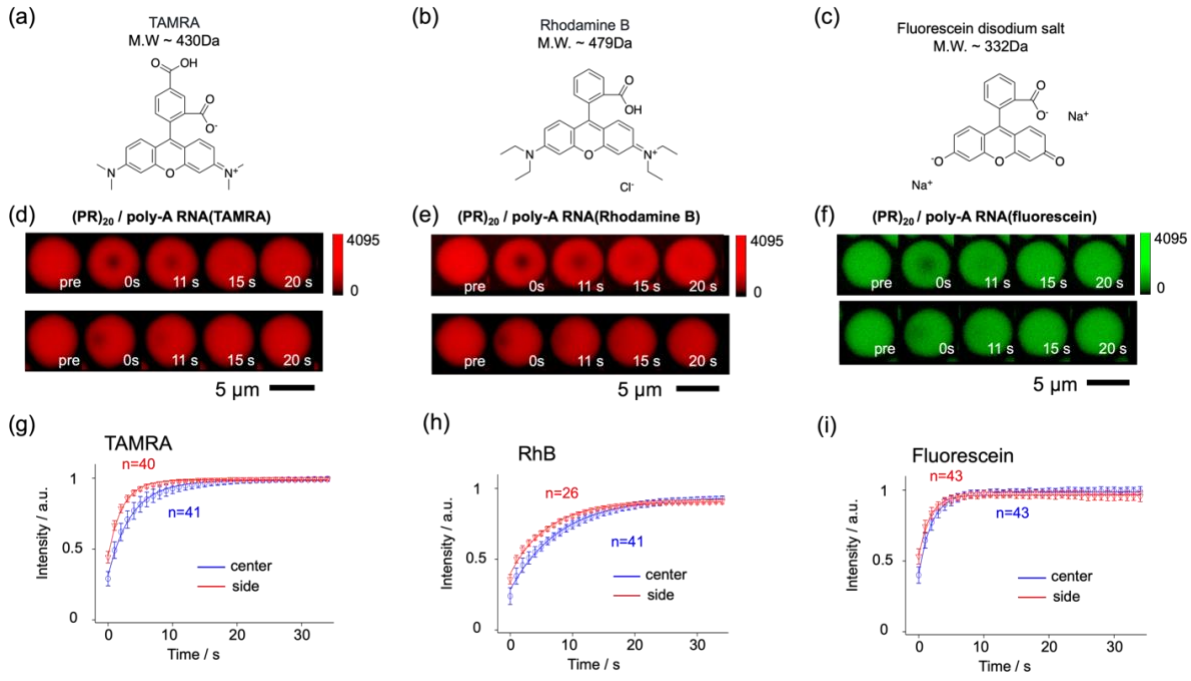

Figure 3.4. **Diffusion of small molecules in liquid droplets**. Chemical structures of TAMRA (a), Rhodamine B (b), and fluorescein (c), respectively. Fluorescence snapshot after

photobleaching in the center region and inner boundary of $(PR)_{20}$/poly-A RNA droplets containing TAMRA (d), Rhodamine B (e), or fluorescein (f). Averaged FRAP curves at the center (blue) and inner boundary (red) of $(PR)_{20}$/poly-A RNA droplets containing TAMRA (g), Rhodamine B (h), or fluorescein (i), respectively.

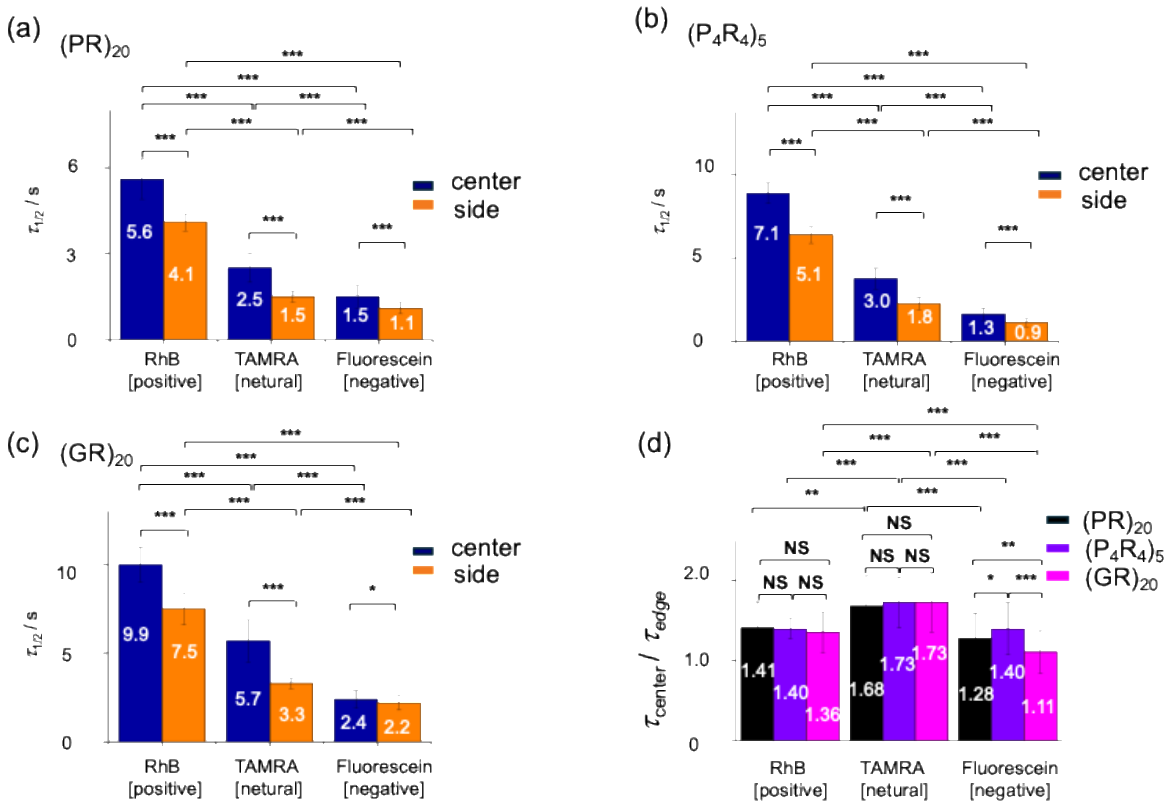

Figure 3.5. **Averaged recovery time of small molecules in liquid droplets**. (a-c) Averaged half recovery time at the center (blue) and inner boundary (orange) of droplets containing $(PR)_{20}$ (a), $(P_4R_4)_5$ (b) and $(GR)_{20}$ (c). (d) Ratio of the averaged recovery half-time between the center and boundary in $(PR)_{20}$ / poly-A RNA (black), $(P_4R_4)_5$ / poly-A RNA (purple) and $(GR)_{20}$ / poly-A RNA (pink) droplets. Asterisks indicate statistical significance based on t-test: *, $p < 0.05$, **, $p < 0.01$, ***, $p < 0.001$, NS: not significant ($p > 0.05$).

3.5 Conclusions

In this study, we investigated the molecular organization and diffusion behavior within arginine-rich dipeptide/poly-A RNA condensates using Raman spectroscopy and fluorescence recovery after photobleaching (FRAP). Raman spectroscopic analysis revealed that the dipeptides $(PR)_{20}$ and $(GR)_{20}$, when mixed with poly-A RNA, form spherical liquid droplets enriched in RNA–dipeptide complexes. Raman intensity mapping demonstrated a concentration gradient of poly-A RNA, with higher density at the droplet center. This suggests the formation of a hierarchical internal structure within droplets, likely governed by intermolecular interactions such as hydrogen bonding, cation–π interactions, and electrostatic forces. FRAP measurements further revealed spatially heterogeneous diffusion dynamics inside the droplets. Labeled poly-A RNA exhibited slower fluorescence recovery at the center compared to the periphery, in agreement with the Raman-based density distribution. Interestingly, the diffusion behavior was more strongly influenced by droplet density than by the specific charge pattern of the arginine-rich dipeptides. Droplets formed with $(GR)_{20}$ showed significantly slower recovery times than those with $(PR)_{20}$, consistent with their higher molecular density. Additionally, the diffusion of small fluorescent dyes varied with their net charge. Negatively charged fluorescein diffused more rapidly than positively or neutrally charged dyes, highlighting the charge-dependent permeability of the droplet environment. This permeability varied across dipeptide sequences and droplet regions, suggesting selective molecular partitioning based on physicochemical properties. Together, our results reveal that arginine-rich dipeptide/poly-A RNA droplets are not uniform liquid phases but possess complex internal structure and diffusion behavior shaped by molecular density, charge interactions, and component composition. These findings underscore the importance of considering internal density heterogeneity and charge-driven interactions when studying biomolecular condensates, with implications for understanding the regulation of biochemical

processes in membrane-less organelles, designing synthetic condensates for biomedical applications, and potential therapeutic strategies for treating neuronal diseases.

3.6 Appendix

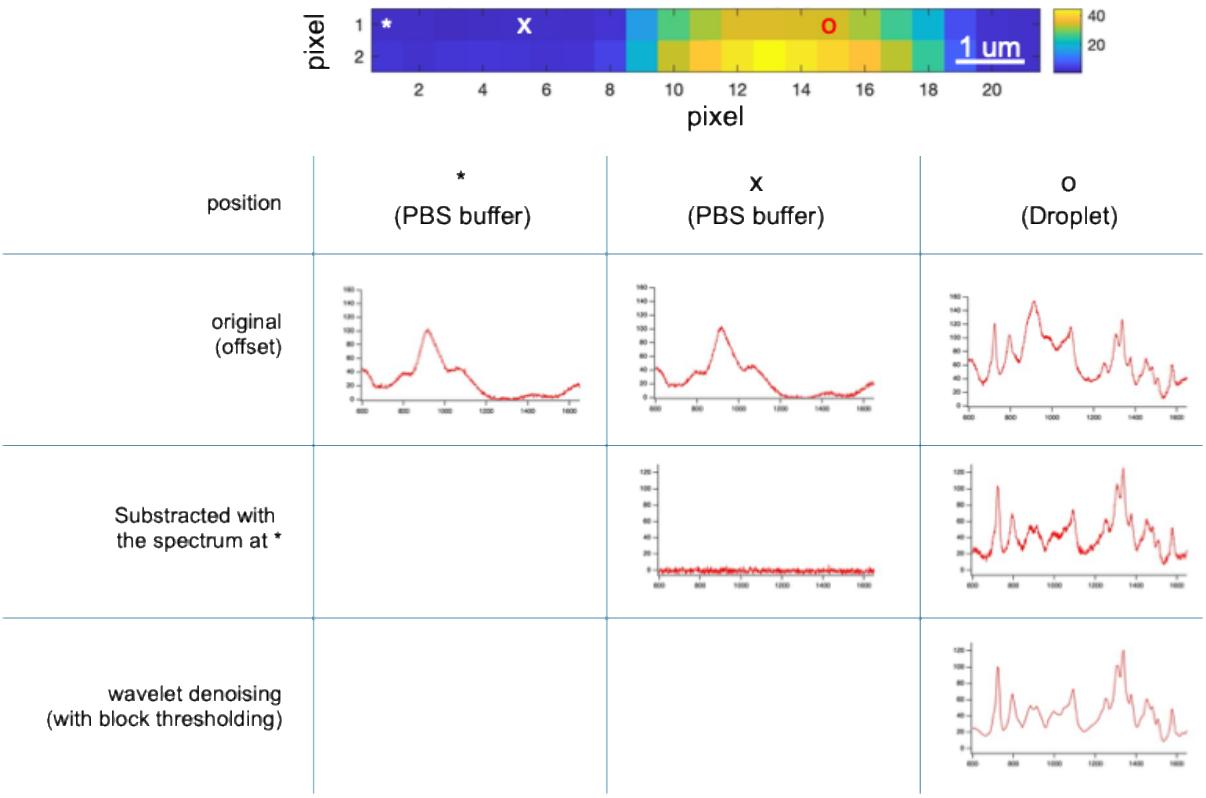

Figure 3.A1. Normalization of Raman spectra in the droplets. Raman scattering intensity map of the liquid droplet sweeping in the x-direction. Normalization of Raman spectra in the mapping data using a spectrum in PBS buffer in each map (outside the droplets).

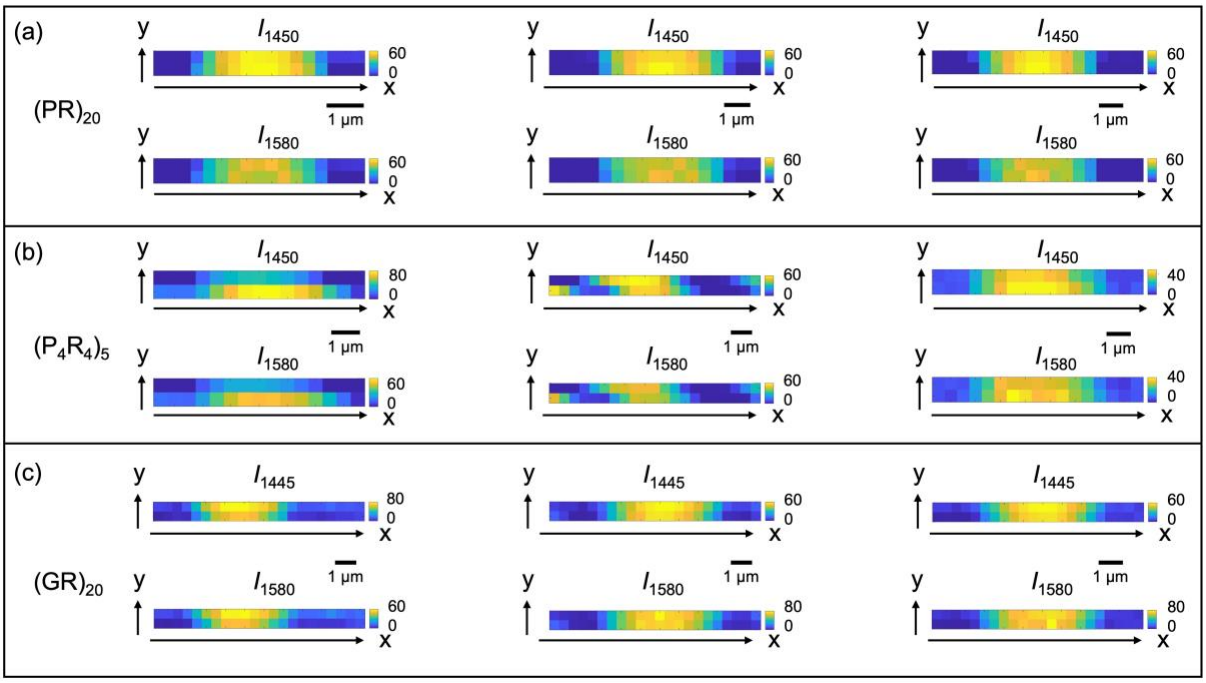

Figure 3.A2. Raman scattering intensity maps of the liquid droplets sweeping in the x-direction. The Raman scattering signal at 1450 cm^{-1} indicating CH_2 /CH_3 deformation modes from the side chain of arginine-rich dipeptide and at 1580 cm^{-1} indicating u(C=C) stretching mode of poly-A RNA generated the intensity maps within droplets composed of $(PR)_{20}$ / poly-A RNA (a), $(P_4R_4)_5$ / poly-A RNA (b) and $(GR)_{20}$ / poly-A RNA droplets (c), respectively.

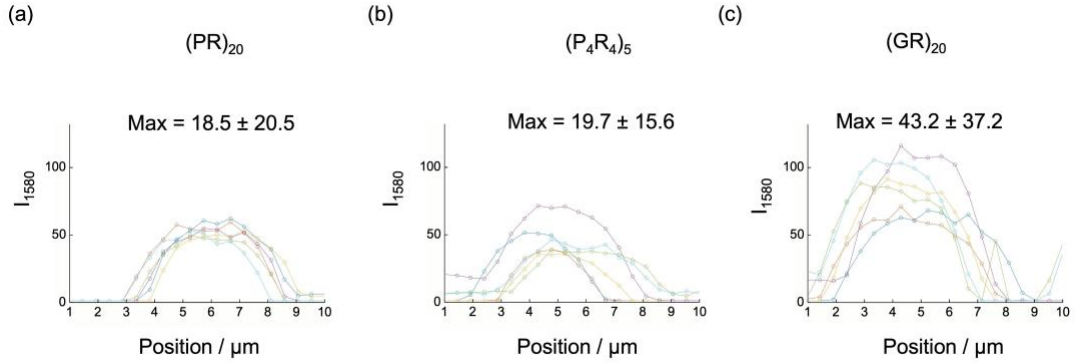

Figure 3.A3. Peak intensity at 1580 cm^{-1} in the droplets. Normalization of Raman spectra in each mapping data using a spectrum in PBS buffer in each map (outside of the droplets) to compare the peak intensity at 1580 cm^{-1} indicating u(C=C) stretching mode of poly-A RNA among $(PR)_{20}$ / poly-A PR20 (a), $(P_4R_4)_5$ / poly-A (b), and $(GR)_{20}$ / poly-A droplets (c), respectively.

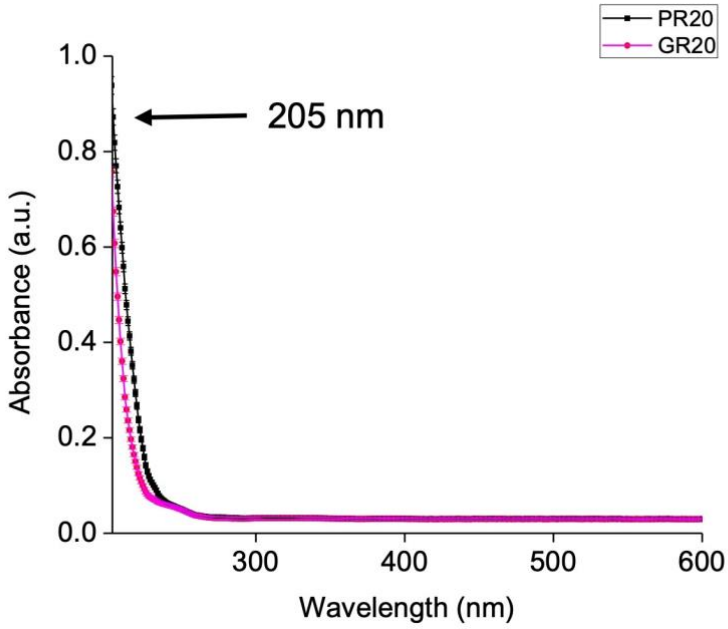

Figure 3.A4. The UV absorbance spectra of dipeptide solutions. Absorption spectra (205-600 nm) of $(PR)_{20}$ (black line) and $(GR)_{20}$ (pink line) in PBS buffer, with n=3. The absorption intensity at 205 nm is due to absorbance from peptide bonds on the peptide backbone and absorbance from side chain of arginine. The error bars show ± SD.

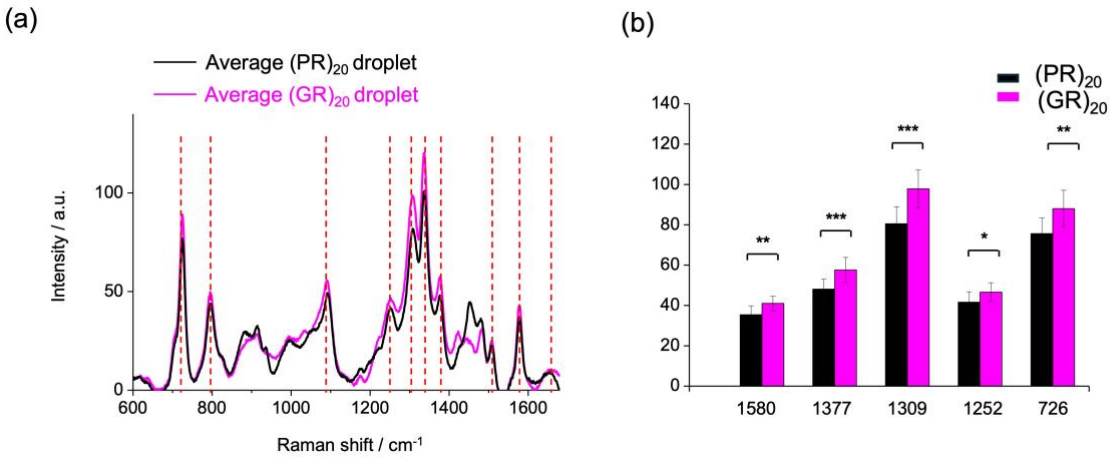

Figure 3.A5. The Raman intensity of liquid droplets. (a) Average Raman spectra of $(PR)_{20}$ / poly-A (black line) and $(GR)_{20}$ / poly-A (pink line), in multiple droplets (n=10). All spectra were acquired in 300s at the center region for each droplet. Red dash lines represent the peaks appeared in both $(PR)_{20}$ / poly-A and $(GR)_{20}$ / poly-A droplets. (b) Raman intensities in $(PR)_{20}$ / poly-A (black) and in (GR)20 / poly-A droplets (pink). Vibrational modes appeared in both $(PR)_{20}$ / poly-A and $(GR)_{20}$ / poly-A droplets. The intensity in $(GR)_{20}$ / poly-A RNA at 1580 cm^{-1}, 1377 cm^{-1}, 1309 cm^{-1}, and 726 cm^{-1} is 1.2 times higher than that of $(PR)_{20}$ / poly-A RNA droplet. The intensity in (GR)20 / poly-A RNA at 1252 cm^{-1} is 1.1 times higher than that of the (PR)20 / poly-A RNA droplet. The background by the spectrum outside the droplets was subtracted from the Raman intensity of each mode in the droplets. The asterisks indicate the significance of the t-test: ***, $p < 0.001$, **, $p < 0.01$, *, $p < 0.05$.

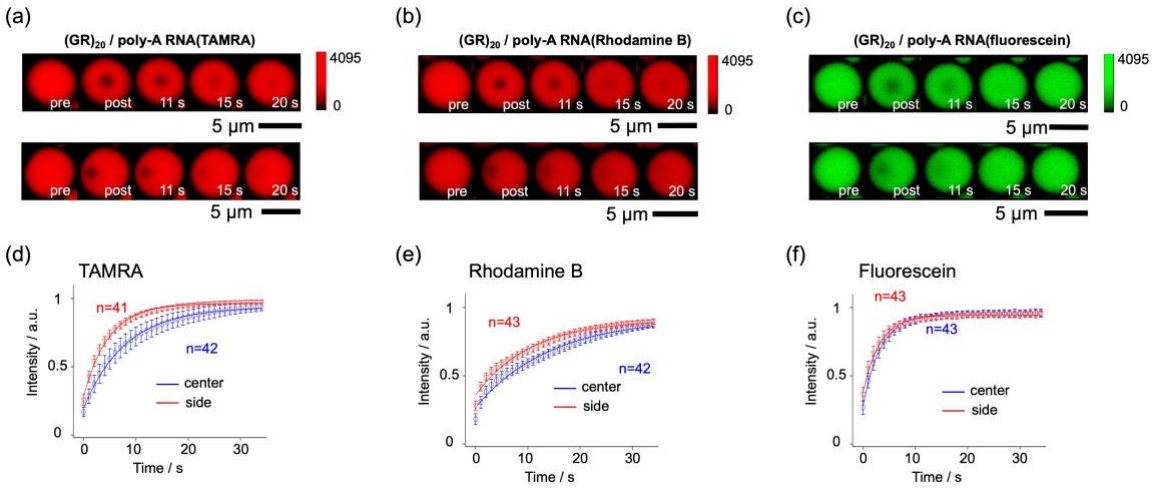

Figure 3.A6. **Diffusion of small molecules in $(GR)_{20}$ / poly-A droplets**. Snapshot of fluorescence images after photobleaching of TAMRA (a), Rhodamine B (b), or fluorescein (c) in the center region (top) and inner boundary (bottom) of $(GR)_{20}$/poly-A droplets, respectively. The averaged FRAP curves at the central region (blue) and the inner boundary (red) in the droplet of $(GR)_{20}$/poly-A with TAMRA (d), Rhodamine B (e), or fluorescein (f), respectively.

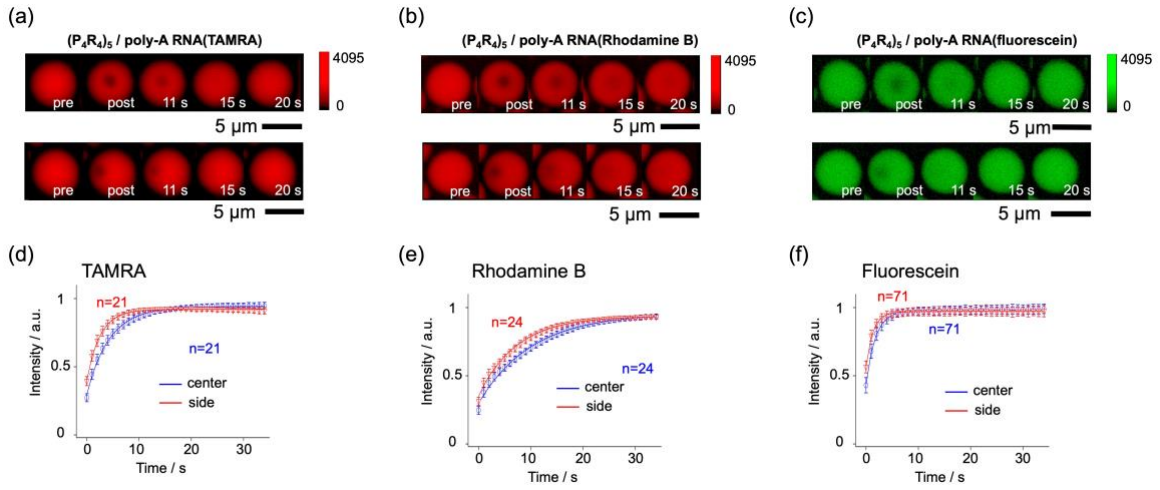

Figure 3.A7. **Diffusion of small molecules in $(P_4R_4)_5$ / poly-A droplets**. Snapshot of fluorescence images after photobleaching of TAMRA (a), Rhodamine B (b), or fluorescein (c) in the center region (top) and inner boundary (bottom) of $(P_4R_4)_5$ /poly-A droplets, respectively. The averaged FRAP curves at the central region (blue) and the inner boundary (red) in the droplet of $(P_4R_4)_5$/poly-A with TAMRA (d), Rhodamine B (e), or fluorescein (f), respectively.

3.7 Reference

1 Brangwynne, C. P.; Eckmann, C. R.; Courson, D. S.; Rybarska, A.; Hoege, C.; Gharakhani, J.; Julicher, F.; Hyman, A. A. Germline P granules are liquid droplets that localize by controlled dissolution/condensation. *Science* **2009,** *324* (5935), 1729-1732.

2 Nesterov, S. V.; Ilyinsky, N. S.; Uversky, V. N. Liquid-liquid phase separation as a common organizing principle of intracellular space and biomembranes providing dynamic adaptive responses. *Biochim Biophys Acta Mol Cell Res* **2021,** *1868* (11), 119102.

3 Mitrea, D. M.; Mittasch, M.; Gomes, B. F.; Klein, I. A.; Murcko, M. A. Modulating biomolecular condensates: a novel approach to drug discovery. *Nat Rev Drug Discov* **2022,** *21* (11), 841-862.

4 Li, W.; Jiang, C.; Zhang, E. Advances in the phase separation-organized membraneless organelles in cells: a narrative review. *Transl Cancer Res* **2021,** *10* (11), 4929-4946.

5 Yang, S.; Shen, W.; Hu, J.; Cai, S.; Zhang, C.; Jin, S.; Guan, X.; Wu, J.; Wu, Y.; Cui, J. Molecular mechanisms and cellular functions of liquid-liquid phase separation during antiviral immune responses. *Front Immunol* **2023,** *14*, 1162211.

6 Kanekura, K.; Yagi, T.; Cammack, A. J.; Mahadevan, J.; Kuroda, M.; Harms, M. B.; Miller, T. M.; Urano, F. Poly-dipeptides encoded by the C9ORF72 repeats block global protein translation. *Hum Mol Genet* **2016,** *25* (9), 1803-1813.

7 Ryan, V. H.; Fawzi, N. L. Physiological, Pathological, and Targetable Membraneless Organelles in Neurons. *Trends Neurosci* **2019,** *42* (10), 693-708.

8 Du, M.; Stitzinger, S. H.; Spille, J. H.; Cho, W. K.; Lee, C.; Hijaz, M.; Quintana, A.; Cisse, II. Direct observation of a condensate effect on super-enhancer controlled gene bursting. *Cell* **2024,** *187* (2), 331-344 e317.

9 Kanekura, K.; Kuroda, M. How can we interpret the relationship between liquid-liquid phase separation and amyotrophic lateral sclerosis? *Lab Invest* **2022,** *102* (9), 912-918.

10 Chen, C.; Yamanaka, Y.; Ueda, K.; Li, P.; Miyagi, T.; Harada, Y.; Tezuka, S.; Narumi, S.; Sugimoto, M.; Kuroda, M.; Hayamizu, Y.; Kanekura, K. Phase separation and toxicity of C9orf72 poly(PR) depends on alternate distribution of arginine. *J Cell Biol* **2021,** *220* (11).

11 Rai, S.; Pramanik, S.; Mukherjee, S. Deciphering the liquid-liquid phase separation induced modulation in the structure, dynamics, and enzymatic activity of an ordered protein beta-lactoglobulin. *Chem Sci* **2024,** *15* (11), 3936-3948.

12 Chen, C.; Jia, H.; Nakamura, Y.; Kanekura, K.; Hayamizu, Y. Effect of Multivalency on Phase-Separated Droplets Consisting of Poly(PR) Dipeptide Repeats and RNA at the Solid/Liquid Interface. *ACS Omega* **2022,** *7* (23), 19280-19287.

13 Dai, Y.; Zhou, Z.; Yu, W.; Ma, Y.; Kim, K.; Rivera, N.; Mohammed, J.; Lantelme, E.; Hsu-Kim, H.; Chilkoti, A.; You, L. Biomolecular condensates regulate cellular electrochemical equilibria. *Cell* **2024,** *187* (21), 5951-5966 e5918.

14 Welsh, T. J.; Krainer, G.; Espinosa, J. R.; Joseph, J. A.; Sridhar, A.; Jahnel, M.; Arter, W. E.; Saar, K. L.; Alberti, S.; Collepardo-Guevara, R.; Knowles, T. P. J. Surface Electrostatics Govern the Emulsion Stability of Biomolecular Condensates. *Nano Lett* **2022,** *22* (2), 612-621.

15 Renton, A. E.; Majounie, E.; Waite, A.; Simon-Sanchez, J.; Rollinson, S.; Gibbs, J. R.; Schymick, J. C.; Laaksovirta, H.; van Swieten, J. C.; Myllykangas, L.; Kalimo, H.; Paetau, A.; Abramzon, Y.; Remes, A. M.; Kaganovich, A.; Scholz, S. W.; Duckworth, J.; Ding, J.; Harmer, D. W.; Hernandez, D. G.; Johnson, J. O.; Mok, K.; Ryten, M.; Trabzuni, D.; Guerreiro, R. J.; Orrell, R. W.; Neal, J.; Murray, A.; Pearson, J.; Jansen, I. E.; Sondervan, D.; Seelaar, H.; Blake, D.; Young, K.; Halliwell, N.; Callister, J. B.; Toulson, G.; Richardson, A.; Gerhard, A.; Snowden, J.; Mann, D.; Neary, D.; Nalls, M. A.; Peuralinna, T.; Jansson, L.; Isoviita, V. M.; Kaivorinne, A. L.; Holtta-Vuori, M.; Ikonen, E.; Sulkava, R.; Benatar, M.; Wuu, J.; Chio, A.; Restagno, G.; Borghero, G.; Sabatelli, M.; Consortium, I.; Heckerman, D.; Rogaeva, E.; Zinman, L.; Rothstein, J. D.; Sendtner, M.; Drepper, C.; Eichler, E. E.; Alkan, C.; Abdullaev, Z.; Pack, S. D.; Dutra, A.; Pak, E.; Hardy, J.; Singleton, A.; Williams, N. M.; Heutink, P.; Pickering-Brown, S.; Morris, H. R.; Tienari, P. J.; Traynor, B. J. A hexanucleotide repeat expansion in C9ORF72 is the cause of chromosome 9p21-linked ALS-FTD. *Neuron* **2011,** *72* (2), 257-268.

16 Tran, H.; Almeida, S.; Moore, J.; Gendron, T. F.; Chalasani, U.; Lu, Y.; Du, X.; Nickerson, J. A.; Petrucelli, L.; Weng, Z.; Gao, F. B. Differential Toxicity of Nuclear RNA Foci versus Dipeptide Repeat Proteins in a Drosophila Model of C9ORF72 FTD/ALS. *Neuron* **2015,** *87* (6), 1207-1214.

17 Yamakawa, M.; Ito, D.; Honda, T.; Kubo, K.; Noda, M.; Nakajima, K.; Suzuki, N. Characterization of the dipeptide repeat protein in the molecular pathogenesis of c9FTD/ALS. *Hum Mol Genet* **2015,** *24* (6), 1630-1645.

18 Kwon, I.; Xiang, S.; Kato, M.; Wu, L.; Theodoropoulos, P.; Wang, T.; Kim, J.; Yun, J.; Xie, Y.; McKnight, S. L. Poly-dipeptides encoded by the C9orf72 repeats bind nucleoli, impede RNA biogenesis, and kill cells. *Science* **2014,** *345* (6201), 1139-1145.

19 Lee, K. H.; Zhang, P.; Kim, H. J.; Mitrea, D. M.; Sarkar, M.; Freibaum, B. D.; Cika, J.; Coughlin, M.; Messing, J.; Molliex, A.; Maxwell, B. A.; Kim, N. C.; Temirov, J.; Moore, J.; Kolaitis, R. M.; Shaw, T. I.; Bai, B.; Peng, J.; Kriwacki, R. W.; Taylor, J. P. C9orf72 Dipeptide Repeats Impair the Assembly, Dynamics, and Function of Membrane-Less Organelles. *Cell* **2016,** *167* (3), 774-788 e717.

20 Boeynaems, S.; Bogaert, E.; Kovacs, D.; Konijnenberg, A.; Timmerman, E.; Volkov, A.; Guharoy, M.; De Decker, M.; Jaspers, T.; Ryan, V. H.; Janke, A. M.; Baatsen, P.; Vercruysse, T.; Kolaitis, R. M.; Daelemans, D.; Taylor, J. P.; Kedersha, N.; Anderson, P.; Impens, F.; Sobott, F.; Schymkowitz, J.; Rousseau, F.; Fawzi, N. L.; Robberecht, W.; Van Damme, P.; Tompa, P.; Van Den Bosch, L. Phase Separation of C9orf72 Dipeptide Repeats Perturbs Stress Granule Dynamics. *Mol Cell* **2017,** *65* (6), 1044-1055 e1045.

21 Miyagi, T.; Ueda, K.; Sugimoto, M.; Yagi, T.; Ito, D.; Yamazaki, R.; Narumi, S.; Hayamizu, Y.; Uji, I. H.; Kuroda, M.; Kanekura, K. Differential toxicity and localization of arginine-rich C9ORF72 dipeptide repeat proteins depend on de-clustering of positive charges. *iScience* **2023,** *26* (6), 106957.

22 Boeynaems, S.; Holehouse, A. S.; Weinhardt, V.; Kovacs, D.; Van Lindt, J.; Larabell, C.; Van Den Bosch, L.; Das, R.; Tompa, P. S.; Pappu, R. V.; Gitler, A. D. Spontaneous driving forces give rise to protein-RNA condensates with coexisting phases and complex material properties. *Proc Natl Acad Sci U S A* **2019,** *116* (16), 7889-7898.

23 Murakami, K.; Kajimoto, S.; Shibata, D.; Kuroi, K.; Fujii, F.; Nakabayashi, T. Observation of liquid-liquid phase separation of ataxin-3 and quantitative evaluation of its concentration in a single droplet using Raman microscopy. *Chem Sci* **2021,** *12* (21), 7411-7418.

24 Samuel, A. Z.; Sugiyama, K.; Ando, M.; Takeyama, H. Direct imaging of intracellular RNA, DNA, and liquid-liquid phase separated membraneless organelles with Raman microspectroscopy. *Commun Biol* **2022,** *5* (1), 1383.

25 Baruch Leshem, A.; Sloan-Dennison, S.; Massarano, T.; Ben-David, S.; Graham, D.; Faulds, K.; Gottlieb, H. E.; Chill, J. H.; Lampel, A. Biomolecular condensates formed by designer minimalistic peptides. *Nat Commun* **2023,** *14* (1), 421.

26 Avni, A.; Joshi, A.; Walimbe, A.; Pattanashetty, S. G.; Mukhopadhyay, S. Single-droplet surface-enhanced Raman scattering decodes the molecular determinants of liquid-liquid phase separation. *Nat Commun* **2022,** *13* (1), 4378.

27 Chatterjee, S.; Kan, Y.; Brzezinski, M.; Koynov, K.; Regy, R. M.; Murthy, A. C.; Burke, K. A.; Michels, J. J.; Mittal, J.; Fawzi, N. L.; Parekh, S. H. Reversible Kinetic Trapping of FUS Biomolecular Condensates. *Adv Sci (Weinh)* **2022,** *9* (4), e2104247.

28 Shuster, S. O.; Lee, J. C. Watching liquid droplets of TDP-43(CTD) age by Raman spectroscopy. *J Biol Chem* **2022,** *298* (2), 101528.

29 Tian, Y.; Zhang, Q.; Hirai, K.; Wen, H.; Feng, G. L.; Li, J. T.; Taemaitree, F.; Inose, T.; Kanekura, K.; Uji-i, H. Spatially heterogeneous dynamics of droplets formed by arginine-rich dipeptides and poly-A RNA during liquid-liquid phase separation. *Molecular Crystals and Liquid Crystals* **2024,** *768* (11), 403-409.

30 Scopes, R. K. Measurement of protein by spectrophotometry at 205 nm. *Anal Biochem* **1974,** *59* (1), 277-282.

31 Anthis, N. J.; Clore, G. M. Sequence-specific determination of protein and peptide concentrations by absorbance at 205 nm. *Protein Sci* **2013,** *22* (6), 851-858.

32 Kimura, H.; Cook, P. R. Kinetics of core histones in living human cells: little exchange of H3 and H4 and some rapid exchange of H2B. *J Cell Biol* **2001,** *153* (7), 1341-1353.

33 Kitamura, A.; Kubota, H.; Pack, C. G.; Matsumoto, G.; Hirayama, S.; Takahashi, Y.; Kimura, H.; Kinjo, M.; Morimoto, R. I.; Nagata, K. Cytosolic chaperonin prevents polyglutamine toxicity with altering the aggregation state. *Nat Cell Biol* **2006,** *8* (10), 1163-1170.

34 Tsutsumi, M.; Muto, H.; Myoba, S.; Kimoto, M.; Kitamura, A.; Kamiya, M.; Kikukawa, T.; Takiya, S.; Demura, M.; Kawano, K.; Kinjo, M.; Aizawa, T. In vivo fluorescence correlation spectroscopy analyses of FMBP-1, a silkworm transcription factor. *FEBS Open Bio* **2016,** *6* (2), 106-125.

35 Wilson, A. L.; Outeiral, C.; Dowd, S. E.; Doig, A. J.; Popelier, P. L. A.; Waltho, J. P.; Almond, A. Deconvolution of conformational exchange from Raman spectra of aqueous RNA nucleosides. *Commun Chem* **2020,** *3* (1), 56.

36 Hirakawa, A. Y.; Okada, H.; Sasagawa, S.; Tsuboi, M. Infrared and Raman spectra of adenine and its 15N and 13C substitution products. *Spectrochimica Acta Part A: Molecular Spectroscopy* **1985,** *41* (1-2), 209-216.

37 Sharma, B.; Asher, S. A. UV resonance Raman finds peptide bond-Arg side chain electronic interactions. *J Phys Chem B* **2011,** *115* (18), 5659-5664.

38 Aliaga, A. E.; Garrido, C.; Leyton, P.; Diaz, G.; Gomez-Jeria, J. S.; Aguayo, T.; Clavijo, E.; Campos-Vallette, M. M.; Sanchez-Cortes, S. SERS and theoretical studies of arginine. *Spectrochim Acta A Mol Biomol Spectrosc* **2010,** *76* (5), 458-463.

39 Garrido, C.; Aguayo, T.; Clavijo, E.; Gómez-Jeria, J. S.; Campos-Vallette, M. M. The effect of the pH on the interaction of L-arginine with colloidal silver nanoparticles. A Raman and SERS study. *Journal of Raman Spectroscopy* **2013,** *44* (8), 1105-1110.

40 Singh, S.; Donfack, P.; Srivastava, S. K.; Singh, D. K.; Materny, A.; Asthana, B. P.; Mishra, P. C. Monitoring potential molecular interactions of adenine with other amino acids using Raman spectroscopy and DFT modeling. *Spectrochim Acta A Mol Biomol Spectrosc* **2015,** *149*, 647-655.

41 Lafarga, V.; Sirozh, O.; Diaz-Lopez, I.; Galarreta, A.; Hisaoka, M.; Zarzuela, E.; Boskovic, J.; Jovanovic, B.; Fernandez-Leiro, R.; Munoz, J.; Stoecklin, G.; Ventoso, I.; Fernandez-Capetillo, O. Widespread displacement of DNA- and RNA-binding factors underlies toxicity of arginine-rich cell-penetrating peptides. *EMBO J* **2021,** *40* (13), e103311.

42 Martin, E. W.; Holehouse, A. S.; Peran, I.; Farag, M.; Incicco, J. J.; Bremer, A.; Grace, C. R.; Soranno, A.; Pappu, R. V.; Mittag, T. Valence and patterning of aromatic residues determine the phase behavior of prion-like domains. *Science* **2020,** *367* (6478), 694-699.

43 Wang, J.; Choi, J. M.; Holehouse, A. S.; Lee, H. O.; Zhang, X.; Jahnel, M.; Maharana, S.; Lemaitre, R.; Pozniakovsky, A.; Drechsel, D.; Poser, I.; Pappu, R. V.; Alberti, S.; Hyman, A. A. A Molecular Grammar Governing the Driving Forces for Phase Separation of Prion-like RNA Binding Proteins. *Cell* **2018,** *174* (3), 688-699 e616.

44 Gupta, R.; Lan, M.; Mojsilovic-Petrovic, J.; Choi, W. H.; Safren, N.; Barmada, S.; Lee, M. J.; Kalb, R. The Proline/Arginine Dipeptide from Hexanucleotide Repeat Expanded C9ORF72 Inhibits the Proteasome. *eNeuro* **2017,** *4* (1).

45 Kikuchi, K.; Yamazaki, Y.; Kanekura, K.; Hayamizu, Y. Graphene Biosensor

Differentiating Sensitive Interactions between Ribonucleic Acid and Dipeptide Repeats in Liquid-Liquid Phase Separation. *ACS Appl Mater Interfaces* **2025,** *17* (8), 12765-12771.

46 Kanekura, K.; Hayamizu, Y.; Kuroda, M. Order controls disordered droplets: structure-function relationships in C9ORF72-derived poly(PR). *Am J Physiol Cell Physiol* **2022,** *322* (2), C197-C204.

47 Vernon, R. M.; Chong, P. A.; Tsang, B.; Kim, T. H.; Bah, A.; Farber, P.; Lin, H.; Forman-Kay, J. D. Pi-Pi contacts are an overlooked protein feature relevant to phase separation. *Elife* **2018,** *7*, e31486.

48 Paloni, M.; Bussi, G.; Barducci, A. Arginine multivalency stabilizes protein/RNA condensates. *Protein Sci* **2021,** *30* (7), 1418-1426.

49 Chong, P. A.; Vernon, R. M.; Forman-Kay, J. D. RGG/RG Motif Regions in RNA Binding and Phase Separation. *J Mol Biol* **2018,** *430* (23), 4650-4665.

50 Chowdhury, M. N.; Jin, H. The RGG motif proteins: Interactions, functions, and regulations. *Wiley Interdiscip Rev RNA* **2023,** *14* (1), e1748.

51 Fischer, R.; Waizenegger, T.; Kohler, K.; Brock, R. A quantitative validation of fluorophore-labelled cell-permeable peptide conjugates: fluorophore and cargo dependence of import. *Biochim Biophys Acta* **2002,** *1564* (2), 365-374.

52 Kornprobst, T.; Plank, J. Photodegradation of Rhodamine B in Presence of CaO and NiO-CaO Catalysts. *International Journal of Photoenergy* **2012,** *2012* (1), 398230.

53 Chen, C.; Li, P.; Luo, W.; Nakamura, Y.; Dimo, V. S.; Kanekura, K.; Hayamizu, Y. Diffusion of LLPS Droplets Consisting of Poly(PR) Dipeptide Repeats and RNA on Chemically Modified Glass Surface. *Langmuir* **2021,** *37* (18), 5635-5641.

Summary and perspective

In summary, firstly, with a combination of FRAP measurements and Raman spectroscopy, this study focused on the spatial diffusion dynamics within liquid droplets formed by arginine-rich dipeptides and poly-A RNA via LLPS. FRAP analysis unveiled that poly-A RNA molecules diffuse more rapidly at the edge of droplets compared to those at the central region. Furthermore, Raman spectroscopy of the intensity revealed the clear concentration gradient of RNA molecules across liquid droplets: a lower concentration at the edge and a higher concentration at the central region of the droplets. Notably, this concentration gradient of RNA obatained with Raman spectroscopy aligns with the diffusion behavior of labeled RNA molecules in liquid droplets observed with FRAP measurements. However, the complex interactions between dipeptides and RNA molecules may further influence the diffusion behaviors of liquid droplets. Although further investigation is needed, this study demonstrates that Raman spectroscopy combined with FRAP has the potential to contribute to understanding the complex diffusion dynamics within liquid droplets.

Secondly, we investigated the spatial distribution of components with different charge properties within liquid droplets formed by arginine-rich dipeptides and poly-A RNA through LLPS. Using a combination of Raman spectroscopy and FRAP, we explored the spatial dynamics and structural organization of these droplets. Raman microscopy further demonstrated a concentration gradient of both RNA and dipeptides, with lower concentrations near the boundary and higher concentrations toward the center. This concentration gradient aligns with the observed diffusion behavior. FRAP analysis revealed that poly-A RNA diffuses more rapidly at the inner boundary than at the center. These findings suggest that concentration gradients, hierarchical structures, and dynamic interactions are key features of the droplets formed via LLPS. The RNA-peptide complexes within the droplets may influence diffusion, indicating potential internal interactions that warrant further investigation. Although further

investigation is needed, the study demonstrates that Raman microscopy has promising potential to help us understand the complex dynamics and structural organization of liquid droplets.

In conclusion, we investigated the spatially heterogeneous diffusion behaviors within arginine-rich dipeptide/poly-A RNA biomolecular condensates using Raman spectroscopy and FRAP analysis. We provide a powerful method for revealing the biophysical properties of biomolecular condensates. These findings help us understand the importance of considering density heterogeneity and charge-driven molecular interactions when investigating biomolecular coacervations, with implications for designing synthetic condensates for biomedical applications, thus contributing to a better understanding of the regulation of biochemical processes within membrane-less organelles and potential therapeutic strategies for treating neuronal diseases.

Publications

Publications related to this dissertation:

[1] Y. Tian, Q. Zhang, K. Hirai, H. Wen, G.L. Feng, J.T. Li, F. Taemaitree, T. Inose, K. Kanekura, H. Uji-i, Spatially Heterogeneous Dynamics of droplets formed by arginine-rich dipeptides and poly-A RNA during liquid-liquid phase separation, Molecular Crystals and Liquid Crystals. 2024. DOI: 10.1080/15421406.2024.2353937

[2] Y. Tian, Q. Zhang, J.T. Li, M. Tsutsumi, T. Inose, F. Taemaitree, K. Hirai, K. Kanekura, H. Uji-i, Raman spectroscopy and FRAP analysis on density heterogeneity and diffusion behavior of complex coacervation by arginine-rich dipeptides and poly-A RNA, ACS Omega. 2025. DOI: 10.1021/acsomega.5c04844

Other publications:

[1] Q. Zhang; Inose, T.; Ricci, M.; Li, J.T.; Tian, Y.; Wen, H.; Toyouchi, S.; Fron, E.; Dao, A.T.N.; Kasai, H.; Rocha, S.; Hirai, K.; Fortuni, B.; Uji-I, H. Gold-Photodeposited Silver Nanowire Endoscopy for Cytosolic and Nuclear pH Sensing. Acs Appl Nano Mater, 4 (2021) 9886-9894.

[2] Q. Zhang; Murasugi, T.; Watanabe, K.; Wen, H.; Tian, Y.; Ricci, M.; Rocha, S.; Inose, T.; Kasai, H.; Taemaitree, F.; Uji-i, H.; Hirai, K.; Fortuni, B. Selective Detection of Intracellular Drug Metabolism by Metal-Organic Framework-Coated Plasmonic Nanowire. Advanced Optical Materials, 11 (2023) 2300856.

Conferences

[1] 2023.8.30-9.2, KJF International Conference on Organic Materials for Electronics and Photonics 2023. (poster)

[2] 2023.10.11, The 9th Hokkaido University Cross-Departmental Symposium. (poster)

[3] 2023.12.7-12.8, The 2023 RIES–CEFMS (Research Institute for Electronic Science – Center for Emergent Functional Matter Science) Joint International Symposium. (poster)

[4] 2025.9.1-9.5, Nanoscale, Single-Molecule and Related Spectroscopies (NSM). (poster)